Faculty of Physics and Astronomy

University of Heidelberg

Diploma thesis
in Physics
submitted by
Markward Britsch
born in Lahr
2003

Hyperon Production in Proton–Nucleus Collisions at 42 GeV Center of Mass Energy

This diploma thesis has been carried out by Markward Britsch at the
Max-Planck-Institute for Nuclear Physics, Heidelberg
under the supervision of
Prof. Dr. Werner Hofmann

Abstract

The subject of this thesis is a measurement of hyperon production ratios which is of special interest as a reference on Quark Gluon Plasma search. The data used in this analysis have been taken with a minimum bias trigger at the fixed target experiment HERA-B, which uses the 920 GeV proton beam of the HERA storage ring at DESY. Λ, Ξ and Ω hyperons produced in collisions using carbon and tungsten wires as targets were reconstructed. Hyperon ratios are presented for the rapidity range $-1.5 < y < 0.5$ (where they were measured), extrapolated to the whole phase space and to $y = 0$. The main results at $y = 0$ are $\frac{\overline{\Lambda}}{\Lambda} = 0.88 \pm 0.07$ (error including systematic error) and $\frac{\overline{\Xi}}{\Xi} = 0.69 \pm 0.12$ (statistical uncertainty only) for the carbon target. These values are compared to proton–nucleus and nucleus–nucleus data above and below HERA-B energies and are comparable with both. In the rapidity range $-1.5 < y < 0.5$ the ratio $\frac{\overline{\Lambda}}{\Lambda}$ is significantly different for the two target materials, whereas extrapolated to the whole phase space it is not. A possible explanation in terms of multiple scatterings in the nucleus is given. The distribution of the Λ particle–anti-particle asymmetry versus Feynman's scaling variable x_f using the carbon target is found to be in good agreement with measurements from pion–nucleus reactions at 500 GeV π-beam energy.

Zusammenfassung

Das Thema dieser Arbeit ist eine Messung von Hyperon-Anzahlverhältnissen, welche als Referenzdaten für die Suche nach Quark Gluon Plasma benötigt werden. Die Daten, die für diese Arbeit verwendet wurden, sind mit einem Minimum Bias Trigger beim Fixed Target Experiment HERA-B aufgenommen worden, das den 920 GeV Protonenstrahl des Speicherrings HERA am DESY verwendet. Λ-, Ξ- und Ω-Hyperonen, die in Reaktionen mit Kohlenstoff- und Wolframtargetdrähten entstanden, wurden rekonstruiert. Hyperonverhältnisse werden im Rapiditätsbereich $-1.5 < y < 0.5$ (in dem sie gemessen wurden), in den gesamten Phasenraum und nach $y = 0$ extrapoliert präsentiert. Die Hauptergebnisse bei $y = 0$ für das Kohlenstofftarget sind $\frac{\overline{\Lambda}}{\Lambda} = 0.88 \pm 0.07$ (statistischer und systematischer Fehler) und $\frac{\overline{\Xi}}{\Xi} = 0.69 \pm 0.12$ (nur statistischer Fehler). Diese Werte werden mit Proton–Kern und Kern–Kern Daten verglichen, deren Energien ober- und unterhalb der HERA-B Energie liegen, und sind mit diesen verträglich. Im Rapiditätsbereich $-1.5 < y < 0.5$ ist $\frac{\overline{\Lambda}}{\Lambda}$ für die beiden Targetmaterialien signifikant verschieden, extrapoliert auf den gesamten Phasenraum jedoch nicht. Eine mögliche Erklärung durch Vielfachstreuung im Kern wird gegeben. Die Verteilung der Teilchen–Antiteilchen Asymmetrie in Feynmans Scaling Variable x_f für die Λ Hyperonen stimmt gut mit Messungen an Pion–Kern Reaktionen bei 500 GeV π-Strahl Energie überein.

Contents

List of Figures

List of Tables

Aus dem
"Lexikon der erklärungsbedürftigen Wunder,
Daseinsformen und Phänomene Zamoniens und
Umgebung"
von Prof. Dr. Abdul Nachtigaller

Dimensionslochraum, der: Es ist eigentlich ganz einfach, sich einen Quadratmeter des Dimensionslochraumes vorzustellen, vorausgesetzt, man hat mindestens sieben Gehirne:

Stellen Sie sich einen Zug vor, der mit einer Kerze auf dem Dach durch ein schwarzes Loch fährt, während Sie selbst mit einer Kerze auf dem Kopf auf einem Glockenturm auf dem Mars stehen und eine Uhr aufziehen, die genau einen Quadratmeter groß ist, und ein Uhu, der übrigens auch eine Kerze auf dem Kopf trägt, in entgegengesetzter Richtung zum Zug und mit Lichtgeschwindigkeit durch einen Tunnel fliegt, welcher gerade von einem anderen schwarzen Loch verschluckt wird, das ebenfalls eine Kerze auf dem Kopf trägt (sofern Sie sich ein schwarzes Loch mit einer Kerze auf dem Kopf vorstellen können, dazu benötigen Sie mindestens vier Gehirne). Verbinden Sie die vier Punkte, an denen die Kerzen brennen, mit einem Buntstift, und Sie haben einen Quadratmeter des Dimensionslochraums. Auf der Uhr können Sie übrigens nachsehen, wie spät es auf dem Mars ist, sogar im Dunkeln, denn Sie haben ja eine Kerze auf dem Kopf.

By Walter Moers in "Die $13\frac{1}{2}$ Leben des Käpt'n Blaubär".

Chapter 1

Introduction

In this chapter, the theoretical background is described and experimental results from earlier experiments on strangeness production are presented. The context of the work presented in this thesis will be described in Section 1.4, where an overview of this thesis will also be given.

1.1 The Standard Model

The question of the origin of the universe is as old as mankind. Deeply interwoven with this is the question, whether there is any simple underlying order in the universe, a set of fundamental laws, or even just one. Modern physics and cosmology seem to be close to the answer to these questions.
The Standard Model of particle physics (see *e.g.* [Pov95]) tries to describe all particles and all possible particle interactions, and thus all physics in some sense, by as few components as possible. There are the three fundamental interactions in the Standard Model: the strong interaction, the weak interaction and the electromagnetic interaction. Gravitation could not yet be

fermions	family			charge	color	weak isospin		spin
	1	2	3			left handed	right handed	
leptons	ν_e	ν_μ	ν_τ	0	–	1/2	0	1/2
	e	μ	τ	-1			0	
quarks	u	c	t	$+2/3$	r, g, b	1/2	0	1/2
	d	s	b	$-1/3$			0	

Table 1.1: The fundamental particles

interaction	acts on	particles mediating	mass (GeV)	spin
gravitational	mass - energy	graviton (not yet observed)	0	2
strong	color charge	8 gluons (g)	0	1
electromagnetic	electric charge	photon (γ)	0	1
weak	weak isospin	W^+, W^-, Z	$\approx 10^2$	1

Table 1.2: The fundamental interactions

included in this model, but for particle processes it can be neglected altogether[1].
To our present knowledge there are three families – or generations – of fundamental particles grouped according to their hierarchy in mass and divided in two sectors. There is the leptonic sector (the light ones), consisting of the electron, the muon and the tau and their corresponding neutrinos. The electron and the electron neutrino are in the same family. The other sector contains the quarks, consisting of (**u**p, **d**own), (**c**harmed, **s**trange) and (**t**op, **b**ottom). Each pair forms one generation, as illustrated in Table 1.1. The fundamental particles in the Standard Model are all spin-$\frac{1}{2}$ fermions.
The particles that mediate the interactions are bosons (*i.e.* particles of integer spin, fermions are of half integer spin), also called gauge bosons. There is the photon, mediating the electromagnetic interaction, the Z and $W^{\pm}$, mediating the weak interaction and the eight gluons for the strong interaction. In a quantized theory of gravitation it is assumed that gravitation is mediated by gauge bosons called gravitons. For an overview of the properties of the gauge bosons, please refer to Table 1.2.
There is a hierarchy between the four fundamental interactions, sometimes also called "forces". At energies much lower than 80 GeV gravitation is by far the weakest, followed by the weak force, then the electromagnetic and finally the strong force. This also corresponds to typical lifetimes. Particles that decay due to weak interaction have the longest lifetimes ($\sim 10^{-10}$ s), followed by particles decaying electromagnetically ($\sim 10^{-16}$ s) and the strongly decaying particles ($\sim 10^{-23}$ s).
The most important connection between particle physics and cosmology is that particle physics can (try to) explain how particles behaved in the early

[1] Although, there are predictions by some string theories (beyond the Standard Model) that in the new LHC collider at CERN, there may be measurable gravitational effects like small black holes being produced in the collider [Dim01].

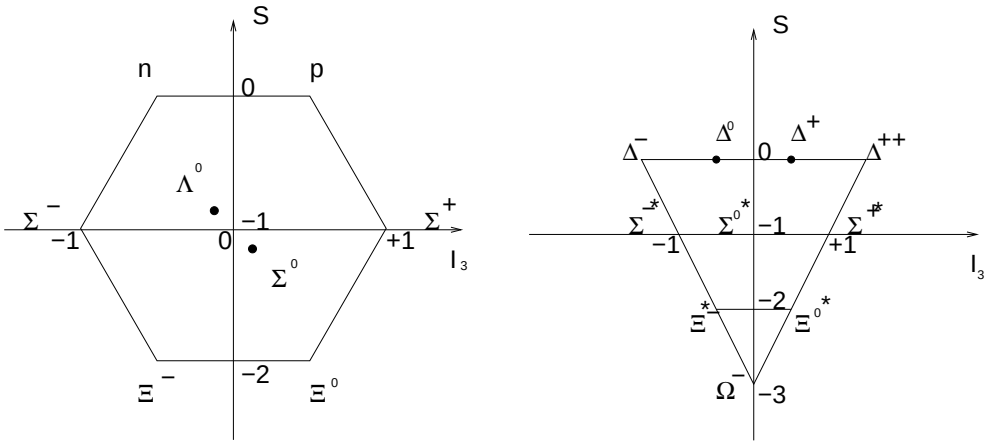

(a) The baryon octet, spin $\frac{1}{2}$ (b) The baryon decuplet, spin $\frac{3}{2}$

Figure 1.1: The baryon multiplets: The vertical axis is the strangeness, the horizontal axis is the third component of the isospin.

stages of the universe and contribute largely to the question of how particles could come into existence at all.

Most quantities in this thesis will be given in natural units, *i.e.* in units where $\hbar = c = k_B = 1$, energy is measured in multiplies of eV. This implies *e.g.* that also momentum, mass and temperature are measured in GeV or MeV. In some cases for clarity reasons, *e.g.* in detector geometry descriptions, SI units will be used.

1.1.1 Hadrons

Around 1930, only electrons and protons were known. Then the anti-particle of the electron, called positron, the neutron, the pion and some other particles were discovered. In 1947 the first so called V^0 was seen [Fra87]. A V^0 is a neutral particle, hence not leaving a track in a cloud chamber or photographic emulsion, decaying into a pair of charged particles. These V^0 particles were a puzzle, since they were produced in strong interactions *e.g.* pions colliding with a proton target, but then decayed with a lifetime of about $\sim 10^{-10}$ s, which is much larger than the typical decay time of strongly decaying particles. This led to the introduction of the so called strange quantum number, which is conserved in strong and electromagnetic interactions. Nowadays V^0 particles are known as Λ, $\overline{\Lambda}$ and K^0_S. Baryons with strangeness are called *hyperons*, examples are Λ, Ξ^- or Ω^- and their anti-particles. Anti-particles are usually marked by a bar.
More and more particles were discovered. Soon, there was a large variety of

hadron	quark content
p	(uud)
n	(udd)
Λ	(uds)
Σ^0	(uds)
Σ^-	(dds)
Σ^+	(uus)
Ξ^-	(dss)
Ξ^0	(uss)
Ω^-	(sss)
K^0	($d\bar{s}$)
K^-	($s\bar{u}$)
π^0	$\frac{1}{\sqrt{2}}$($d\bar{d}$ - $u\bar{u}$)
π^-	($d\bar{u}$)
π^+	($u\bar{d}$)

Table 1.3: Valence quark contents of some hadrons.

particles, which didn't fit at all into the search for a simple model. Apart from the leptons, of which not all known today had been discovered by that time, there were many particles called hadrons, which were divided into baryons, like the nucleons or the Λ, and mesons, like the pion or the kaon. To reduce the number of fundamental particles in the theory, Gell-Mann and Zweig independently proposed 1964 the so called quark[2] model [Fra87]. They proposed three kinds of quarks which were later called up, down and strange[3] as constituents of all known hadrons. Three of them would make up a baryon, a quark and an anti-quark would form a meson.
The hadrons had been arranged in multiplets before according to their quantum number of strangeness in isospin (see Fig. 1.1 for the most common baryon multiplets), and now these multiplets could be explained by the quark model.
Symmetry and symmetry breaking is a very important concept in physics. Assuming equal masses of the three quarks they could be described by three orthogonal states with SU(3) symmetry transformations between them. That way group theory could explain the multiplets in the context of the quark model. The proton for example is made up of (uud), the π^- of ($d\bar{u}$). More examples are given in Table 1.3.

[2]word in a poem by James Joyce
[3]the strange quark turned out to have a strangeness of -1, unfortunately.

quark	bare mass / MeV [Hag02]	constituent mass / MeV [Pov95]
down	5 – 8.5	≈ 300
up	1.5 – 4.5	≈ 300
strange	80 – 155	≈ 450
charm	1.0 – 1.4	
bottom	4.0 – 4.5	
top	174.3 ± 5.1	

Table 1.4: The quark masses. For heavy quarks, there is practically no difference between bare and constituent mass.

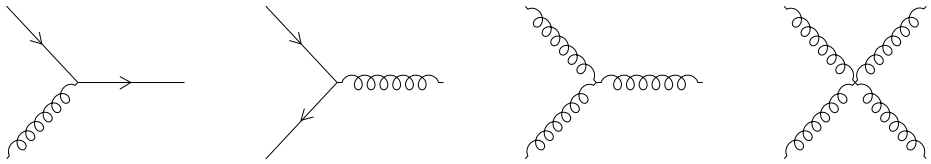

(a) (b) (c) (d)

Figure 1.2: The elementary QCD Feynman diagrams: a) gluon emission/absorption, b) quark pair creation/annihilation, c) 3-gluon vertex and d) 4-gluon vertex. These Feynman diagrams can be read for time axis going up, down, left or right, giving all possibilities.

All ground state hyperons shown in the baryon octet, except for the Σ^0 which decays mainly electromagnetically into $\Lambda\gamma$, can only decay weakly since they are the lightest particles containing one or more strange quarks and strangeness is, as stated before, conserved in the other interactions. They cannot turn into mesons due to baryon number conservation and they cannot turn into each other due to flavor conservation in strong and electromagnetic interactions. A special case is the Ω^- in the baryon decuplet. It is the lightest particle containing three strange quarks. In principle it could decay strongly into a K^- and a Ξ^0, but that is kinematically forbidden. So the Ω^- decays weakly mainly into Λ K^-.

1.1.2 QCD and Quark Gluon Plasma

Quantum **C**hromo**d**ynamics (QCD) is the **Q**uantum **F**ield **T**heory (QFT) of strong interactions. All particles are described by fields, and interactions are described by virtual gauge bosons being exchanged by the interacting particles. Virtual means that they cannot be detected directly and don't have

to satisfy $m^2 = E^2 - \vec{p}^2$. The "language" in which those interactions are described are the Feynman diagrams. Actually each element in a diagram corresponds to a mathematical term and a complete diagram represents a mathematical expression for a quantum amplitude. This amplitude is connected to the corresponding interaction cross section or lifetime by Fermi's Golden Rule. In Feynman diagrams, space is plotted versus time. Commonly, lines correspond to fermions, curly lines to photons, spring-like lines to gluons and dashed lines to the weak gauge bosons. Fermion lines have arrows that indicate the flow of the fermion number. Points where lines meet ("vertices") are interaction points. Internal lines, *i.e.* connecting two vertices, are called propagators, corresponding to virtual particles. In- and outgoing lines symbolize external particles.
The only particles that interact strongly are quarks and gluons. The QCD vertices are shown in Figure 1.2. It is important to note that gluons, unlike photons in the electromagnetic interaction, can interact directly with each other since they carry the "charge" to which they couple. This has some effects as will be described below.
The "charge" the gluons couple to is called color. There are three kinds of colors called red, blue and green. Anti-quarks carry anti-color, gluons carry a color *and* an anti-color. Color cannot be observed directly in the experiment, only "white" objects can be seen. As a consequence, a meson must have *e.g.* a red colored quark and an anti-red colored anti-quark to be "white". Baryons must have all three colors to make up white, like in the TV-screen. Thus no quark or gluon can exist as a free particle – this is called *confinement*. Since, due to the self-interaction of the gluons, the potential between the color charges will increase with distance, new quark–anti-quark pairs will be produced out of the vacuum when a quark is knocked out of a baryon or meson. Together with the knocked out quark and the rest of the hadron, the produced quark–anti-quark pairs will form colorless particles. This process is known as *hadronization* or *fragmentation*. In accelerator experiments, this leads to so called particle jets, since the hadrons that have been formed travel almost in the direction of the primary quark.
Another important effect of the gluon self coupling is the running coupling constant. The strong coupling α_s is energy dependent (just like the electromagnetic and the weak coupling, but stronger). With Q being the exchanged four-momentum in a hard scattering process, one has to leading order [Gri87]:

$$\alpha_s(Q^2) = \frac{\alpha_s(Q_0^2)}{1 + \frac{(33-2n_f)}{12\pi}\alpha_s(Q_0^2)\ln\frac{Q^2}{Q_0^2}} = \frac{12\pi}{(33-2n_f)\ln\frac{Q^2}{\Lambda^2_{QCD}}} \tag{1.1}$$

or equivalently, when the strong coupling is known at a reference scale Q_0,

$$\Lambda^2_{QCD} = Q_0^2 \exp\frac{-12\pi}{(33-2n_f)\alpha_s(Q_0^2)} \tag{1.2}$$

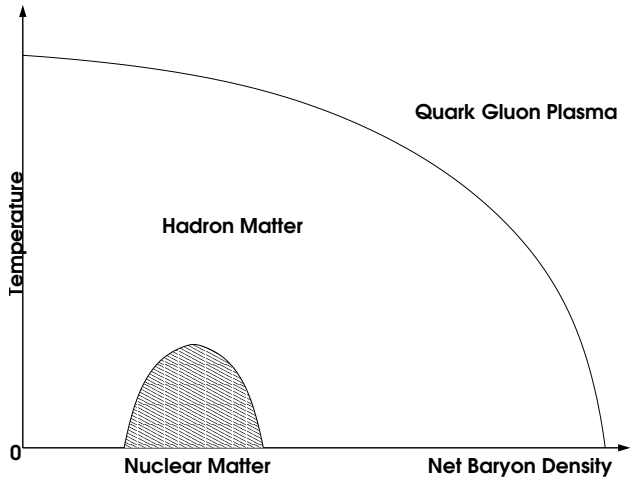

Figure 1.3: Qualitative picture of the hadron matter phase diagram in the temperature – net baryon density plane. The shaded area indicates the nuclear matter region.

The value of the QCD scale Λ_{QCD} is in the range 100-500 MeV and depends on the number of active flavors n_f, which satisfy $(2m_f)^2 < Q^2$.
A problem of this running coupling constant is that it diverges at energies $E \approx \Lambda_{QCD}$ and below, hence perturbative methods cannot be used in that regime. Unfortunately most QFTs are based on such methods, leaving this regime of $E < \Lambda_{QCD}$ mainly to phenomenological models.
In the parton model of the nucleon (see *e.g.* [Pov95]), in addition to the so called valence quarks there is a sea of gluons, other quarks and anti-quarks, produced from vacuum fluctuations of the gluon field. These quarks are called sea quarks. The fraction of the nucleon four-momentum carried by one parton, *i.e.* one quark or gluon in the hadron, is called x. The distributions of the different kinds of quarks are described by two structure functions in x and Q^2. These functions can be measured by deep inelastic scattering, *i.e.* colliding electrons, positrons or neutrinos with nucleons. The DESY experiments H1 and ZEUS have made important contributions to the measurement of these functions.
The quark-confinement makes it difficult to define a quark mass due to the conceptual problem to define the mass of a field that does not exist as a free particle. There are two important definitions, the bare mass and the constituent mass. The bare mass used in perturbative calculations is the mass of the quark in the $Q^2 \to \infty$ limit, seen in scattering processes on the quarks. The constituent mass on the other hand, is the mass of the quarks seen in hadron spectroscopy. In Table 1.4 the quark masses are listed.

In the early universe as well as in collapsed stars and high-energy heavy-ion collisions one expects to find a phase of hot, dense matter of deconfined

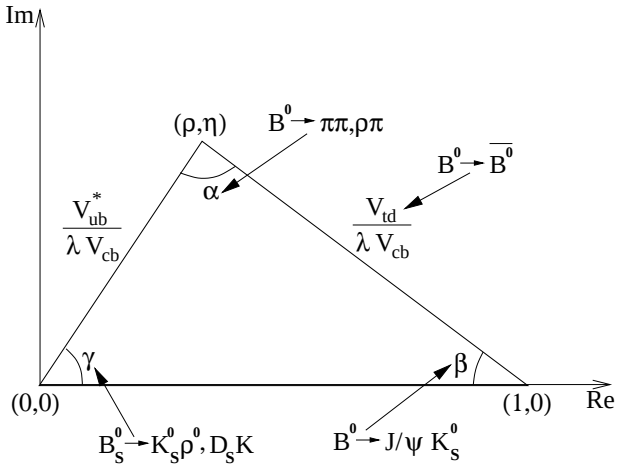

Figure 1.4: The unitarity triangle. Ways to access angles and side lengths are indicated.

quarks and gluons, called **Q**uark **G**luon **P**lasma (QGP) [Won94], [Koc86]. In QGP the energy density is so high, that quark pairs can be created out of the vacuum and all quarks and gluons are in thermal equilibrium. An introduction to the QGP can be found in [Won94].
In Figure 1.3 the expected phase diagram of the hadronic matter in the temperature–baryon density plane is shown. The QGP is expected to exist outside the outer curved line in this figure. Within this line is the area of hadron matter. The shaded area indicates the region of common nuclear matter. There are two conditions under which QGP can be formed. One is the hot QGP, where the energy density due to the temperature is high enough to deconfine the quarks and gluons. The other possibility is the baryon rich plasma. Here the Fermi pressure due to the d- and u-quark densities can deconfine the quarks and gluons. For QGP with zero net baryon number, lattice gauge calculations give critical temperatures at which the plasma is formed of about $T_c \approx 210$ MeV [Won94].

1.1.3 CP-Violation

As stated before, symmetry is very important in physics. Three important discrete symmetries are the time inversion (T), space inversion or parity (P) and particle anti-particle exchange (C). The T operation lets the time flow backwards, P exchanges the spatial coordinates $\vec{x}$ by $-\vec{x}$ and C exchanges every particle by its anti-particle, flipping the sign of every additive quantum number. Until the early 1950's it was believed that C, P and T are conserved by all forces. But 1956 Lee & Yang pointed out, that parity conservation was never tested for the weak interaction. Just one year later, Wu could demonstrate that indeed P is maximally violated in the charged current weak interaction, *i.e.* an exchange of a W^+ or W^-. The neutral current

(Z) has a coupling to the electromagnetic current, which is not P-violating [Nac91]. In 1964 Fitch and Cronin discovered that CP was violated in the $K^0 - \overline{K^0}$-system in the order of 10^{-3} (for reference to these dates see *e.g.* [Fra87]). Note however that for a local, Lorentz invariant QFT CPT invariance holds [Nac91].
What is so interesting about CP-violation? In some early phase of the universe matter was produced, but more matter than anti-matter — at least locally — since there is no evidence for anti-matter anywhere in the near universe. In a thermodynamic model of the universe without CP-violation, the matter density would be much lower than observed [Ste02], since, if CP-symmetry holds, then the same amount of matter as anti-matter must have been produced. Actually, CP-violation can be implemented in the Standard Model, but this seems not to be enough to account for the matter–anti-matter asymmetry needed [Ste02].
This is how CP-violation enters the Standard Model:
In charged weak interactions, quarks can change not only their flavor (u, d,c,s,t,b) but also their family. This is described by the so called **C**abbibo **K**obayashi **M**askawa - matrix (CKM). It connects the mass eigenstate (d, s, b) with the weak eigenstate (d', s', b'):

$$\begin{pmatrix} d' \\ s' \\ b' \end{pmatrix} = \begin{pmatrix} V_{ud} & V_{us} & V_{ub} \\ V_{cd} & V_{cs} & V_{cb} \\ V_{td} & V_{ts} & V_{tb} \end{pmatrix} \begin{pmatrix} d \\ s \\ b \end{pmatrix} \tag{1.3}$$

This matrix can approximately be parametrized by three real (λ, A, ρ) and one imaginary $(i\eta)$ parameters, as done in the Wolfenstein parametrization [Wol83]:

$$V = \begin{pmatrix} 1 - \frac{\lambda^2}{2} & \lambda & \lambda^3 A(\rho + i\eta) \\ -\lambda & 1 - \frac{\lambda^2}{2} & \lambda^2 A \\ -\lambda^3 A(1 - \rho - i\eta) & -\lambda^2 A & 1 \end{pmatrix} + \mathcal{O}(\lambda^4) \tag{1.4}$$

CP-violation arises from the imaginary parameter $(i\eta)$. This matrix has to be unitary: $V_{ik}^\dagger V_{kj} = \delta_{ij}$. From this relation, we extract one line, namely: $V_{ud}V_{ub}^* + V_{cd}V_{cb}^* + V_{td}V_{tb}^* = 0$. Using the Wolfenstein parametrization (neglecting terms of $\mathcal{O}(\lambda^5)$) and dividing by $\lambda^3 A$, we get: $(\rho + i\eta) - 1 - (1 - \rho - i\eta) = 0$. This relation can be visualized as the so called "unitary triangle" in the complex plane (see Fig. 1.4): $\frac{V_{ub}^*}{\lambda^3 A} + \frac{V_{td}}{\lambda^3 A} = 1$. The other unitary relations lead to triangles, all of which are very flat except for one. If the triangle is not degenerated to a line, CP is violated. On the other hand if measurements show that the angles don't add up to 180° or the side lengths don't fit, this is an indication for physics beyond the Standard Model.
The experiments BaBar at SLAC in the USA and Belle at KEK in Japan have meanwhile measured the β-angle, *e.g.* BaBar: $\sin 2\beta = 0.742 \pm 0.067(\text{stat.}) \pm 0.033(\text{syst.})$ [Aub02].

1.2 Models of Strangeness Production

Since this thesis deals with strange particle production in high-energy particle collisions, some models of strangeness production will be presented below. This section is split into two parts, one about strangeness production in heavy-ion collisions and one about strangeness production in hadron collisions. In the heavy-ion collisions case, QGP is expected to be created and thus the models differ from the hadron case.

1.2.1 Strangeness Production in Heavy-Ion Collisions

To probe the properties of QGP, high-energy heavy-ion collisions will be used. The reason why QGP is expected to be formed in high-energy heavy-ion collisions is the large stopping power of the nucleons, *i.e.* that due to large cross sections of the nucleons they undergo multiple scatterings and get stopped. This leads to the formation of a fireball. In addition, the Lorentz contraction of the nuclei makes them flat oblate ellipsoids, leading to a small flat fireball with an even higher energy density [Won94]. The stopping power is so strong that in the region of center of mass energies of $\sqrt{s} \sim 5 - 10$ GeV per nucleon the nucleons are expected to be stopped completely and to form a baryon rich QGP. At even higher energies of more than $\sqrt{s} \sim 100$ GeV the baryons cannot be stopped any more and a QGP with zero net baryon number will be formed.
It is difficult to identify the formation of QGP unambiguously due to the possible formation of a hadron gas with similar properties. As possibilities for such an identification, different signatures have been proposed, such as:

- di-lepton production
- J/ψ suppression
- photon production
- pion momentum correlations
- enhanced strangeness production

For this work only the strangeness production signature is of importance and will be described. Descriptions of the other signatures can be found *e.g.* in [Won94].

Hyperons and anti-Hyperons from QGP

The descriptions given in this subsection is based on [Won94] and [Koc86]. The time scale of the QGP life time in nucleus-nucleus reactions is expected to be of the order of 10^{-23} s. Since this is much smaller than the typical timescale of weak interactions (10^{-10} s), strict strangeness conservation is

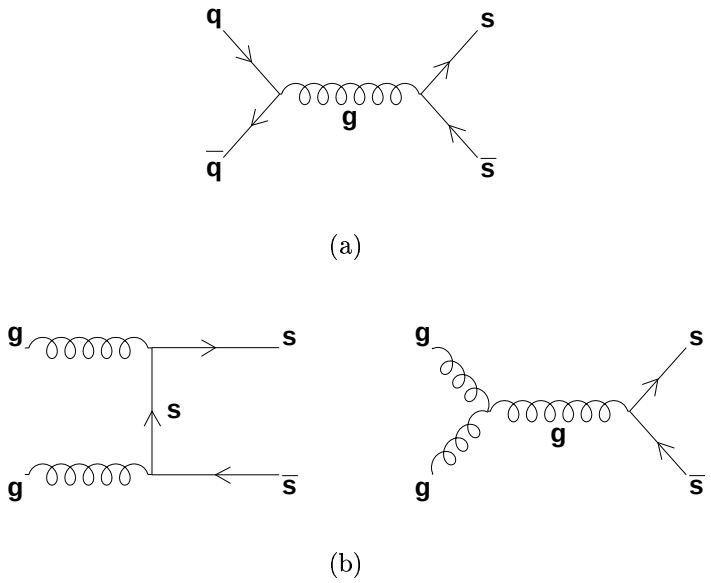

Figure 1.5: The Feynman diagrams that describe how pairs of strange–anti-strange quarks can be produced in QGP: a) $s\bar{s}$-quark pair from quark annihilation b) $s\bar{s}$-quark pair by gluon fusion.

assumed here. After this time period of about 10^{-23} s, the plasma reaches the critical temperature or baryon density and transforms into a hot and dense hadron gas.
Since the temperature in QGP is larger than the strange quark mass, strange quark–anti-quark pairs can be produced. The leading order Feynman diagrams are shown in Figure 1.5. There are two different processes: $q\bar{q} \rightarrow s\bar{s}$ and $gg \rightarrow s\bar{s}$. By using Feynman calculus, the cross sections of these processes can be calculated and turn out to be of the same order of magnitude. Due to the fact that there are eight different gluons, but only two different light quarks, the rate of strangeness production by gluons dominates. This can also be used to separate the QGP from the hadron gas, since in a hadron gas there are no free gluons and interacting hadrons underlie the restriction to build up hadrons in the final state of each interaction.
So from the point of time, when QGP is formed, s- and $\bar{s}$-quarks are produced until they fill up their phase space. There are two types of equilibriums that are important in this context. First there is the thermal equilibrium, that is reached when all particle types still interact and have the same momentum distribution. It is established very soon after the formation of the QGP. It is however not absolutely clear if the chemical equilibrium, *i.e.* the point where the phase space for each particle is filled up, is reached within the lifetime of the plasma. For a hadron gas there are good indications that this is not the case. The chemical equilibrium is established when the densities of the particle types, and thus their chemical potential as well, reach a steady

level while the particles still transform into one another. The equilibration time is estimated to be $\tau \sim 10$ fm/c $\approx 3 \cdot 10^{-23}$ s, when a temperature of $T = 200$ MeV is assumed. On the other hand the typical interaction times in high-energy heavy-ion collisions are in the order of $5 - 10$ fm/c. So at about $T = 200$ MeV the chemical equilibrium, and thus the saturation of the phase space with s- and $\bar{\text{s}}$-quarks, may not be reached. Calculations show, that this should definitely be the case for $T = 400$ MeV.
If we assume that the chemical equilibrium is reached, estimates of the relative number densities for the different kinds of quarks can be made. The outcome is that at zero net baryon density, we find for the number densities $n_s = n_{\bar{s}} \approx n_d = n_{\bar{d}} \approx n_u = n_{\bar{u}}$. The first equality is obvious, since we assume strangeness conservation. This means for the chemical potentials: $\mu_s = 0$ and $\mu_d = \mu_u = \mu_B = 0$, where the μ_B denotes the baryon chemical potential. In the case of a net baryon number, we have: $\mu_B \neq 0$, $n_s < n_d$, $n_s < n_u$, but $n_s > n_{\bar{d}}$ and $n_s > n_{\bar{u}}$. The relations $n_s = n_{\bar{s}}$, $\mu_s = 0$ still hold. Anyway, the number of strange and anti-strange quarks relative to the number of d- and u-quarks is much higher than in a hadron gas. And since, unlike in the case of a hadron gas, there are a lot more $\bar{\text{u}}$- and $\bar{\text{d}}$-quarks around in QGP, strange anti-baryons like $\overline{\Lambda}$, $\overline{\Xi}$ or $\overline{\Omega}$ can be formed more easily. Strange baryons can be created in a hadron gas by producing an $\text{s}\bar{\text{s}}$-quark pair and taking u- and d-valence quarks from a hadron. But for strange anti-baryons, pairs of $\text{d}\bar{\text{d}}$- or $\text{u}\bar{\text{u}}$-quarks have to be created. Thus an enhancement of anti-hyperon production in QGP, especially with multiple strangeness, is expected and can be observed in an enhancement of the ratios of anti-hyperon numbers of one type to the number of hyperons of the same type, like $\frac{\overline{\Lambda}}{\Lambda}$, $\frac{\overline{\Xi}}{\Xi}$ and $\frac{\overline{\Omega}}{\Omega}$. Due to the large number density of s-quarks, hyperons with multiple strangeness are more abundant in the QGP, and therefore ratios like $\frac{\Xi^-}{\Lambda}$ ($\frac{(ssd)}{(uds)}$) are enhanced with respect to the hadron gas case. These effects are not expected to be affected by interactions within the hadron gas that is formed after the QGP.

Anti-Baryon to Baryon Ratio Predictions for deconfined Quarks

There are also more quantitative predictions. For example the coalescence model ([Bia98] and [Zim00]) is a simple model that predicts a relation between the anti-baryon to baryon ratios of different hyperon types in the case of a hadronization from unconfined quarks, *i.e.* neglecting the gluonic degrees of freedom. Please mind, that the latter would be *very important* in the case of QGP formation and *not* negligible. This model is independent of any thermal or chemical equilibrium. The starting assumption is that the probability for the creation of a (anti-)baryon is proportional to the probability to find the three corresponding (anti-)quarks in the same small phase-space volume. Just this simple assumption leads to the relations between the anti-baryon–baryon ratios, even when we take into account the fact that

the numbers of different quark types must not change in the hadronization process. Formally, we get:

$$p = \omega_p (b_q q)^3; \quad \Lambda \text{ or } \Sigma = \omega_\Lambda (b_q q)^2 (b_s s);$$
$$\Xi = \omega_\Xi (b_q q)(b_s s)^2; \quad \Omega = \omega_\Omega (b_s s)^3 \tag{1.5}$$

where the ω parameters are the probabilities to form the baryon and are assumed to be equal for particle and anti-particle. Where q is the density of the light and s the density of the strange quarks. The b_x are adjusted such that flavor is conserved. With $b_x = 1$ for all x, we get the linear model [Bia98]. So Equation 1.5 is called the non-linear coalescence model [Zim00], having strict strangeness conservation but giving the same results for the anti-baryon–baryon ratios as the linear model:

$$\frac{\bar{p}}{p} = \frac{\bar{q}^3}{q^3}; \quad \frac{\overline{\Lambda \text{ or } \Sigma}}{\Lambda \text{ or } \Sigma} = \frac{\bar{p}}{p} D; \quad \frac{\overline{\Xi}}{\Xi} = \frac{\bar{p}}{p} D^2; \quad \frac{\overline{\Omega}}{\Omega} = \frac{\bar{p}}{p} D^3; \quad D = \frac{b_q q \cdot b_{\bar{s}} \bar{s}}{b_{\bar{q}} \bar{q} \cdot b_s s} \tag{1.6}$$

By the way, since this model only counts quarks, it cannot distinguish between Λ and $\Sigma^{0/-/+}$ or between Ξ^- and Ξ^0, which have the same quark content if we set $q = d = u$. If these ratios are measured, three values of D can be calculated that should agree in case of the production of a phase where quarks are deconfined.

1.2.2 Strangeness Production in Hadron Collisions

Since light hadrons are QCD bound states of light particles, the perturbative method cannot describe them. As perturbative QCD cannot describe fragmentation either, the problem of the formation of strange hadrons from hadron-nucleon reactions is left mostly to phenomenological models. For example in a paper about strange–anti-strange particle asymmetries in pion-proton collisions [Gut02], the main points in modeling strangeness production and its x_f distribution (x_f is defined below) in hadron-nucleon reactions are described as follows.

Often Used Dynamic Variables

In this discussion, as well as later, four important kinematic variables are used:

1. **Feynman x**

$$x_f = \frac{p_{z\text{cm}}}{p_{z\text{max,cm}}} \approx \frac{2 p_{z\text{cm}}}{\sqrt{s}} \tag{1.7}$$

where $p_{z\text{cm}}$ is the longitudinal-component of the particle momentum in the center of mass system and $\sqrt{s}$ is the center of mass energy. The

maximally possible $p_{z\mathrm{cm}}$ is denoted with $p_{z\mathrm{max,cm}}$.

2. **rapidity**

$$y = \frac{1}{2} \ln \frac{E + p_z}{E - p_z}. \tag{1.8}$$

where E is the energy and p_z the longitudinal-component of the momentum of the particle. The rapidity has the property that differences of rapidities are Lorentz invariant, which means that rapidity in the lab frame is related to rapidity in the center of mass frame just by an additive constant [Won94]. In this thesis y will stand for the rapidity in the center of mass system.

3. **transverse momentum**
The transverse momentum p_t is the absolute value of the momentum in the transverse plane.

4. **azimuthal angle ϕ**

$$\tan \phi = \frac{p_y}{p_x} \tag{1.9}$$

with p_x and p_y being the momentum components of the transverse plane.

The intrinsic Particle Model

There are two main processes by which strange and anti-strange quarks can be created. One is parton annihilation as in QGP, depicted in Figure 1.5, the other is hadronization of a sea s- or $\bar{\mathrm{s}}$-quark from one of the hadrons.

We will consider the annihilation, also called **leading twist production**, first. Although it is not absolutely clear whether a perturbative method is allowed in spite of the low strange quark mass, such an approach is used. The point is that $\Lambda_{QCD} \approx 100$ MeV, for $n_f = 3$ [Koc86], is in the order of the lower edge of the strange mass range. As stated in Section 1.2.1, perturbative QCD can calculate those cross sections on the parton level. To describe them at the hadron level, one has to know the x distributions of the partons in the hadrons and their fragmentation probabilities. These are given by structure functions and fragmentation functions. The structure functions already mentioned in Section 1.1.2 are known from deep inelastic scattering. The hadronization functions on the other hand describe the probability that a quark hadronizes into a certain hadron. Equal probabilities for all possible strange hadrons are assumed.

The hadronization from sea s- or $\bar{\mathrm{s}}$-quarks, so called **"intrinsic"** quarks, is described by a Fock state of the hadron that contains a sea $\mathrm{s}\bar{\mathrm{s}}$-quark pair, like

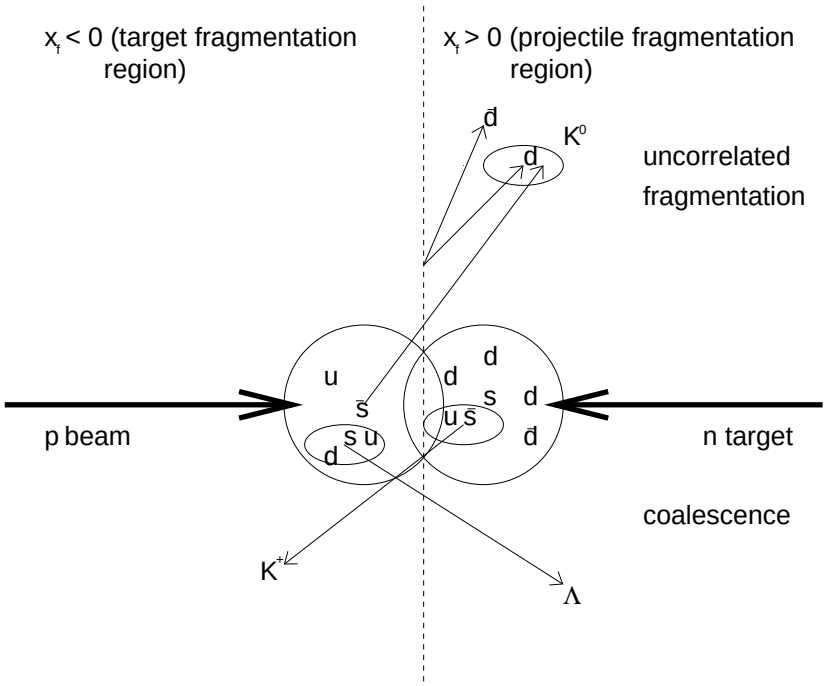

Figure 1.6: The intrinsic particle production is illustrated here in the center of mass system of a proton–neutron collision. The right side comprises the so called projectile fragmentation region, the left side is the target fragmentation region – the neutron is the target here. In the upper half a kaon production by uncorrelated fragmentation is shown – the $d\bar{d}$ is created by a gluon out of the vacuum. The lower half shows particle productions by coalescence, *i.e.* the valence quarks of the K^+ and the Λ preexist in the nucleon.

$|uuds\bar{s}\rangle$ for a proton. A collision with another hadron breaks the coherence of this Fock state and the strange and the anti-strange quark can hadronize. All kinds of quark pairs can exist in such a Fock state, but more massive pairs are less probable. States with more than one sea quark pair are also possible, but less likely than states with a lower number of sea-quark pairs. A general Fock state is written as $|n_v r_s(s\bar{s})r_u(u\bar{u})r_d(d\bar{d})\rangle$ with $r = r_s + r_u + r_d$ the number of sea quark pairs and n_v the number of valence (anti-)quarks, *i.e.* $n_v = 2$ for mesons and $n_v = 3$ for baryons. Such a state is made up of $n = n_v + 2r$ quarks and anti-quarks.

There are two possibilities for a strange hadron to emerge from hadronization of such a Fock state. Either it hadronizes **uncorrelatedly** by drawing $q\bar{q}$-quark pairs out of the vacuum, or it hadronizes by **coalescence**, *i.e.* like in the phase of deconfined quarks, where three quarks that already exist in the Fock state form a baryon, or a quark and an anti-quark from the Fock state form a meson, as seen in Figure 1.6. Quarks that have preexisted in one of the colliding particles as valence quarks and are later part of a prod-

uct particle are called leading particles. For r=1, *i.e.* one sea-quark pair in the Fock state, *e.g.* $|n_v s\bar{s}\rangle$, not all strange hadrons can be formed without additional strangeness production, leading to enhancement of those that can be formed. This is called the leading particle effect. It depends also on x_f, becomes weaker for r=2 and almost vanishes for r=3. The assumption that the longitudinal momentum of such a quark does not change by a large amount leads to the definition of the fragmentation regions. For example in the reaction proton on neutron where the proton is the incident beam particle and the neutron the fixed target particle, the kinematic region where intrinsic particles from the proton can be found, is called the proton or projectile fragmentation region (see Fig. 1.6). It is defined by $x_f > 0$, where x_f is the Feynman x of the produced particle. Equivalently, $x_f < 0$ is called the target fragmentation region. As an approximation one can assume that even in the region near $|x_f| = 0$ no hadrons mixed from quarks of both reacting particles are found.
For the full production cross section for one strange hadron S, the two processes, *i.e.* leading twist and intrinsic particle production, have to be added:

$$\frac{d\sigma^S_{hN}}{dx_f} = \frac{d\sigma^S_{lt}}{dx_f} + \frac{d\sigma^S_{iQ}}{dx_f}. \tag{1.10}$$

1.3 Measurements concerning Strangeness Production

In the QGP research a lot of work has been done at CERN, namely the NA and WA experiment series. Especially using the new RHIC heavy ion collider at Brookhaven, an unambiguous discovery of QGP is expected in the near future. This section deals with a small fraction of chosen experimental data and their interpretation. The last section will address particle–anti-particle asymmetries in hadron-nucleus collisions.

1.3.1 Extrapolation Formula and older Proton-Nucleus Experiments

To observe an enhancement in hyperon ratios as a signature for QGP in nucleus-nucleus reactions, reference values have to be known from proton-nucleus and proton-proton reactions. To make a meaningful comparison between the ion collisions and the proton-nucleon collisions data, they should lie in the same kinematic region. In order to compare older data from proton-nucleus and proton-proton collisions at $x_f > 0.2$ with data from heavy-ion rection at $y_{cms} \sim 0$, implying $x_f \sim 0$, an extrapolation model is used. This model was proposed by the authors in [Kac97] and used on available data.
With the invariant differential cross section $E\frac{d\sigma}{dp}(pA \to c) := I(pA \to c)$ of

the reaction proton on nucleus creating c, they used the factorization

$$I(pA \to c) = I(pp \to c) \cdot F(A) \tag{1.11}$$

to compare all data from different kinds of target nuclei, including protons. The function F(A) contains a factor $A^{\alpha(p)}$, where $\alpha(p)$ is momentum dependent and assumed to be the same for all hyperons for $p_t < 1$ GeV. This leads to the absence of an A dependence for the particle ratios. The x_f and p_t dependence is modeled as follows:

$$I(pp \to c) = B_c \cdot (1 - x_f)^{\beta_c} g(m_c, p_t) \tag{1.12}$$

where β_c is taken from experiments for different particles c. B_c is a normalization factor. For the function $g(m_c, p_t)$ a thermal distribution $\sim \exp(-\frac{m_t}{T})$ with $m_t = \sqrt{m_c^2 + p_t^2}$ and $T = 120$ MeV was used.

An overview of the ratios of main interest here, calculated from different experiments and extrapolated to $x_f = 0$, $p_t = 0$ according to Equation 1.12 are listed in Table 1.5. Indeed measurements near $|x_f| = 0$ were also found, as indicated in the last column of the table, supporting this model. So for $x_f = 0$, $p_t = 0$ and beam momentum p ranging from 200 GeV to 800 GeV, the anti-hyperon to hyperon ratios are around or larger than 0.3, whereas the ratios of different kinds of particles are below 0.1. The authors conclude that an enhancement due to QGP is more likely to be seen for ratios of particles containing different numbers of strange quarks than in anti-hyperon to hyperon ratios.

1.3.2 Anti-Hyperon to Hyperon Ratios at WA85 and WA94 — Hadron Gas, QGP

The experiments WA85 [Aba97a] and WA94 [Aba97b] were fixed target experiments at CERN at 200 GeV per nucleon beam energy, using the OMEGA spectrometer. WA85 used protons and sulfur ions as beam particles and tungsten as the target material. WA94 used the same beam particles, but sulfur as target material. The main results regarding strangeness production are listed in Table 1.6. From the table it is seen that most ratios agree within errors for proton and heavy-ion collision. Only the ratio $\frac{\overline{\Xi^-}}{\overline{\Lambda}}$ is in both experiments 30–40% larger in ion-collisions than in the proton-nucleus collisions, supporting the suspicion of Section 1.3.1 that an enhancement due to QGP is more likely to be seen for ratios of particles containing different numbers of strange quarks than in anti-hyperon to hyperon ratios.

In [Dov95], those results (in a preliminary version) by WA85 are used to test some models. The author arrives at the result that the data seems to fit well into the hadron gas model, giving a similar temperature $T \approx 200$ MeV

ratio	beam momentum [GeV]	value	target materials	extra-polated?
$\frac{\overline{\Lambda}}{\Lambda}$	24	0.0140 ± 0.0061	p	no
	60	0.110 ± 0.041	Au	no
	200	0.45 ± 0.20	Be	yes
		0.18 ± 0.11	Au	no
		0.346 ± 0.092	Pb	no
		0.259 ± 0.059	S	no
	300	0.572 ± 0.040	Be, Cu, Pb	yes
	400	0.531 ± 0.044	Be	yes
		0.5 ± 0.1	p	no
	$\sqrt{s} = 31 - 53$	0.67 ± 0.14	p	no
	$\sqrt{s} = 63$	0.63 ± 0.17	p	no
		0.58 ± 0.16	p	yes
$\frac{\overline{\Xi^-}}{\Xi^-}$	800	0.62 ± 0.05	Be	yes
$\frac{\overline{\Omega^-}}{\Omega^-}$	800	0.55 ± 0.15	Be	yes
$\frac{\Omega^-}{\Xi^-}$	800	0.042 ± 0.002	Be	yes
$\frac{\overline{\Omega^-}}{\overline{\Xi^-}}$	800	0.056 ± 0.004	Be	yes

Table 1.5: Some results on hyperon ratios from [Kac97] using Formula 1.12, or measured in the region $x_f \approx 0$. In the last column is stated whether the data was taken at mid-rapidity or extrapolated. Where more than one measurement was used, the weighted average is given. Where $\sqrt{s}$ instead of the beam momentum is given the data comes from a collider experiment.

ratio	pW (WA85) [Aba97a]	SW (WA85) [Aba97a]	pS (WA94) [Aba97b]	SS WA(94) [Aba97b]
$\frac{\overline{\Lambda}}{\Lambda}$	0.20 ± 0.02	0.20 ± 0.01	0.22 ± 0.01	0.23 ± 0.01
$\frac{\overline{\Xi^-}}{\Xi^-}$	0.47 ± 0.07	0.47 ± 0.06	0.46 ± 0.05	0.55 ± 0.07
$\frac{\Xi^-}{\Lambda}$	0.070 ± 0.006	0.097 ± 0.006	0.078 ± 0.004	0.09 ± 0.01
$\frac{\overline{\Xi^-}}{\overline{\Lambda}}$	0.16 ± 0.02	0.23 ± 0.02	0.16 ± 0.02	0.21 ± 0.02

Table 1.6: Hyperon ratios obtained at WA85 and WA94 for proton-tungsten, sulphur-tungsten, proton-sulphur and sulphur-sulphur interactions. The values are taken at mid rapidity which corresponds to $2.3 < y_{\text{lab}} < 3.0$ for WA85 and $2.5 < y_{\text{lab}} < 3.0$ for WA94. In the transverse momentum range 1.2 GeV $< p_t <$ 3.0 GeV.

and baryon chemical potential $\mu_B \approx 320$ MeV for all strange particles, but with some inconsistencies. One is that the calculated temperature lies well within the suspected region of QGP.
For the fit to a QGP-model on the other hand, the vanishing strangeness content correctly yields $\frac{\mu_s}{T} = 0.03 \pm 0.05$, as well as the strong saturation of the strange quark phase space $\gamma_s = 0.55 \pm 0.04$. As suspected at these beam energies, a non vanishing light quark, and thus baryon chemical potential is found: $\frac{\mu_q}{T} = 0.39 \pm 0.04$. Altogether the data is consistent with the QGP-model, although some assumptions still have to be made. In the paper it is concluded that the formation of QGP is plausible but not proven for this data.

1.3.3 Anti-Hyperon to Hyperon Ratios at NA44, NA49, WA97 and STAR — Coalescence

In the paper [Bia98] cited before in section 1.2.1 all available data by that time concerning anti-hyperon to hyperon ratios, taken from the papers of the collaborations NA44 [Kan97], NA49 [Bor97] and WA97 [Cal99], are collected, shown here in Table 1.7. These are CERN experiments using the SPS accelerator at 158 GeV per nucleon beam energy.
For these data proton and lead beams on lead targets were used. As can be seen, the coalescence model describes the Pb-Pb data well, but fails in the case of the p-Pb data, since the D-values in the right three columns of the table agree for Pb-Pb, but not for p-Pb. Data for sulfur-sulfur reactions were taken also. They still fit the model, but not as well. Remember that the non-linear coalescence model gives the same values for these ratios as the linear one. It is concluded that the coalescence model is in agreement with the SPS data from nucleus-nucleus interaction, but is not in agreement with the proton-nucleus interactions. In [Zim00] where the authors present the non-linear model, they also give a time duration $\delta\tau \approx 1.5\frac{\text{fm}}{c}$ for the hadronization based on the model. This excludes a long living mixed phase of QGP and hadron gas.

The **R**elativistic **H**eavy **I**on **C**ollider (RHIC) has been built at Brookhaven National Laboratory mainly to search for QGP signatures. There are now first preliminary data available. The authors of [Zim00] used such preliminary data on anti-hyperon to hyperon ratios by the STAR collaboration to probe the non-linear coalescence model – here also called **AL**gebraic **CO**alescence in **R**ehadronization (ALCOR) [Zim01]. By solving the reaction equations in Equation 1.5, this model can make quantitative prediction of those ratios. In Table 1.8, the preliminary STAR data, taken at $\sqrt{s} = 130$ GeV per nucleon, is compared to the model predictions. From the data in this table, one can also see, that the ratios are correct. The authors conclude that, as in the case of SPS energies, a phase of quark matter is produced, where the quark degrees of freedom dominate. This quark matter then hadronizes

reaction	measured ratio				w/ coalescence model		
	$\frac{\overline{\Lambda}\text{or}\overline{\Sigma^0}}{\Lambda\text{or}\Sigma^0}$	$\frac{\overline{\Xi^-}}{\Xi^-}$	$\frac{\overline{\Omega^-}}{\Omega^-}$	$\frac{\overline{p}}{p}$	D_Λ	D_Ξ	D_Ω
Pb-Pb	0.133	0.249	0.383	0.07	1.9	1.89	1.76
	$\pm$0.007	$\pm$0.019	$\pm$0.081	$\pm$0.01	$\pm$0.3	$\pm$0.15	$\pm$0.15
p-Pb	0.20	0.33	—	0.31	0.65	1.03	—
	$\pm$0.3	$\pm$0.03	—	$\pm$0.03	$\pm$0.11	$\pm$0.07	—

Table 1.7: Anti-baryon to baryon ratios obtained at NA44, NA49 and WA97 for central rapidity at 158 A GeV. There was no data available for Ω-ratios in p-Pb interactions. The three right columns give the values calculated by the coalescence model as described in section 1.2.1 according to Formula 1.6. Numbers are taken from [Bia98].

	ALCOR model	STAR data
$\frac{\overline{p}}{p}$	0.63	0.61 ± 0.06
$\frac{\overline{\Lambda}}{\Lambda}$	0.72	0.73 ± 0.03
$\frac{\overline{\Xi^-}}{\Xi^-}$	0.83	0.82 ± 0.08
$\frac{K^+}{K^-}$	1.13	1.12 ± 0.06
$\frac{K^+}{\pi^+}$	0.142	0.15 ± 0.01

Table 1.8: Preliminary baryon to anti-baryon ratios obtained by the STAR collaboration at RHIC, compared to the non-linear coalescence model (ALCOR). The data was taken in Au-Au collisions of $\sqrt{s} = 130$ GeV per nucleon. Numbers are taken from [Zim01]

.

in a time scale shorter than the expected time scale of QGP. On the other hand, in contrast to the SPS data, there is also evidence by jet quenching for liberation of the gluonic degrees of freedom as expected for QGP. But this is supposed to happen in an earlier stage of the collision.

1.3.4 Particle–anti-Particle Asymmetries in π-Nucleus Collisions: E791

This last section is about particle–anti-particle asymmetries in pion–nucleus reactions by the Fermilab E791 experiment [Ait00]. This is a fixed target experiment with a 500 GeV π^- beam employing different target materials.

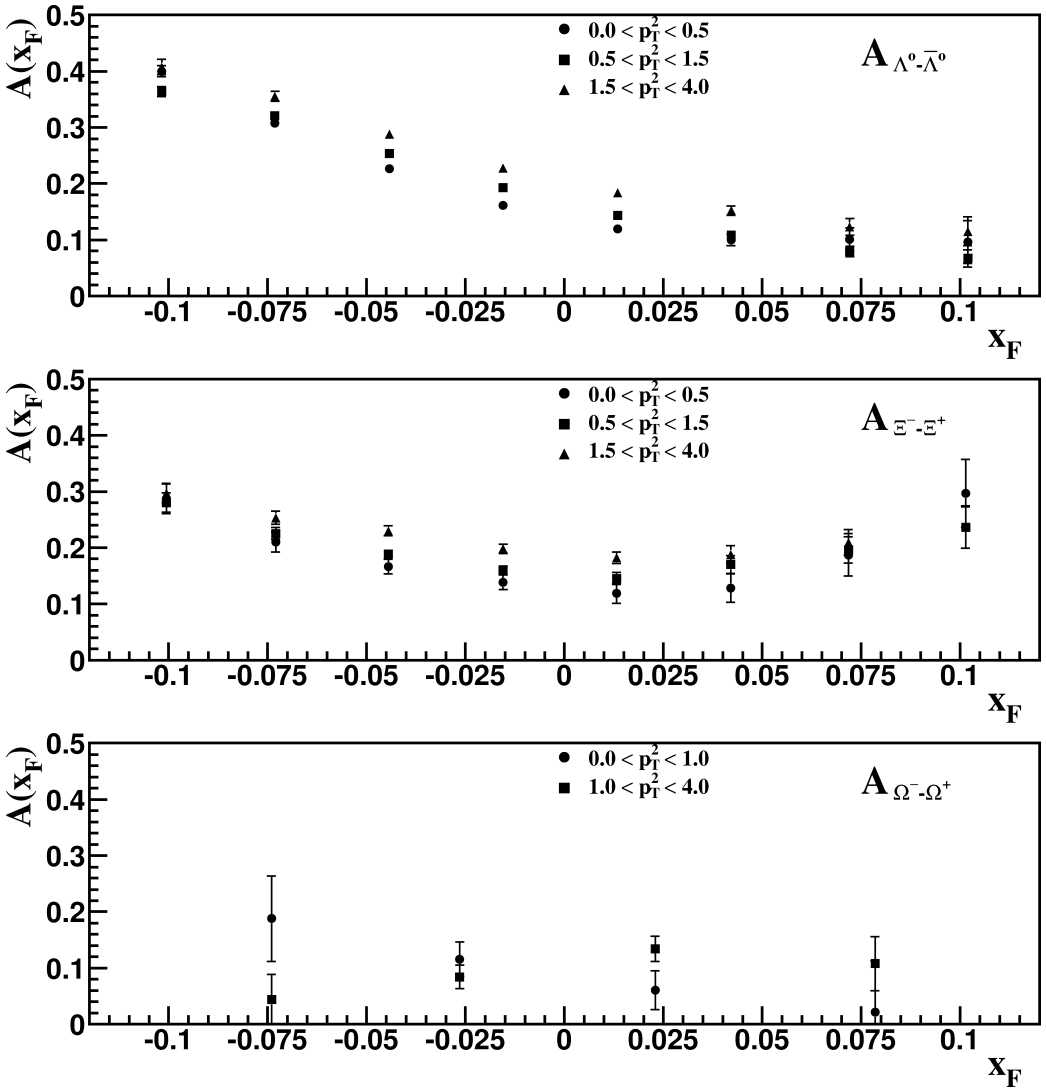

Figure 1.7: Asymmetries of strange to anti-strange baryons of π^--nucleus reactions by E791, plotted against x_f for different p_t. Taken from [Ait00].

The particle–anti-particle asymmetry in x_f is defined by

$$A_Y(x_f) = \frac{\frac{d\sigma^Y}{dx_f} - \frac{d\sigma^{\overline{Y}}}{dx_f}}{\frac{d\sigma^Y}{dx_f} + \frac{d\sigma^{\overline{Y}}}{dx_f}} = \frac{N_Y - N_{\overline{Y}}}{N_Y + N_{\overline{Y}}} \tag{1.13}$$

where $N_Y/N_{\overline{Y}}$ is the acceptance corrected number of hyperons Y/anti-hyperons $\overline{Y}$ and $\frac{d\sigma}{dx_f}$ is the differential cross section. The results by the E791 experiment are plotted in Figure 1.7 for Λ, Ξ^- and Ω^- with different p_t. The data could not be reproduced using the PYTHIA/JETSET model described later in Section 5.1.1. Especially the large asymmetry at $x_f = 0$ was surprising, but can at least partly be explained by the larger energy threshold for the anti-baryon, since for the production of an anti-baryon, an additional baryon has to be produced to conserve baryon number. Leading particle effects can be seen, *e.g.* in the fact that A_Λ is large for $x_f < 0$, *i.e.* in the nucleon fragmentation region, since the nucleon contains both d and u quark needed to form a Λ (uds). On the other hand, the π^- ($d\bar{u}$) does not contain a u quark and thus A_Λ is low in the pion fragmentation region $x_f > 0$. Indeed Gutierrez and Vogt can explain the general trends of this data well with their intrinsic particle model [Gut02] which is based on the ideas discussed in Section 1.2.2.

1.4 Guide to this Thesis

1.4.1 Motivation

From the discussion in Sections 1.3.2 and 1.3.3 one concludes, that the use of hyperon ratios as a signature for QGP is still an open question. HERA-B can provide an additional reference measurement near central rapidity at 920 GeV beam energy, a region that was not yet covered by other proton–nucleus experiments with heavier target nuclei. It can also make another check on the extrapolation formula presented in Section 1.3.1 and its target material independence. A measurement of the particle–anti-particle asymmetry in x_f in the negative x_f region, can also be done. The results should be comparable with those from E791 in the target fragmentation region applying the ansatz from Section 1.2.2.

1.4.2 Structure of this Thesis

This thesis is structured as follows. First, in Chapter 2 a simple model for predicting hyperon ratios in proton–proton reactions based on quark coalescence will be presented. The results were obtained by using a Monte Carlo method. Then in Chapter 3, the HERA-B detector will be introduced with emphasis on the subsystems used for this analysis. How the signals of the Λ,

Ξ and Ω particles are obtained will be described in Chapter 4. The signals will be presented there.
Chapter 5 will start with the description of the Monte Carlo used for the acceptance determination. After a comparison of the Monte Carlo simulated distributions and the distributions in the real data, the analysis is described. This analysis includes hyperon ratios in different kinematic regions, distributions of $\frac{\overline{\Lambda}}{\Lambda}$ and $\frac{\overline{\Xi}}{\Xi}$, and particle–anti-particle asymmetry distributions in x_f for the Λ hyperons. Finally, Chapter 6 will report on the results and discuss them.

Chapter 2

A simple Model to predict Hyperon Production Ratios

In this chapter, a simple model will be presented to predict hyperon ratios in proton–proton collisions. It is based on the idea of coalescence discussed in Sections 1.2.1 and 1.2.2. This model is not meant to produce precise results, but rather to give insight by its simplicity, while still yielding results that are qualitatively right at least for some ratios.

2.1 Idea

The idea behind this model is fairly simple. One counts the combinatorial possibilities to form a hyperon by quark coalescence from the proton Fock state whose coherence is broken in the collision. The assumption is made that no hadrons are formed which contain (anti-)quarks from both beam and target proton. Up to three sea-quark pairs are taken into account, leading to the possibility to have either a baryon and some mesons in the final state or two baryons and an anti-baryon. The probability to have the extra baryon–anti-baryon pair can be accounted for by a free parameter b. For the model, the following probabilities are taken into account: first the probabilities for the different possible Fock states of the proton, *e.g.* $|uuds\bar{s}>$ or $|uudd\bar{d}s\bar{s}>$ (see Table 2.2). Then, since the coalescence model requires the quarks to be close in *phase space*, they must also be close in momentum space, which a priori is less probable if one is a sea-quark and the other one is a constituent-quark. Thus every time a sea-quark pairs up with a constituent-quark, there is a smaller probability a that this happens compared to the case where all sea-quarks pair up with quarks that are also from the sea. This probability a is not known in advance and another free parameter of this model. When calculating the predictions of the model by hand, it makes life much simpler to not to have higher powers of a and to neglect the parameter b. When using a Monte Carlo simulation, these restrictions are not necessary, and the probability b with which an initial state goes to a final state including an

Fock state	# all	# all w/o	hyp.	# hyp. w/	# hyp. w/o
$\|uuds\bar{s}>$	4	1	Λ	2	0
$\|uuds\bar{s}s\bar{s}>$	20	2	Λ	8	0
			Ξ	2	0
$\|uuds\bar{s}s\bar{s}s\bar{s}>$	130	7	Λ	42	0
			Ξ	21	0
			Ω	6	1
			$\overline{\Omega}$	9	1
$\|uuds\bar{s}q\bar{q}>$	40	4	Λ	22	0
$\|uuds\bar{s}s\bar{s}q\bar{q}>$	260	13	Λ	98	0
			Ξ	20	1
			$\overline{\Xi}$	9	1
$\|uuds\bar{s}q\bar{q}q\bar{q}>$	260	13	Λ	70	0
$\|uuds\bar{s}q\bar{q}q'\bar{q}'>$	130	7	Λ	41	1
			$\overline{\Lambda}$	9	1

Table 2.1: The counted numbers of Λ, Ξ^- and Ω^- in the final states for the different initial Fock states. For simplicity, Ξ means Ξ^- and Ω means Ω^-. The second column gives the number of final states for the corresponding initial Fock state of the proton, the third column the number of final states with no crossing. The column before the last column then gives the number of possibilities to form a hyperon with a crossing, the last column the same without a crossing in the state. Particles that were omitted for some Fock states cannot be formed out of it. The last two rows are counted for as one state in Table 2.2, here it is split, where $|uuds\bar{s}q\bar{q}q'\bar{q}'>$ means with $q \neq q'$.

additional baryon–anti-baryon pair instead of forming three mesons, is used as a second free parameter.

2.2 Calculation by Hand

First the numbers of different final states of each initial Fock state as well as the number of the different hyperons in that state are counted. Two numbers for both are needed, one with no "crossings", meaning no sea–quark will be paired up with a constituent–quark, and one with at least one "crossing", as presented in Table 2.1. Then the relative probability for each Fock state is needed. These probabilities are given in [Gut02] and are listed in Table 2.2. These numbers can be understood if the probabilities for the states

Fock state	relative weight
$\|uuds\bar{s}>$	1
$\|uuds\bar{s}s\bar{s}>$	0.285
$\|uuds\bar{s}s\bar{s}s\bar{s}>$	0.081
$\|uuds\bar{s}q\bar{q}>$	0.704
$\|uuds\bar{s}s\bar{s}q\bar{q}>$	0.2
$\|uuds\bar{s}q\bar{q}q'\bar{q}'>$	0.5

Table 2.2: The relative probabilities of the different Fock states including an s-quark. Numbers are taken from [Gut02].

hyperon	term
Λ	$1.229a + 0.001282$
$\overline{\Lambda}$	$0.01026a + 0.001282$
Ξ	$0.07158a + 0.000770$
$\overline{\Xi}$	$0.00615a + 0.000770$
Ω	$0.00311a + 0.000623$
$\overline{\Omega}$	$0.00499a + 0.000623$

Table 2.3: The relative production of the different particles in the manual calculation.

$|uuds\bar{s}s\bar{s}>$ (0.285) and $|uuds\bar{s}q\bar{q}>$ (0.704) compared to that of $|uuds\bar{s}>$ are given, *i.e.* the probability to find an additional $s\bar{s}$- or a $q\bar{q}$-pair in the sea of the proton. Thus the probabilities for the other states are given by multiplying these numbers, *e.g.* the probability for the state $|uuds\bar{s}s\bar{s}s\bar{s}>$ is given by the square of the probability for the $|uuds\bar{s}s\bar{s}>$ state, since it contains one more $s\bar{s}$-pair. From this reasoning we also see that states with more than three sea-quark pairs become more and more improbable.
To obtain the relative normalization between the Fock states the final states containing a "crossing" have to be multiplied by a, and the ones without a "crossing" have to be multiplied by $1-a$.
Now we are ready to put all the numbers together, *i.e.* by adding up the relative yield of a particle for the different Fock states from Table 2.1 times the relative weight of the Fock state (see Tab. 2.2). This gives *e.g.* for the Λs: $(\frac{2}{4}\cdot 1+\frac{8}{20}\cdot 0.285+\frac{42}{130}\cdot 0.081+\frac{22}{40}\cdot 0.704+\frac{98}{260}\cdot 0.2+\frac{70+41}{260+130}\cdot 0.5)\cdot a+\frac{1}{260+130}\cdot 0.5\cdot(1-a)$ $= 1.229a + 0.001282$. The (relative) numbers for the other hyperons are calculated accordingly, the terms are given in Table 2.3.
When now one ratio is given by experiment, a can be calculated and thus the other ratios, which can be compared to the data. This has been done for the WA85 data presented in Table 1.6. From $\frac{\overline{\Lambda}}{\Lambda} = 0.20$, we see that $a = 4.35 \cdot 10^{-4}$. The other results are then (results from WA85 given in parenthesis): $\frac{\overline{\Xi}}{\Xi} = 0.99(0.47)$, $\frac{\Xi}{\Lambda} = 0.54(0.070)$ and $\frac{\overline{\Xi}}{\overline{\Lambda}} = 0.60(0.16)$. These results are not very close to the measured values, since we have simplified an already simple model. It should also be mentioned that the measurements are taken at mid rapidity, whereas the model tries to predict the overall ratios. We will see how ever in the next section that a more realistic Monte Carlo calculation produces much better results.
By taking a neutron as a target, the only minor changes are in the ratios containing a Ξ. This justifies the application of this model to proton–nucleus data.

2.3 Calculation by Monte Carlo Simulation

2.3.1 The Monte Carlo Method

The Monte Carlo method, see *e.g.* [Cow98], is a numerical method to calculate probabilities. The most simple example is the random walk of a particle, *i.e.* its Brownian motion in a gas. This can be simulated by giving the particle from time to time random kicks in different directions — "throwing a dice" to determine the next direction. In general, the Monte Carlo method can calculate probabilities from almost arbitrary probability distributions and functions of those. This is done by generating a random value according to the desired probability density and looking, if the value is within the interesting range, or applying a function to the value as stated above to have a

look at the outcome. This technique has been applied to the model described above.

2.3.2 Rien ne va plus: The Program

The program uses the two free parameters a and b introduced before. First we choose some numbers for a and b. Since the model neglects all kinematics, the program only has to group quarks and count the hyperons in question. The algorithm does for each event the following:

1. Produce a random number to decide on the initial Fock state, using the weights from Table 2.2.
2. If there are three sea-quark pairs, create a baryon–anti-baryon pair with the probability $\boldsymbol{b}$.
   If no baryon–anti-baryon pair is produced then:
   (a) Each anti-quark pairs with a constituent quark with the probability $\boldsymbol{a}$ to form a meson, otherwise it pairs with a sea quark. All eligible quarks are selected with equal probabilities.
   (b) The quarks not used up for the mesons make up the only baryon.
   (c) **Start the simulation of the next event.**
3. If we have a baryon–anti-baryon pair, the anti-baryon consists of the three sea–anti-quarks
4. Decide according to the probability $\boldsymbol{a}$, whether there is a crossing.
   If there is no crossing:
   (a) One baryon consists of the constituent quarks of the proton, *i.e.* it is a proton, the other one of the three sea–quarks.
   (b) **Start the simulation of the next event.**
5. If there is a crossing, randomly choose three quarks to form one baryon, reject the choice as long as it consists only of constituent or only of sea quarks. The three remaining quarks make up the second baryon.
6. **Start the simulation of the next event.**

100000 events were simulated to calculate the ratios, leading typically to more than 1000 particles of each type.
The whole range of a and b was scanned by this method. To find parameters a and b such that the ratios are similar to the results from an experiment, a distance function between the results of the Monte Carlo and the results from the experiment is calculated, namely

$$\text{distance} = \sqrt{\sum_i \left(\frac{m_i - e_i}{m_i}\right)^2}, \tag{2.1}$$

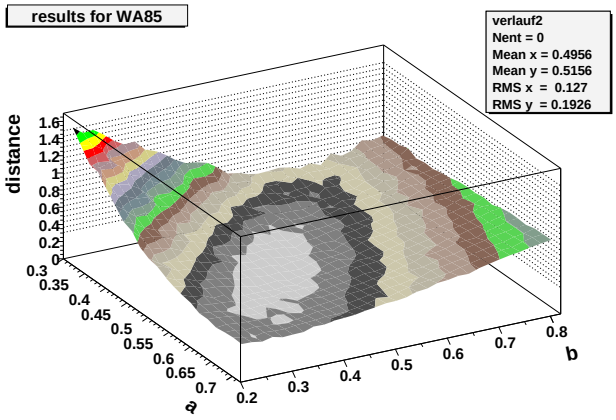

(a)

Figure 2.1: A global minimum in the a–b-plane for the WA85 data is found. Plotted is here the distance function as defined in Formula 2.1.

where the m_i numbers are the ratios obtained by the Monte Carlo, with $m_1 = \frac{\overline{\Lambda}}{\Lambda}$, $m_2 = \frac{\overline{\Xi}}{\Xi}$, etc. And the e_i numbers are the measured ratios from the experiment. This distance function represents the relative euclidian distance. The reason the relative distance was taken instead of the absolute distance is that small values could have large relative deviations otherwise. The euclidian distance was the most simple choice, a weighting with the errors was not considered, since the model is only meant to reproduce the measured values qualitatively.

2.3.3 Alea iacta est: Results

By taking again the results from WA85, a global minimum in the distance function — where the ratio $\frac{\overline{\Xi}}{\Lambda}$ was not used, since it hardly changed with the parameters — was found as seen in Figure 2.1. A descending algorithm did not work out very well due to the flat distribution in the minimum and the statistical character of the Monte Carlo method that never gives exactly the same result for the same parameters. Nevertheless, since the minimum is flat, the best value found ought to be sufficiently close to the true minimum. It is, again with the results of WA85 in parenthesis: $\frac{\overline{\Lambda}}{\Lambda} = 0.18(0.20)$, $\frac{\overline{\Xi}}{\Xi} = 0.60(0.47)$, $\frac{\Xi}{\Lambda} = 0.086(0.070)$ and $\frac{\overline{\Xi}}{\overline{\Lambda}} = 0.30(0.16)$, with $a = 0.447$ and $b = 0.536$. Obviously the Monte Carlo method performs much better than the calculation by hand. Interestingly enough, a is not much smaller than 0.5, unlike in the calculation by hand where $a = 4.35 \cdot 10^{-4}$, which explains why the manual calculations failed. This would mean, that the probability to pair a sea–anti-quark with a constituent–quark is almost equal to a pairing with a sea-quark. The same seems to hold for the probability b to form a baryon–anti-baryon pair, rather than three mesons.

Chapter 3

The HERA-B Experiment

The HERA-B experiment is one of four experiments at the HERA storage ring at DESY in Hamburg, Germany. In this chapter the design of the experiment will be described briefly, concentrating on the parts that are important for the analysis carried out in this thesis.

3.1 Physics Goals

The HERA-B experiment was built to measure CP-violation in the B_d-meson systems. As seen in the unitary triangle in figure 1.4, each angle can be measured by one or more appropriately chosen decays. For the angle β it's the so called "golden B^0decay": $B^o(\overline{B}^o) \rightarrow J/\psi K_s^0$. This decay mode is called "golden", since it has some theoretical as well as experimental advantages. This decay mode is dominated by a tree diagram (not including loops), which can be calculated easily. Experimentally the signatures of such a decay are easy to trigger on [Pet02].
With $n(t)$ being the decay rate of $B^o \rightarrow J/\psi K_s^0$ and $\bar{n}(t)$ that of $\overline{B}^o \rightarrow$

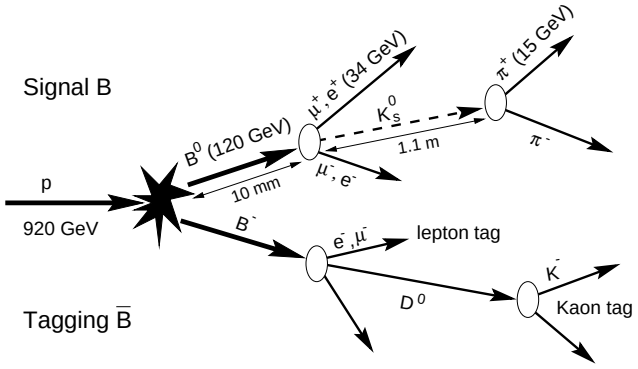

Figure 3.1: The gold-plated decay $B^0 \rightarrow J/\psi K_S^0$. The charge of the b-quark is found by the lepton or kaon tag. Taken from [Pet02].

$J/\psi K_s^0$, the so called CP-asymmetry becomes [HB94]:

$$A_{CP}(t) = \frac{n(t) - \bar{n}(t)}{n(t) + \bar{n}(t)} = \sin 2\beta \sin xt \tag{3.1}$$

The last equality is true in the Standard Model with the angle β from the unitary triangle. The variable x denotes here the mixing parameter, defined by $x = \frac{\Delta M}{\Gamma}$ where ΔM is the mass difference of the two B^0 mass eigenstates and Γ is their mass width.
To measure A_{CP} it must be known whether a B^0 or a $\overline{B}^0$ decayed. How to do this "tagging" by analyzing the decay products of the other B-meson is shown in Figure 3.1.
Unfortunately, due to technical problems, $\sin 2\beta$ could not be measured in the year 2000 running period. Since then, the precision of BaBar and Belle is such that HERA-B is no longer competitive [HB00].

3.2 The HERA Storage Ring at DESY

The "**H**adron **E**lektron **R**ing **A**nlage" HERA is a double storage ring for protons and electrons (or positrons) at the "**D**eutsches **E**lektronen **SY**nchrotron" DESY (see Fig. 3.2). It has a circumference of 6.3 km, the electrons (positrons) have an energy of 27.5 GeV and the protons have an energy of 920 GeV [DES01]. This yields about 42 GeV in the proton-nucleon center of mass system of a fixed target experiment and about 320 GeV in the proton-electron center of mass system.

There are four experiments at the storage ring: ZEUS and H1, which are collider experiments to examine the structure of the proton, Hermes, which is a fixed target experiment using only the electron beam to examine the spin structure of the nucleon, and HERA-B which is also a fixed target experiment but using the protons.
The proton beam is divided into 220 possible stable bunches of which only 180 are filled. The length of one bunch is about 1 ns, with 96 ns between two bunches.

3.3 The HERA-B Detector

The HERA-B detector is a single-arm forward-angle spectrometer, divided into various sub-detectors (see Fig.3.3). As seen in the figure, the angular region covered by the spectrometer is between 10 and 220 mrad in x-direction and 10 to 160 mrad in y-direction, corresponding to a coverage of about 90% of the solid angle in the rest frame of the proto–nucleon system [HB95]. Here, as throughout this thesis, y points upwards and x inwards in respect to the HERA ring. The proton beam points along the positive z-direction.

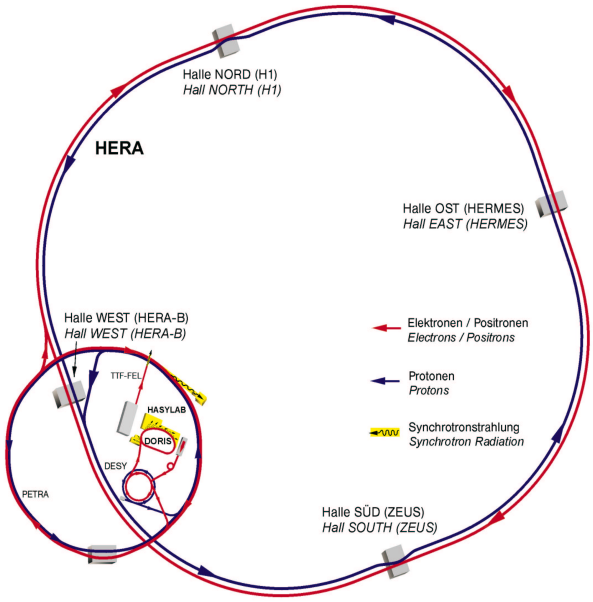

Figure 3.2: The HERA storage ring at DESY [DES01].

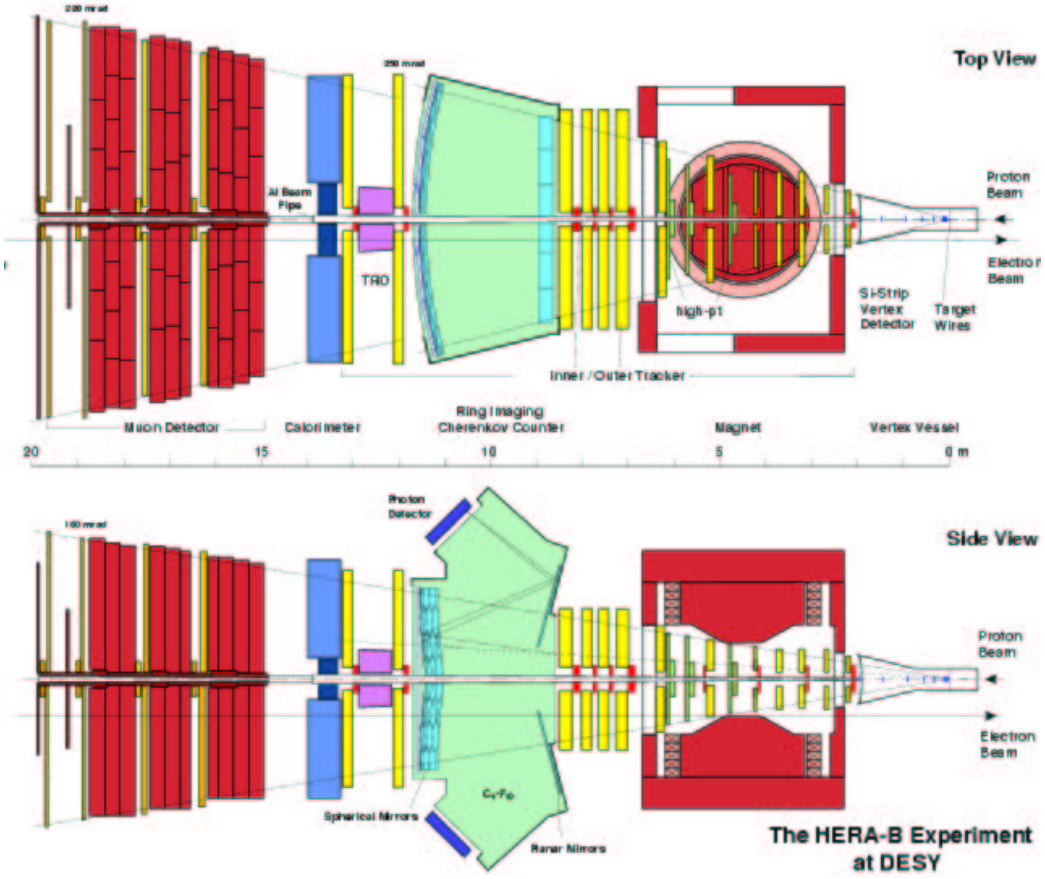

Figure 3.3: Layout of the HERA-B detector[Pyr02].

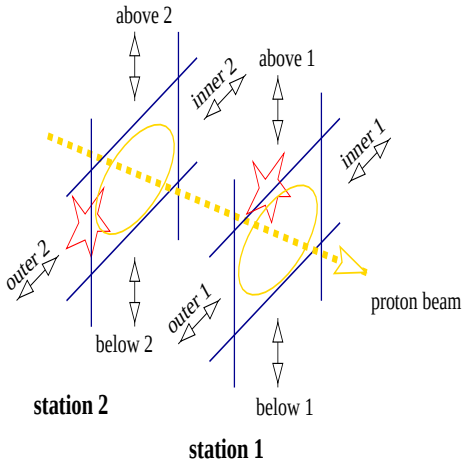

Figure 3.4: Schematic view of the target, taken from [HB00].

3.3.1 The Target

The target consists of eight wires at two stations, separated from each other by 40 mm (see Fig. 3.4). The wires are in beam direction 500 μm thick and are 50 μm wide. They can be moved in and out to adjust and stabilize the interaction rate. The distance of a wire to the beam center is about four to six standard deviations of the beam [Fun99]. The beam has a roughly Gaussian shape, with a typical width of 400 μm. Various target materials can be used.

3.3.2 Vertexing and Tracking System

Since only the vertexing and tracking was used for the analysis in this thesis, these parts will be described in greater detail. This system consists of the **V**ertex **D**etector **S**ystem (VDS), the magnet and the main tracker, *i.e.* inner tracker combined with outer tracker. In the VDS, situated directly behind the target, primary and secondary vertices of charged tracks are detected. The main tracker records tracks of charged particles downstream of the magnet. By fitting track segments of the VDS with those of the main tracker the momentum of the particle can be calculated, assuming they are singly charged.

The Vertex Detector System

The VDS consists of 64 (mostly double sided) silicon strip detectors. They have an active surface of 70 x 50 mm^2 each. Groups of eight of them form a so called super-layer, such that there are two detectors each, above, below, right and left of the beam. On the detectors the silicon strips are parallel to each other on each plane, but slanted with respect to the other planes, such that four track projections are measured with stereo angles of $\pm 2.5°$ and

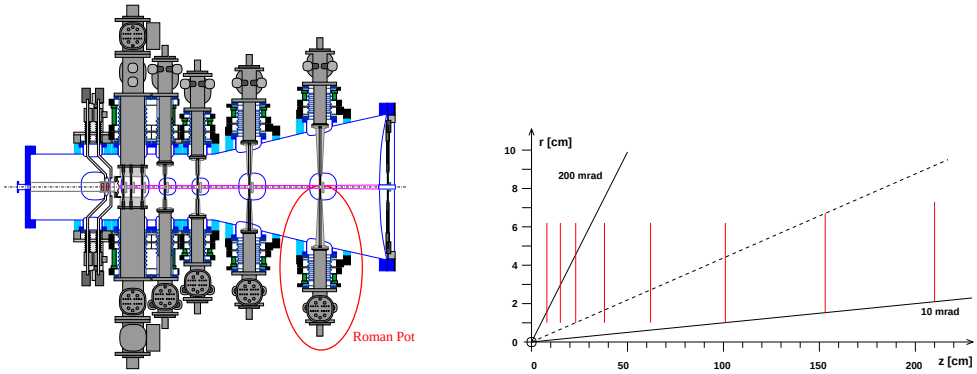

(a) (b)

Figure 3.5: The Vertex detector system: the detector modules mounted on roman pots located inside a vacuum vessel (a) and the angular acceptance of the VDS (from [Brä01])(b).

90°±2.5°. This allows to reduce ambiguities when more than one particle passes a super-layer. The angular acceptance is, requiring at least three super-layers to be passed, between 10 and 250 mrad [Brä01](see Fig. 3.5). In the year 2000, a vertex resolution, measured with J/ψ decays into two muons, of 40 μm in transverse and 630 μm in the longitudinal direction [Bau03] was achieved for the VDS. The performance of the VDS in 2002 was, as in 2000 [Bau03], good and the design specifications were met.

The Magnet

As stated above, the momentum ($\frac{Q}{p}$ to be exact) of a track can be calculated by its curvature in the magnet between the VDS and the main tracker. The dipole magnet has a field integral of 2.2 Tm. The particle trajectories are bent in the xz-plane.

The Inner Tracker

The **I**nner **Tr**acker (ITR) covers a region between 10 mrad and 100 mrad, corresponding to distances of 6 cm to about 30 cm to the beam. The particle densities that were expected when HERA-B was planned were too large for wire chambers. Thus a new technology was needed, and for the ITR the **M**icro **S**trip **G**aseous **C**hamber (MSGC) were chosen. An MSGC works like a multi wire proportional chamber with gas amplification where the wires are replaced by strip electrodes on a substrate (see Fig. 3.6)[Eis99]. Its resolution is better than 0.1 mm in x-direction and 1 mm in y-direction. As counting gas a mixture of Ar/CO_2 (70:30) was used.
Due to problems with gas discharges in hadron beams, the voltage at the elec-

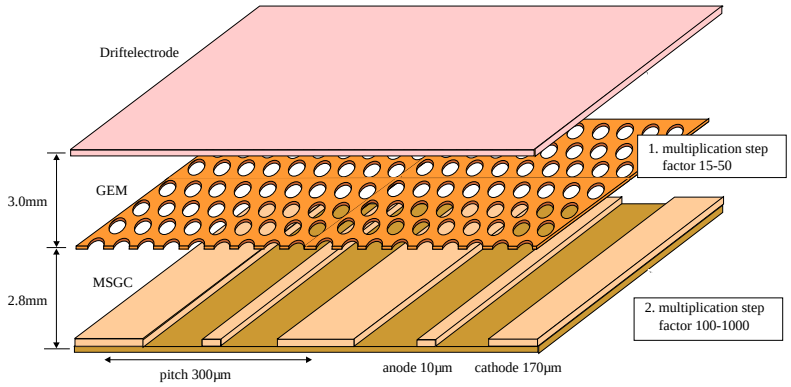

Figure 3.6: The Inner Tracker, schematic view of a MSGC/GEM-Module.

trodes had to be reduced. To achieve the required amplification, a GEM(**G**as **E**lectron **M**ultiplyer)-foil was added as a preamplifier. The GEM holds a voltage of 440V.
The whole detector consists of 48 layers of four rectangular MSGCs. Each MSGC has dimensions of 25x25 cm^2. The Layers are grouped in super-modules of three layers. The layers of one super-module are rotated about the y-axis by $-5°$, $0°$ and $+5°$ to have a stereo angle [Gra01].
In the runs used in this analysis, the ITR was still in the commissioning phase and therefore was not used in the reconstruction of the data.

The Outer Tracker

The **O**uter **Tr**acker (OTR) [Zim99] is split into one super-layer right in front of the Magnet (the Magnet Chamber, MC1), 4 Super-layers between Magnet and RICH (called Pattern Chambers, PC1-4) and the two so called trigger chambers, that are used by the first level Trigger, between RICH and ECAL (TC1-2) (see Fig. 3.7, MC2-8 have been removed during the shut down in 2001). The analysis is based on the information from the PCs and MCs. The outer tracker chambers have z-positions between z=210 cm and z=1320 cm and a radial distance to the beam of about 20cm. The angular coverage is up to 250 mrad in the bending plane (x) and 160 mrad in the non-bending plane (y). Every super-layer, similar to the ITR, has three layers with stereo angles of 0 and $\pm 5°$.
These layers consist of so called honeycomb drift chambers in single or double layers (see Fig. 3.8(a)). The counting gas used is a mixture of Ar, CF_4 and CO_2. There are chambers of 5 and of 10 mm size (see Fig. 3.8(b)). Because of the larger track density, the 5 mm ones are closer to the beam. In 2000, the 5 mm chambers reached a spatial resolution of 240-300 μm ([HB00]). In 2002 the OTR was running smoothly.

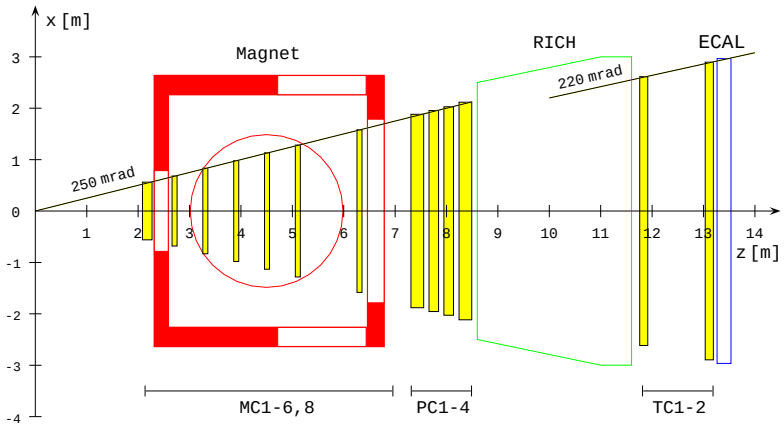

Figure 3.7: Overview of the outer tracker (OTR) [Zim99]. MC2-8 have been removed in 2001.

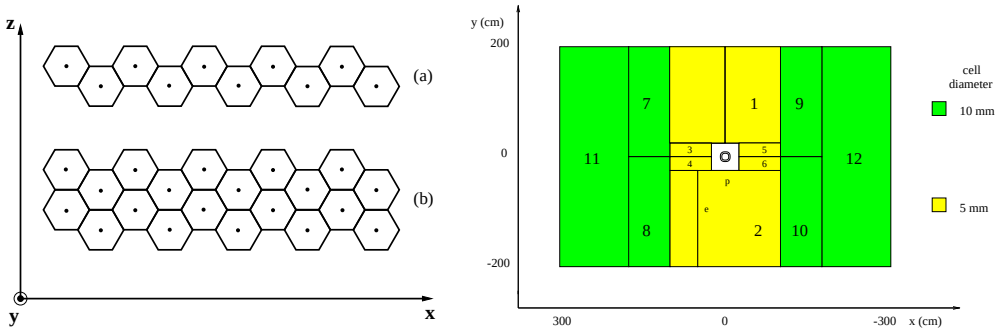

(a) (b)

Figure 3.8: The outer tracker: (a) single and double layer honeycomb structure [Zim99] (b) segmentation

3.3.3 RICH, ECAL and Muon Chambers

The other sub detectors are not used for this analysis and thus described only briefly.

The Ring Imaging Čerenkov Detector (RICH) [Ari00] uses the Čerenkov effect to determine the velocity of a particle. The HERA-B RICH uses a radiator gas, in which the Čerenkov-light is guided by mirrors to arrays of photomultipliers. The Čerenkov-light is emitted in a cone of the opening angle ϑ_C which is mapped onto a ring at the photomultiplier array. Using the relation $\cos\vartheta_C = \frac{1}{\beta n}$, where n is the refractive index of the medium, $\beta = \frac{v}{c}$, the velocity in natural units, is measured. Knowing the velocity and the momentum (using the tracking system) of a particle, the mass can be calculated, and thus the particle identified.
The HERA-B RICH can separate particles roughly in a range of 10 - 50 GeV [HB00].

The Electromagnetic Calorimeter (ECAL) [Zoc00] can measure the position and energy of electrons, positrons and photons by their electromagnetic shower. It consists of layers of matter of absorbers (out of tungsten and lead) and, alternating, scintillators connected to photomultipliers. The ECAL also plays an important role in the trigger system (see Section 3.3.4).

The Muon Chambers [Tit00] consist of gas proportional chambers. In front of and between the four muon chamber layers, there is located about 1 m of absorption material, which practically only muons can penetrate.

3.3.4 Trigger and Data Acquisition

HERA has a bunch crossing frequency of about 10 MHz. This is way too fast to process and store all the data that are produced. On the other hand most of the interactions are inelastic scattering involving light and strange quarks only. For a study of CP-violation in the B-meson system, these events have to be suppressed. To solve this problem a three stage trigger system has been designed (as reference see *e.g.* [HB94] and [Kre01]).

The Pretrigger

The **F**irst **L**evel **T**rigger (FLT) is initiated by the so called *Pretrigger* if there is either a transverse energy[1] deposit in a region of the ECAL above some threshold (indicating an electron, positron or possibly a photon), or if there are coincident signals in the muon chambers MC3 and MC4, pointing back to

[1] The transverse energy is $E_t = E \cdot \sin\theta$. It is approximated here by a rough estimate of the p_t kick of the particle by the magnet of 600 MeV and the bending of the particle track by the magnet [Kre01].

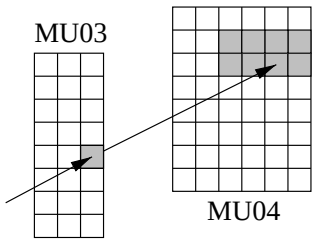

Figure 3.9: Coincidence Patterns (Regions of Interest (RoI)) in the μ-pretrigger

the target, consistent with a muon. The way a muon candidate is recognized is the following: for each hit in one layer a search is done in a **R**egion **o**f **I**ntrest (RoI) in the next layer for a coincident hit. This is depicted in Figure 3.9. These modes of operation allow to trigger on di-electrons or di-muons from a decaying J/ψ, produced by the so called golden decay (see Section 3.1).

The First Level Trigger (FLT)

Using the pretrigger information, the First Level Trigger is used to find hits in corresponding RoIs of upstream tracking chambers. Those are TC1 and TC2 for the muon trigger and PC1 and PC4 for the electron triggers (see Fig. 3.10). The FLT does not use the drift time information of the drift chambers.
The track finding (using the RoI technique) is carried out by a network of custom-made processors called **T**rack **F**inding **U**nits (TFU). At the end their information is fed to the **T**rack **P**arameter **U**nits (TPU), where the momentum is calculated, assuming the track is originating in the target. The last part of this information processing chain is the **T**rigger **D**ecision **U**nit (TDU) (see Fig. 3.10). It calculates the invariant mass of all pairs of particles in the bunch crossing and, if it decides to trigger, processes the data to the **S**econd **L**evel **B**uffer (SLB).

The Second Level Trigger (SLT)

The **S**econd **L**evel **T**rigger (SLT) is implemented as a network of 240 PCs connected to the SLB by a network of **D**igital **S**ignal **P**rocessors (DSP). The DSP-network provides a fast connection with a large bandwidth. The SLT uses more tracking chambers, the drift times and the VDS. Using a simplified Kalman Filter approach, see *e.g.* [Frü00], for tracking, this leads to better spatial resolution and less ghost tracks, *i.e.* tracks made out of hits produced by different particles. At last the vertexing is done.

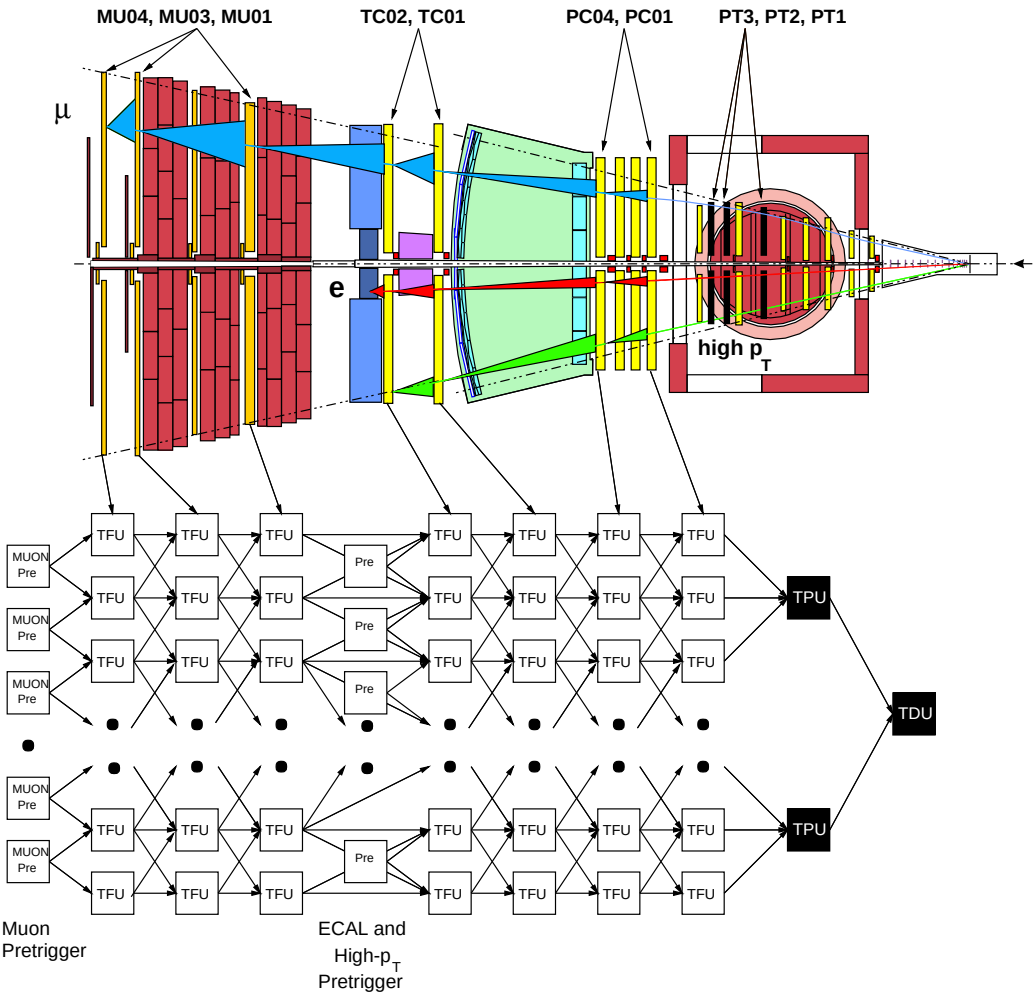

Figure 3.10: The first level trigger: How the information from the pretrigger is processed, using RoIs.

The *Third Level Trigger*, realized on the same PC farm, does a complete event building, *i.e.* all detector information is read into the computers.

The Fourth Level Trigger (4LT)

The **4**th **L**evel **T**rigger (4LT) consists again of a PC farm of 200 Computers, connected to the SLT by an ethernet connection. The 4LT makes a full reconstruction and logs the data on tape. A full scheme of the triggers and **D**ata **Acq**uisition (DAQ) is shown in Fig. 3.11.

The Minimum Bias Trigger

There is the possibility to use two kinds of minimum bias triggers, *i.e.* they accept any kind of event, in the ideal case without any bias. One is a pure random trigger, triggering randomly with a predefined rate on every bunch-crossing. This leads to many empty events in the data. The advantage of the interaction trigger is, that it rejects these empty events. It triggers on a threshold in the RICH and/or ECAL and/or VDS hit multiplicity. The runs used in the analysis of this thesis were taken using an interaction trigger with a threshold of 20 hits in the RICH [Sch02a]. No further triggering stage is needed for a minimum bias trigger. The data can directly be written to tape or sent to the 4LT, which was the case for the data used here.

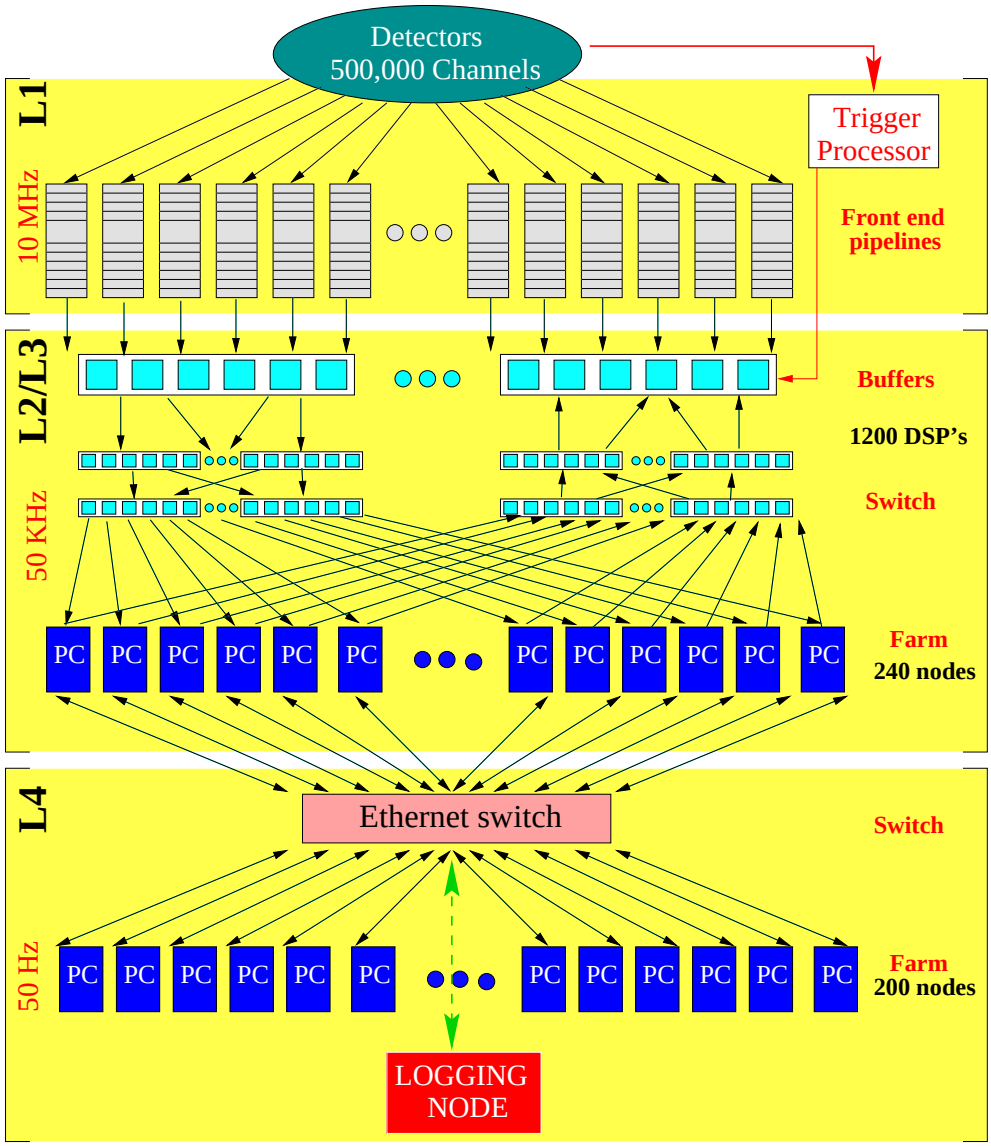

Figure 3.11: The data acquisition system with all the trigger levels [Kre01].

Chapter 4

Extraction of the Hyperon Signals

In this chapter the processing of the raw data is described and how tracking and vertexing information are extracted. The further steps include an event selection and writing the information retained to a file in the compact "BEE" format. Eventually, after a description of the selection criteria for the candidates, the cuts are presented and motivated to extract the Λ, $\overline{\Lambda}$, Ξ^-, $\overline{\Xi^-}$, Ω^- and $\overline{\Omega^-}$ signals. The obtained mass peaks of the hyperons are shown.

4.1 From raw Data to Tracks and Vertices

4.1.1 Runs used

Two interaction trigger runs of the year 2002 were used, one with about 7 million interactions using a carbon target and one with about 2.4 million interactions with a tungsten target. The runs will be referenced by the terms 'carbon run' or 'C-run' and 'tungsten run' or 'W-run'. More detailed information is given in Table 4.1. The second reprocessing (see below) of these runs was used.

run number	number of i.a.	target material	target wire	i.a. rate [MHz]	date
19170	7000215	C	below 1	0.99	20. Jul.
19179	2417098	W	inner 1	0.82	21. Jul.

Table 4.1: Details of the interaction trigger runs of the year 2002 used in this thesis, i.a. is short for interaction. Target wire naming convention is as seen in Fig. 3.4.

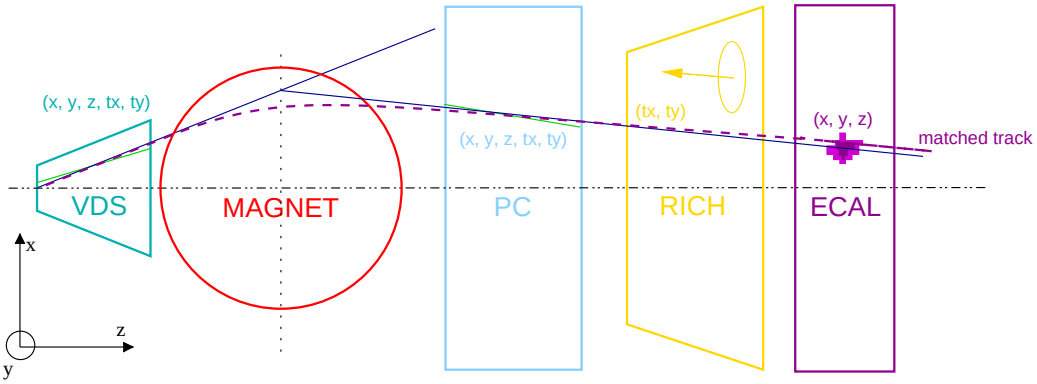

Figure 4.1: The matching of the track segments into tracks. VDS and Pattern Chamber (PC) track segments are extrapolated to the middle of the magnet at $z = 4.55$ m and cuts on Δx, Δy and Δt_x (the slope in x-direction) are applied. The figure is taken from [Aga01].

4.1.2 Reconstruction of the Data with the ARTE Software Package

The reconstruction of the data – meaning finding tracks, vertices, ECAL clusters etc. – usually takes place at least two times, first online while data taking and a second time offline (also called "reprocessing") when the alignment and other calibration constants are known better. The analysis software is called ARTE -**A**nalysis and **R**econstruction **T**ool [ART03]. ARTE stores the information in data structures called tables. Some important tables are *e.g.* RTRA (reconstructed tracks), RSEG (reconstructed track segments) or HITB (detector hits). These tables contain also references to each other, *e.g.* to indicate which track comes from which vertex. ARTE writes so called "dst", short for **d**ata **s**umary **t**ape, files, containing the hit information plus the reconstructed data. A file in the "mini" format, containing only reconstructed data and thus being much smaller, is also written. For the analysis in this thesis, only the mini files were used.

Tracking

After the hits in the sub-detectors have been prepared by the corresponding sub-detector software, the track- and vertex finding takes place. First, the track segments in the VDS and the trackers, the ECAL clusters and the RICH rings, have to be reconstructed. Especially the tracking, which is essential for this analysis, is not a trivial task due to the high multiplicity. CATS, which stands for **C**elular **A**utomaton for **T**racking in **S**ilicon, is the track finding algorithm of the VDS. As the name suggests, it is based on a cellular automaton [Kis99]. There is also a corresponding OTR CATS [Eme01b] for track finding in the OTR, which uses in addition a Kalman Filter to build the

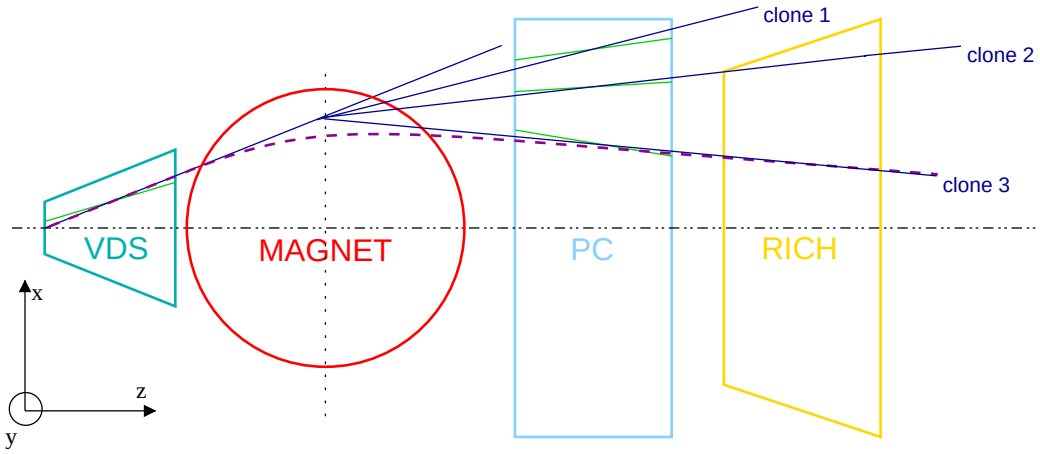

Figure 4.2: When two main tracker segments are matched to the same VDS segment, two tracks sharing the same VDS segment are produced. Such tracks are called clones. The figure is taken from [Aga01].

tracks. The resulting track segments are stored in the RSEG ARTE table. The job to match the track segments, ECAL clusters and RICH rings to a track is done by the software package MARPLE [Igo98]. The most important task is to match the VDS segments to the main tracker segments since the trajectory of the particle bends in the magnetic field in between. Therefore, the segments in both detectors are extrapolated to the center plane of the magnet at $z = 4.55$ m. Then cuts on the distances Δx, Δy, and Δt_x (slope in x-direction) are applied. In Figure 4.1 this is displayed graphically. The final list of tracks are stored in the ARTE table RTRA.
As shown in Figure 4.2, a match can be ambiguous, when *e.g.* two main tracker segments are matched to the same VDS segment giving rise to two tracks sharing at least one segment. Such tracks are called clones. In order to select the track with the best quality from a set of clones, a software routine called `Cloneremove` [Ple01] was developed. First, only reconstructed charged tracks containing a VDS segment are accepted. Then the tracks are selected according to a so called figure of merit (FoM) that is a measure for the quality of the track. The FoM uses the number of hits in the VDS, main tracker and RICH, and the χ^2 per degree of freedom of the track.

Vertexing

The vertexing software used by ARTE is called GROVER [Abt03]. The primary vertices are found by clustering at least three tracks to a vertex candidate where the tracks have to lie within 3.5 standard deviations of a target wire measured in the xy-plane of the wire. Only information of the track segments found in the VDS are used here. These candidates are then fitted using a Kalman Filter approach. In this last step tracks can be excluded

from a vertex if the track has a low probability to belong to the vertex. To ensure that the wire position is correct, a wire following mechanism is used.

4.2 The BEE Analysis Tool

BEE [Gle01a] [Gle01b] is an object oriented analysis tool for high level analysis that has some advantages with respect to ARTE, if only reconstructed data of the events like tracks, vertices, but not hit information are used. Due to a further reduction of the information and data compression, files in the BEE format are smaller than mini files. Technically BEE files are a special kind of ROOT [CER03] files. Thus they can be read using ROOT. Since the data volume is reduced with respect to mini files, analyses with BEE are faster. Another advantage is the SMatrix/SVertex [Gle01c] package based on the Vt++ [Gle00] Kalman filter based vertexing software. SMatrix/SVertex is using template meta programming techniques and is thus 3 to 20 times faster than Vt++ itself [Gle01c].

4.2.1 The Event Selection

While processing the mini file and writing of the BEE file for which the program `SlTableFill` by Thorsten Glebe [Gle02] was taken as a basis, an event selection based on the standard routine `anl_eventselect` by Michael Schmelling [Sch02b] was used. The event selection rejects empty and bad events. This is done by requiring:

- a primary vertex candidate near the target wire (independent of Grover)
- at least three tracks in the VDS
- the event to be synchronous to a filled bunch
- OTR drift times that correspond to a nominal bunch crossing.

In addition, to ensure a good quality of the tracks, a track selection was done:

- Only tracks selected by Cloneremove are used.
- Each track has to point back to an acceptance window around the target wire.
- Each track has to have at least 6 VDS hits and 5 main tracker hits[1].

[1] In order to have the possibility to handle tracks with VDS hits only, as the Ξ^- and Ω^- tracks themselves, the cut on the main tracker hits was done later in the selection of the candidates.

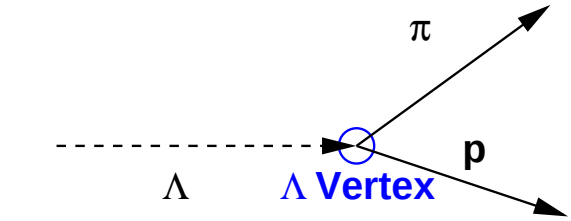

(a)

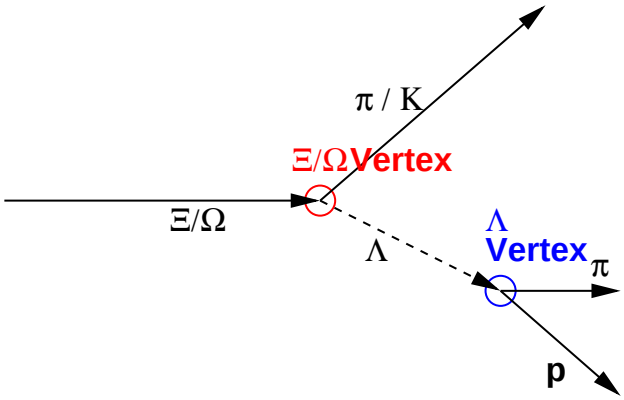

(b)

Figure 4.3: The typical topology of Λ (a), Ξ and Ω (b) decays.

A vertex selection was applied that keeps only primary vertices with a z-position close to the target. Secondary vertices found by GROVER were not used.
After the event selection, in the carbon run about 4.5 million events are left, while in the tungsten run about 1.6 million events remain. Most rejected events had a wrong bunch crossing or no primary vertex candidate was found by the event selection.

4.3 The Preliminary Selection of Candidates

In the next step candidates for the hyperons were selected. The signatures to separate them from the background were topologies of the kind shown in Figure 4.3, corresponding to the decays

- $\Lambda \rightarrow \pi^- + p$
- $\Xi^- \rightarrow \Lambda + \pi^-$
- $\Omega^- \rightarrow \Lambda + K^-$

particle	mass [MeV]	$c\tau$ [cm]	most prominent decay	BR of this decay
Λ	1115.683 ± 0.006	7.89	$\Lambda \to \pi^- + p$	63.9 ± 0.5
Ξ^-	1321.31 ± 0.13	4.91	$\Xi^- \to \Lambda + \pi^-$	99.887 ± 0.035
Ω^-	1672.45 ± 0.29	2.46	$\Omega^- \to \Lambda + K^-$	67.8 ± 0.7

Table 4.2: In this table, the most important properties of Λ, Ξ and Ω hyperons for this analysis are listed as given in [Hag02]. BR means **B**ranching **R**atio, $c\tau$ is the velocity of light times the lifetime of the particle in its rest frame.

and the analogous decays of the anti-particles. The Λ hyperons from the Ξ^- and Ω^- decays are again recognized by the decay $\Lambda \to \pi^- + p$. The symbols Ξ and Ω always mean Ξ^- and Ω^- throughout this thesis, except where it is stated differently or it is obvious. In Table 4.2 the most important properties for this analysis of the Λ, Ξ and Ω hyperons are shown.

4.3.1 Selecting Λ Candidates

To select Λ candidates[2] according to the topology 4.3(a), each event is searched for two oppositely charged tracks, the $(\pi^+)\pi^-$ and the (anti-)proton track. These two tracks are fitted using the SVertex software to a vertex, further on called Λ vertex. Starting with the hypothesis that the particle with larger momentum is the proton or anti-proton[3] and the other one is a pion and assigning the corresponding masses, the invariant mass is calculated. If it is within a predefined range (here 1.09 GeV $< m <$ 1.14 GeV), the vertex is kept, otherwise the other possible mass hypothesis where the particle with the smaller momentum has the proton mass, is checked.
Another requirement is that the Λ vertex is downstream of the target. A cut to reject candidates with a large root mean square distance of the tracks to the Λ vertex d_{RMS} is set. And finally a cut to reject candidates with a large impact parameter, *i.e.* the distance of the extrapolated Λ track to the primary vertex (as shown in Fig. 4.4), is applied. The primary vertex was required to have at least two tracks. The Λ track is determined from the sum of the momenta of the two charged tracks and the vertex position. The selected candidates are stored in a ROOT n-tuple file.

[2] based on the routine `rcSelect_K0S_Lambda` by Federico Sanchez [San02]

[3] The (anti-)proton gets a larger longitudinal momentum in the rest frame. See *e.g.* [Ple02].

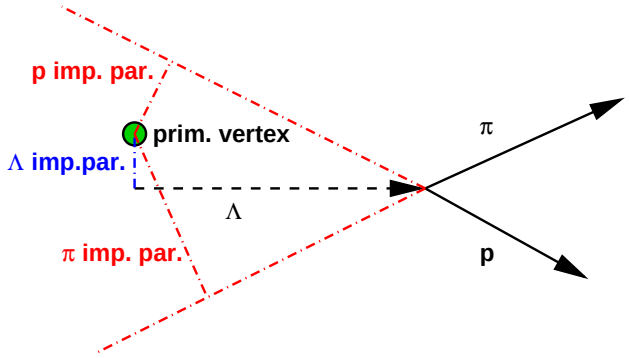

Figure 4.4: A graphical description of the π, proton and Λ impact parameters.

4.3.2 Selecting Ξ and Ω Candidates

The selection of Ξ and Ω candidates is done independently from each other but with exactly the same method, so it is described here once for both particle types. The cascade's topology that is searched is shown in 4.3(b). First a vertex fit of each Λ candidate, not applying the impact parameter cut, in the mass region 1.109 GeV $< m <$ 1.123 GeV (corresponding to the $3\sigma_{Gauss}$ region of the Λ mass peak, see Fig. 4.10), with each other charged track is done. The resulting vertex shall be called Ξ/Ω vertex. As mass hypothesis, the mass of a charged pion (for the Ξ candidates) or of a charged kaon (for the Ω candidates) is assigned to the additional track. This new vertex is preselected, if its invariant mass is in the range 1.25 GeV $< m <$ 1.45 GeV for Ξ or 1.5 GeV $< m <$ 2 GeV for the Ω selection. From all preselected candidates belonging to one Λ candidate, the one is chosen for which the tracks have the lowest root mean square distance to the Ξ/Ω vertex.

4.4 The used Cuts

From these candidates, the mass peak signals are obtained by applying the following cuts.

4.4.1 The Λ Cuts

Looking at the topology of the decay in Figure 4.3(a), one can motivate some of the cuts. First the Λ must originate from the primary vertex and thus have a small impact parameter, *i.e.* the distance to the primary vertex as seen in Figure 4.4. The cut value was chosen to be 0.06 cm, about 15 times the VDS vertex resolution in the xy-plane (see Section 3.3.2). Then the vertex has to have a good quality, which is guaranteed by a cut on the root mean square distance of tracks to the vertex d_{RMS}, where the point of closest approach defines the vertex position. This cut was set to 0.04 cm, about 10 times the VDS vertex resolution in the xy-plane (see Section 3.3.2). A cut on the flight

length in the Λ rest frame βct_0, where t_0 is the decay time in the rest frame of the Λ, was applied. This rejects background of track combinations from the main vertex. Since all the particles are relativistic, one has $\beta ct_0 \approx ct_0$. Thus the cut value of 0.13 cm is much smaller than $c\tau = 7.89$ cm [Hag02] of the Λ, so only about 1.6% of the true Λ hyperons are rejected.
The K_s^0 also decays into two oppositely charged particles, namely π^- and π^+. It has a $c\tau = 2.68$ cm [Hag02] in the same order of magnitude as the Λ and can be even kinematically indistinguishable from it [Ple02]. Assigning the pion mass to the two charged tracks, the Λ candidate is rejected if it falls into a mass window around the K_s^0 mass.
To reduce the background further, a cut on the sum of the impact parameters of the two decay products (pion and proton) of the Λ $b_\pi + b_p$ is applied (see Figure 4.4 for illustration). This cut mainly rejects background from photon conversion which has a small angle between the tracks and will be examined more closely below.
To summarize, here is a complete list of the Λ cuts:

- For the Λ vertex: $d_{RMS} < 0.04$ cm
- Impact parameter of the $\Lambda < 0.06$ cm
- Λ flight length boosted to its rest frame > 0.13 cm
- Sum of the impact parameters of the decay products $b_\pi + b_p > 0.35$ cm
- remove all Λ candidates that fulfill a K_s^0 mass-hypothesis (0.485 GeV $< m <$ 0.515 GeV)

The values of the cuts were established by a procedure that will be described here for the case of the cut on the sum of the impact parameters of the decay products, $b_\pi + b_p$.

The Cut on the Sum of the Impact Parameters of the Decay Products

For a given mass peak to which a Gaussian can be fitted, a peak and a sideband region can be defined. Here the peak region was chosen to be the 3σ region around the mean, where σ is the standard deviation of the Gauss function of the fit and the 3σ region means the region three standard deviations to the left and three to the right of the center c of the Gauss fit, $[c - 3\sigma, c + 3\sigma]$. The intervals $[c - 6\sigma, c - 3\sigma]$ and $[c + 3\sigma, c + 6\sigma]$ were defined to be the sideband region. The borders of those are also shown in figure 4.5. In Figure 4.6 the variable under consideration, $b_\pi + b_p$, is plotted once for the peak, and once for the sideband region. The point where the peak distribution has significantly more entries than the distribution of the sideband region is the point where the signal starts to behave differently

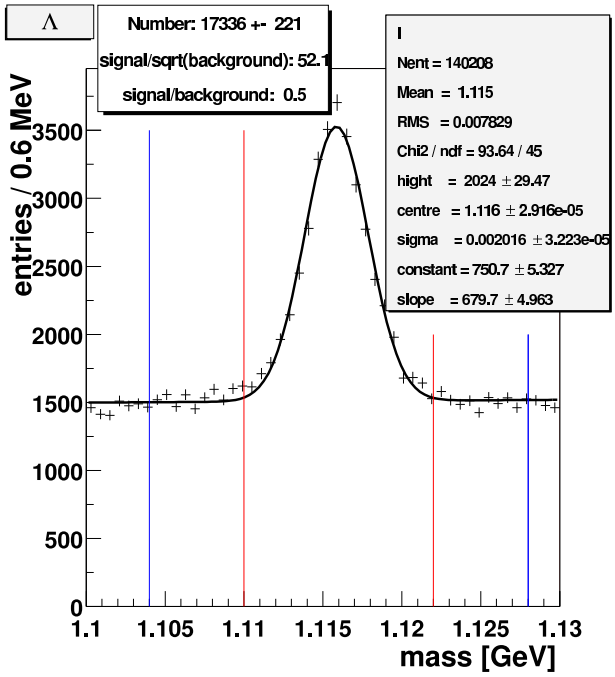

Figure 4.5: The Λ mass peak of the carbon run, all cuts applied, except the $b_\pi + b_p$ cut. Compare this to 4.10(a), the mass peak with all cuts applied. The inner lines indicate the border of the peak or signal region, the outer lines that of the sideband or background region.

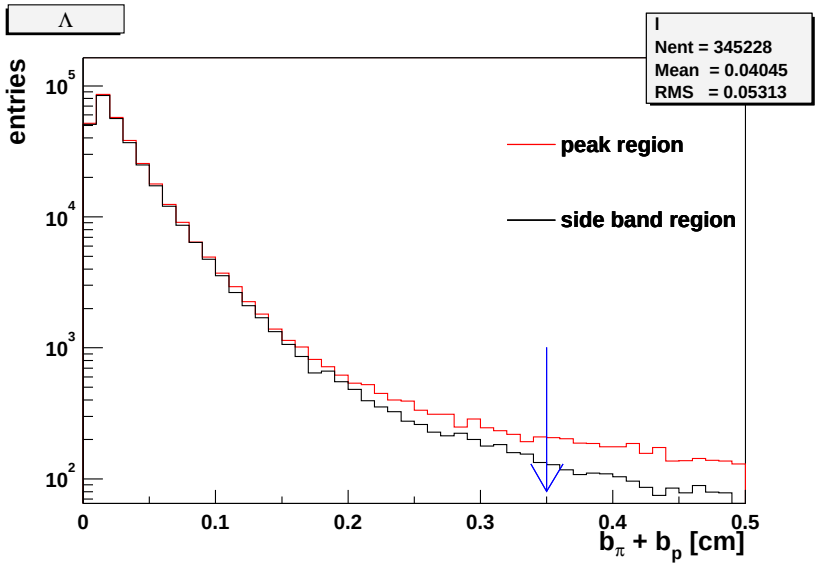

Figure 4.6: The variable $b_\pi + b_p$ plotted for the peak and side band regions (see text). The arrow indicates the cut value. Above this value the peak distribution dominates in this plot.

compared to the background. Thus the value of the variable to cut on should lie in this range, as indicated in Figure 4.6 by the arrow. By comparing Figure 4.5, the signal in the carbon run obtained without the $b_\pi + b_p$ cut with Figure 4.10(a) the signal with the cut, a strong reduction of the background can be observed.

4.4.2 The Ξ Cuts

The cuts for the Ξ selection are based on the cuts for the Λ candidates. The value of the $b_\pi + b_p$ cut is reduced to increase efficiency. For the same reason, the cut on the Λ flight length has been dropped. The d_{RMS} cut for the Ξ vertex is larger than that for the Λ vertex, because it is a vertex of which one track was reconstructed from two other tracks. The only cut that is new, is the cut on the impact parameter of the pion from the Ξ decay. Since the pion is much lighter than the Λ, it has a much larger impact parameter.
Again the values of the cuts have been established by the procedure described above. The complete list of cuts is:

- Use the same cuts as for Λ candidates, except:
  - No cut on the impact parameter of the Λ at the main vertex
  - No cut on the Λ flight length
  - Sum of the impact parameters of the Λ decay products > 0.3 cm
- For the Ξ vertex: $d_{RMS} < 0.1$ cm
- Ξ impact parameter < 0.05 cm
- z-position of Ξ vertex has to lie up stream of the Λ vertex
- Impact parameter of the π from Ξ decay > 0.1 cm

4.4.3 The Ω Cuts

The same procedure for the Ω cuts gives the following values. Additionally a cut on the flight length of the Ω was introduced and the cut on the Ω vertex quality became more rigid. This was done to reduce the high background.

- Use the same cuts as for Ξ candidates, with the pion from the Ξ decay exchanged by the kaon from the Ω decay, except:
  - For the Ω vertex $d_{RMS} < 0.04$ cm
  - No cut on the impact parameter of the kaon alone
- $b_\Lambda + b_K > 0.06$ cm

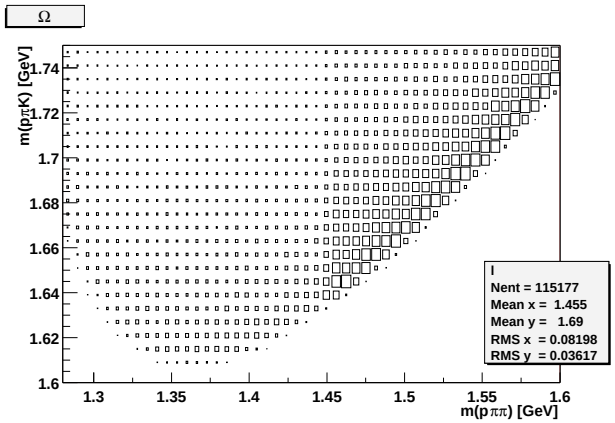

Figure 4.7: Here the invariant mass under Ω mass hypothesis $m(p\pi K)$ is plotted versus the Ξ mass hypothesis $m(p\pi\pi)$ for the Ω candidates in the carbon target run. A strong band is seen starting at about $m(p\pi\pi) = 1.45$ going to higher masses.

- Flight length of the Ω boosted to its rest frame > 0.4 cm
- Only use candidates that fulfill a Ξ mass hypothesis $m(p\pi\pi)$ in the range 1.38 GeV $<$ m $<$ 1.51 GeV.

The cut on the impact parameter of the pion for the Ξ reconstruction is replaced by a cut on the sum of impact parameters of the products of the Ω decay $b_\Lambda + b_K$. In contrast to the case of the Ξ, an analog cut on the impact parameter of the K is less powerful, since the $\frac{K}{\Lambda}$ mass ratio is much larger than the $\frac{\pi}{\Lambda}$ mass ratio.
Of this list one cut is especially interesting and new, that is the cut on the mass of the Ω when applying the Ξ mass hypothesis, *i.e.* the hypothesis that the particle produced together with the Λ is not a kaon, but a pion.

The Cut on Ω candidates with Ξ Mass Hypothesis

This cut has two tasks, one is to eliminate Ξ hyperons that are background for the Ω signal. This is done by requiring the invariant mass to be larger than 1.38 GeV under a Ξ mass hypothesis (compare with Tab. 4.2). The other task is to cut off background in the region above 1.51 GeV applying the Ξ mass hypothesis, as seen in Figure 4.7. In this figure, the invariant mass under Ω mass hypothesis $m(p\pi K)$ is plotted against the Ξ mass hypothesis $m(p\pi\pi)$ for Ω candidates in the carbon run. A strong band can be seen starting at about $m(p\pi\pi) = 1.45$ GeV. This band can be partially eliminated by cutting on the invariant mass under the Ξ mass hypothesis, such that the Ω hyperons are kept.
Thus the question arises how the Ω hyperons behave in the variable $m(p\pi\pi)$. This was evaluated using a simple toy Monte Carlo (see *e.g.* [Cow98] for a

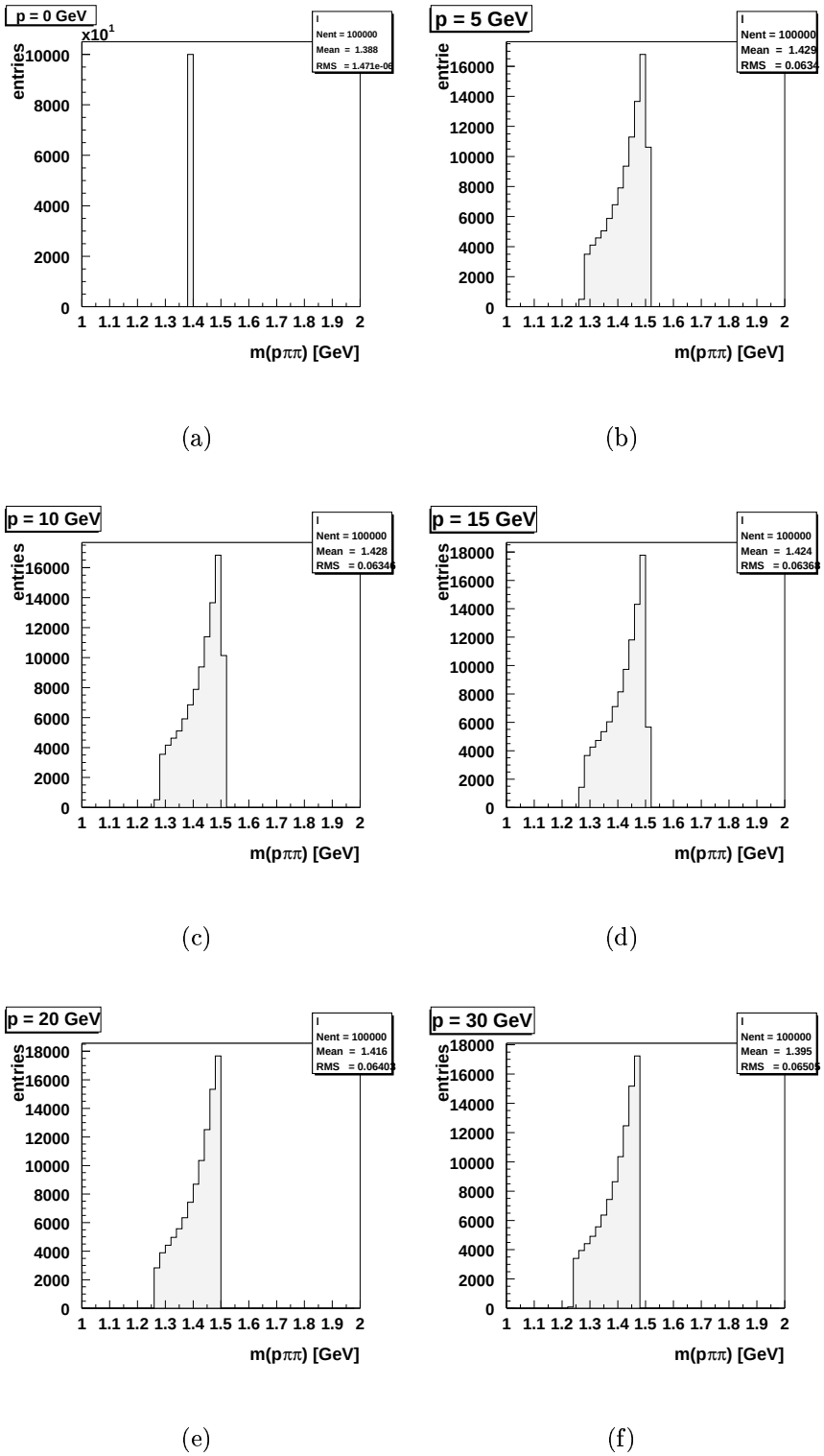

Figure 4.8: The result of the simple toy Monte Carlo simulation of an Ω decay. The invariant mass is plotted under Ξ mass hypothesis $m(p\pi\pi)$ for different momenta p. This helps to establish a value for the $m(p\pi\pi)$ cut.

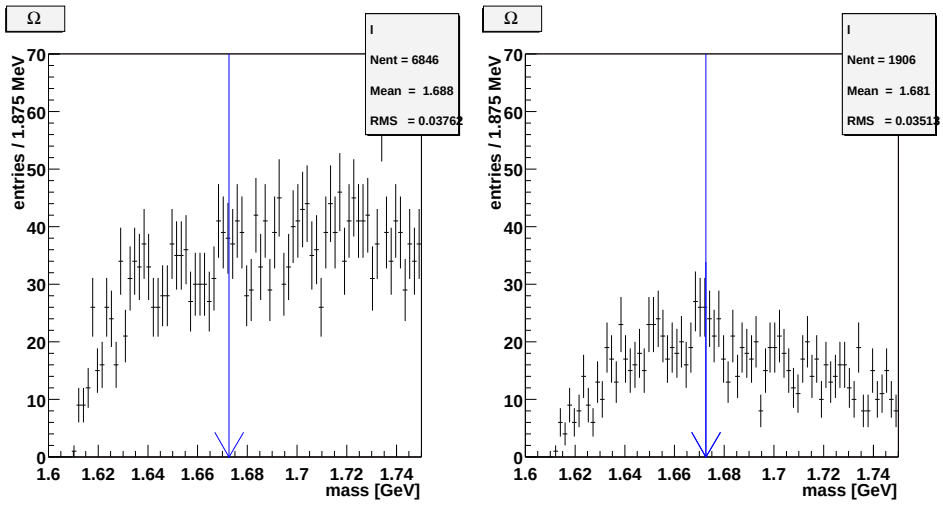

(a) (b)

Figure 4.9: In (a) the invariant mass spectrum of the Ω candidates in the tungsten run after some preselection cuts is shown. In (b) the same spectrum is depicted where the same cuts were applied but in addition the cut on the $m(p\pi\pi)$ mass hypothesis. A change in the shape of the background can be observed.

description of the Monte Carlo method). An isotropic two particle decay of a particle with Ω mass into particles with kaon and Λ mass was simulated. Then the invariant mass under the Ξ mass hypothesis $m(p\pi\pi)$ is plotted. The result can be seen in Figure 4.8 for different values of the Ω momentum. The total momentum of the Ω candidates in the data peaks between 10 GeV and 15 GeV and becomes negligible above 30 GeV. From these plots, two things can be learned: first requiring $m(p\pi\pi) < 1.51$ GeV will not cut away any Ω, second, with the cut on $m(p\pi\pi) > 1.38$ GeV, which is well above the Ξ mass, only about a quarter of the Ω hyperons may get lost, reducing the background efficiently.
Note that cutting on invariant masses or other dynamical variables can be dangerous, since it can create structures or even a peak in the background. Thus the effect of this cut has to be examined. In figure 4.9, the invariant mass spectrum of the Ω candidates in the tungsten run is shown once just applying some soft preselection cuts, omitting the cut on $m(p\pi\pi)$, and the same spectrum with the same cuts but additionally the $m(p\pi\pi)$ cut. It is noticeable that the background indeed changes its shape and *is now, after the cut, elevated around the* Ω *mass*, which is indicated by an arrow. This is not a problem, since the Ω peak itself is expected to be much narrower, but it has to be taken into account for the background subtraction of the signal.

4.5 Obtained Signals

In Figures 4.10, 4.11 and 4.12, the mass spectra of Λ, Ξ, Ω and their anti-particles in both runs are shown. To the Λ and Ξ distributions a Gaussian peak plus linear background was fitted using the χ^2 method (see *e.g.* [Cow98]). The fit results are stated in the histograms. The widths of the $\Lambda/\overline{\Lambda}$ are similar in both runs and about 2.1 MeV. The same holds for the $\Xi/\overline{\Xi}$ distributions where the width is about 2.4 MeV. The particle data group values are indicated in the histograms by the arrow.
The way the numbers of particles were determined in case of Λ and Ξ hyperons is the following. All bins in the 3σ peak region (please refer to Section 4.4.1 for the definition of the 3σ region) minus the corresponding value of the linear part for that bin are added up.
To determine the number of Ω hyperons in each run, first a Gauss function was successfully fitted to the $\overline{\Omega}$ signals as seen in Figures 4.12(b) and 4.12(d). For the Ω signals the fit didn't work out correctly. This determines the 3σ region of the Ω hyperons as $\sigma \approx 4.2$ MeV for the tungsten and $\sigma \approx 3.3$ MeV for the carbon run. Actually the results won't change significantly with these numbers, except for $\overline{\Omega}$ in the carbon run, but the uncertainties are anyway large there. The 3σ region for the carbon run corresponds to about 1.662 GeV – 1.682 GeV. Then the number of entries in the 3σ region was counted in each histogram in Figure 4.12 as well as in the region 1.63 GeV to 1.7 GeV, excluding the peak region, to get the background level. This range around the peak was chosen since the background is supposed to be higher around the peak region as seen in Section 4.4.3. This procedure will be shown here for the example of the $\overline{\Omega}$ hyperons in the carbon run (Fig. 4.12(b)).
The number of entries in the 3σ region mentioned above is counted to be $8 \pm \sqrt{8}$. The number of background entries is $7 \pm \sqrt{7}$, and then scaled to the signal region, giving 2.8 ± 1.1 entries. Thus the number of $\overline{\Omega}$ after the cuts in the carbon run is

$$(8 \pm 2.8) - (2.8 \pm 1.1) = 5 \pm \sqrt{2.8^2 + 1.1^2} = 5 \pm 3.$$

All results after the cuts are collected in Table 4.3.

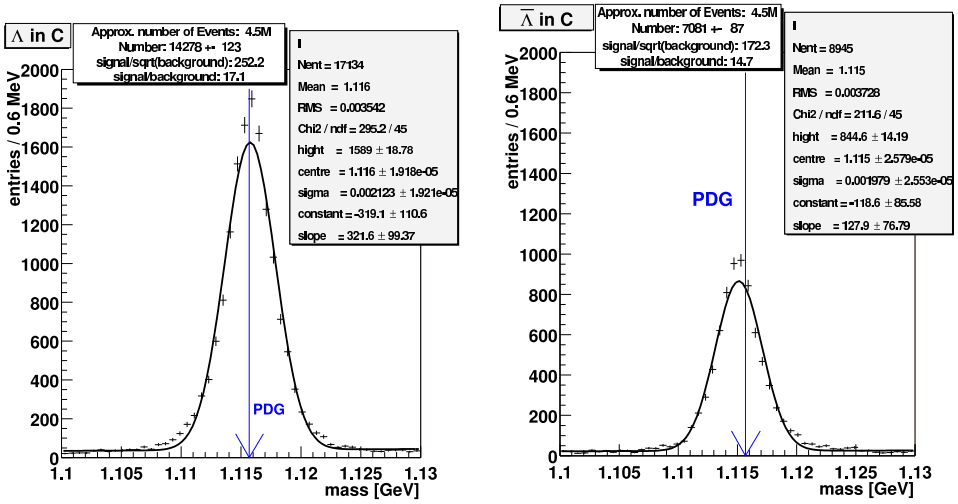

Figure 4.10: The Λ and $\overline{\Lambda}$ mass spectra: (a) Λ from the carbon run, (b) $\overline{\Lambda}$ from the carbon run, (c) Λ from the tungsten run, (d) $\overline{\Lambda}$ from the tungsten run.

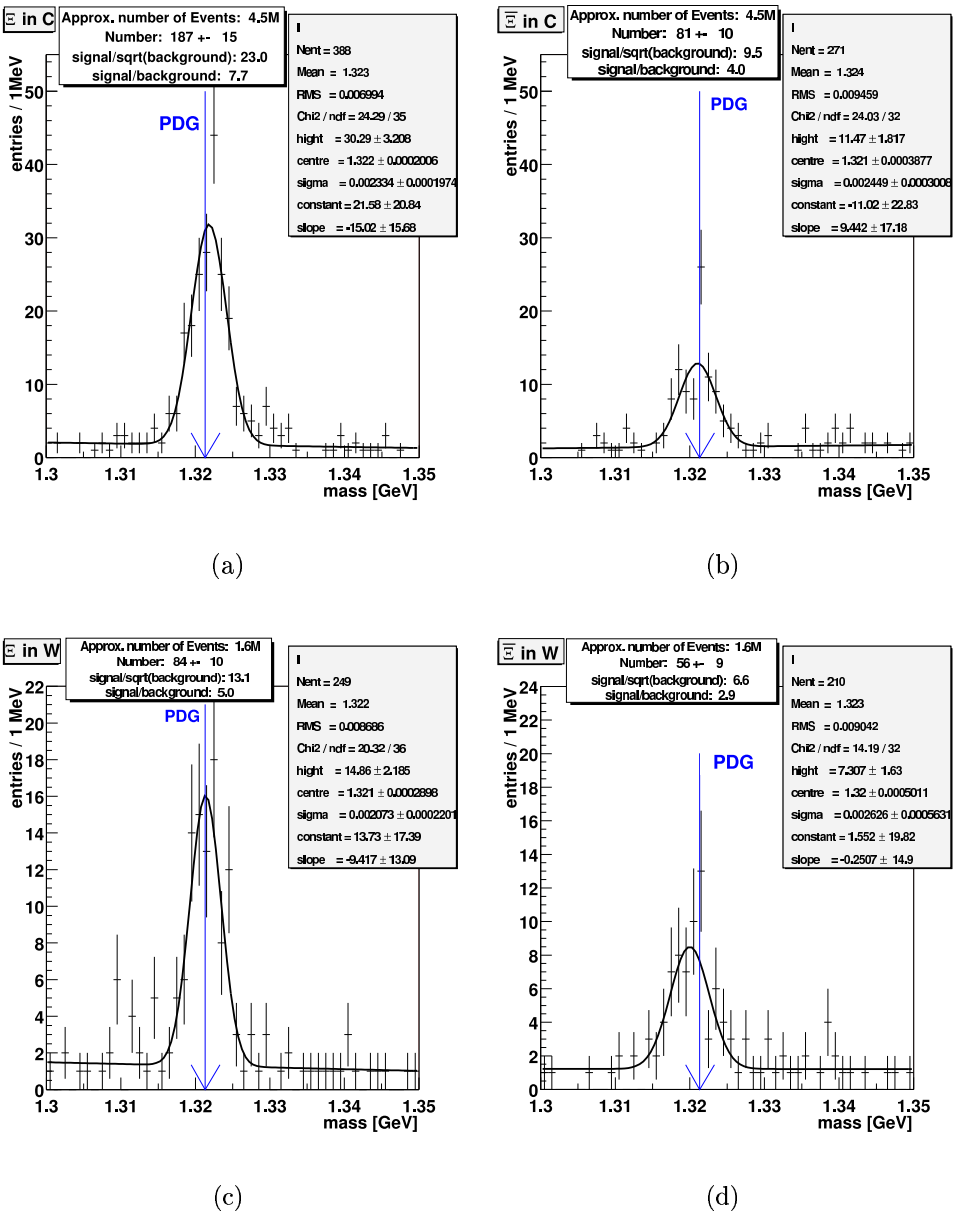

Figure 4.11: The Ξ and $\overline{\Xi}$ mass spectra: (a) Ξ from the carbon run, (b) $\overline{\Xi}$ from the carbon run, (c) Ξ from the tungsten run, (d) $\overline{\Xi}$ from the tungsten run.

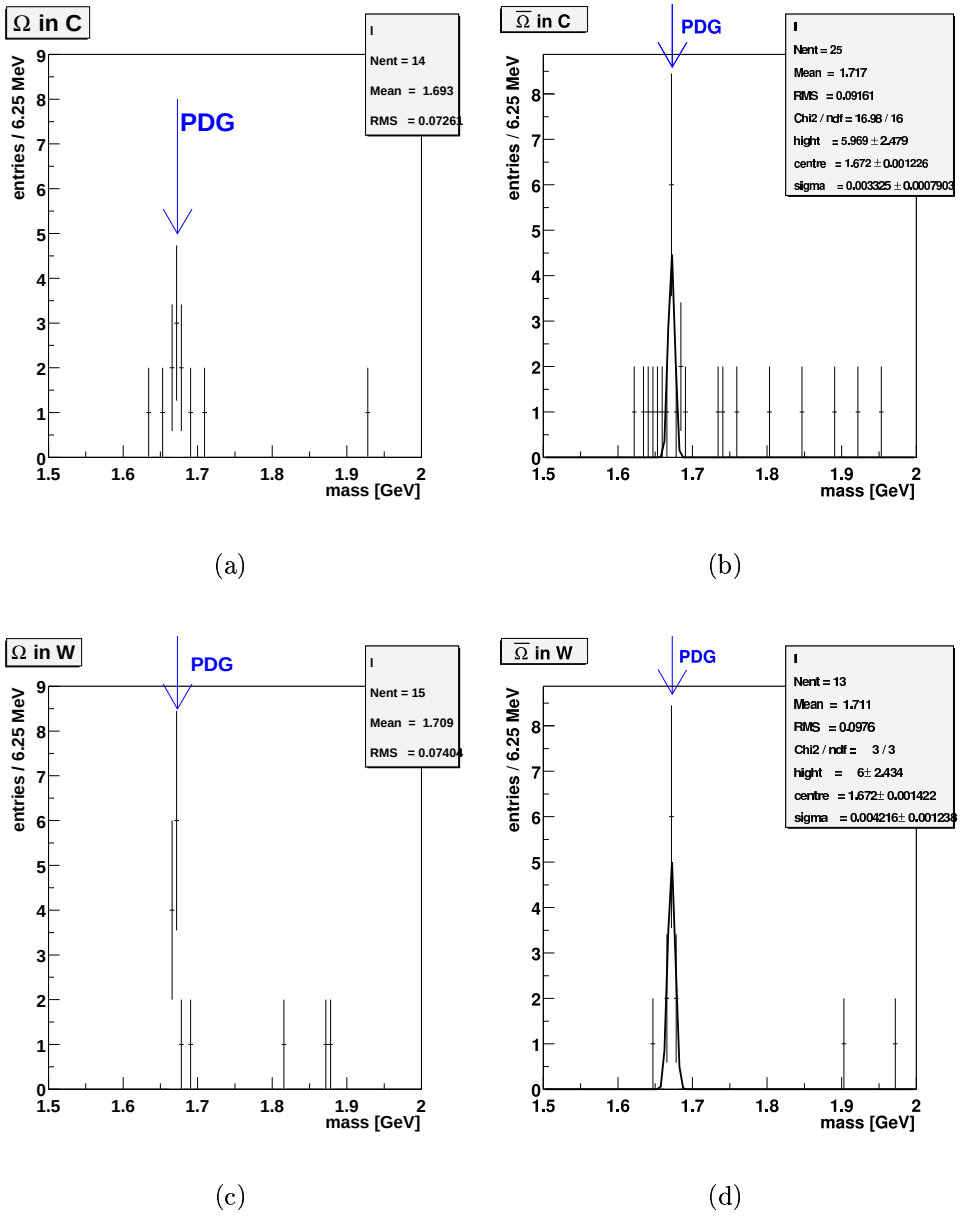

Figure 4.12: The Ω and $\overline{\Omega}$ mass spectra: (a) Ω from the carbon run, (b) $\overline{\Omega}$ from the carbon run, (c) Ω from the tungsten run, (d) $\overline{\Omega}$ from the tungsten run. A Gaussian could be fitted to the $\overline{\Omega}$ peaks.

particle	target material	number
Λ	C	14278 ± 123
$\overline{\Lambda}$	C	7081 ± 87
Λ	W	8804 ± 97
$\overline{\Lambda}$	W	3584 ± 63
Ξ	C	187 ± 15
$\overline{\Xi}$	C	81 ± 10
Ξ	W	84 ± 10
$\overline{\Xi}$	W	56 ± 9
Ω	C	6 ± 3
$\overline{\Omega}$	C	5 ± 3
Ω	W	11 ± 3
$\overline{\Omega}$	W	10 ± 3

Table 4.3: The number of hyperons reconstructed after all cuts in both runs, background subtracted. The values were calculated as described in the text.

Chapter 5

Main Analysis

The analysis work presented in this chapter, starts with a description of the Monte Carlo simulation. The main goal of the Monte Carlo simulation is to estimate the acceptance of the detector for the considered decays and the cuts presented in Chapter 4. Then the procedure to determine hyperon ratios and hyperon asymmetries are described. The chapter ends with the discussion of the systematic errors.

5.1 The Monte Carlo Simulation

The Monte Carlo method (see *e.g.* [Cow98]) is widely used in particle physics to determine the acceptance corrections needed. These acceptance corrections are necessary for a number of reasons. First, the detector does not cover the whole solid angle and thus a correction for the limited geometrical acceptance is needed. Second, the detector is not a perfect detector, but has finite efficiency and resolution. Not all particles may be seen and those which are recorded are measured with values of momentum and position smeared around the true values. And third, the cuts that were presented in Chapter 4 to select the desired particles cut away a part of the signal. The Monte Carlo simulation can provide these acceptances and thus the total acceptance of the whole analysis chain, necessary to obtain meaningful results.
First the employed standard tools will be described here. Then the settings applied for this Monte Carlo simulation are presented.

5.1.1 The HERA-B Monte Carlo Tools

The Monte Carlo is divided into two parts, the so called event generator, where the physical event is created, and the detector simulation, where the passage of the particle through the detector material and the hits in the detectors are described.

The Event generator

The standard HERA-B event generators also utilized in this analysis are the PYTHIA/JETSET [Sjö94] package that can simulate the proton–nucleon interaction and the FRITIOF [Pi92] package that can also simulate nuclear effects. A description of the implementation in the HERA-B environment and ARTE can be found in [Iva99]. The Monte Carlo generates single proton–nucleon collisions by using the PYTHIA/JETSET package for hard scattering processes, where the JETSET part does the fragmentation. FRITIOF simulates soft interactions by assuming that possible multiple scatterings on different nucleons are incoherent.

The Detector Simulation

The detector simulation for HERA-B is done by the standard tool GEANT [GEA93]. A description of the ARTE implementation can be found in [Now94]. GEANT propagates the particles through the detector including multiple scattering and the decay of long living particles. Therefore all material parts in the acceptance region have to be implemented with size, shape and position in GEANT.
The next step is the so called digitization. **M**onte Carlo **im**pact **p**oints (MIMP), which are the points where a particle hits a sub detector volume, are used to simulate detector hits. This means deciding whether a hit is produced and generating the hit according to the appropriate resolution function. After the digitization step, the Monte Carlo data are equivalent to unreconstructed real data. In addition, they contain the so called Monte Carlo truth, that is the tracks, vertices and MIMPs as generated by GEANT.
Then the data are reconstructed in the same way as the real data.

5.1.2 Steering and Settings of the Monte Carlo

The Monte Carlo production is split into two parts, the so called generation step, where the event generator and GEANT is called, and the reconstruction including the digitization.

The Generation Step

The way the hyperons were produced was the following. An inelastic event was created by the event generator. Then this event was searched for the kind of particle or anti-particle in question. This was done separately for Λ, Ξ and Ω, and if there was none, the event is rejected. For more detailed information see Appendix A.
Among the applied cuts the ones on the decay length and p_z of the Λ hyperons should be mentioned here. They are discussed in Section 5.4.1 about systematic errors.

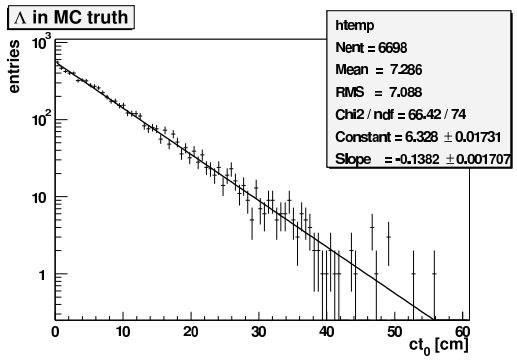

Figure 5.1: The ct_0 value, t_0 being the decay time of the particle in its rest frame, for Λ hyperons in the Monte Carlo truth tungsten run. An exponential function was fitted.

Since the decay of long living particles is affected by the propagation through the detector material, the decay of all ground state hyperons and kaons was performed by GEANT and not by the event generator. These particles were:

- K_S^0
- K_L^0
- $K^{+/-}$
- $\Sigma^{+/-/0}$
- Λ
- $\Xi^{-/0}$
- Ω^-

Digitization and Reconstruction

The steering file for the digitization and reconstruction is listed in Appendix A. The ARTE version was `ARTE-04-01-r2` and version 2.0903 of the geometry file, which defines the geometry of the detector for GEANT, was used, but with corrected target positions.

The Monte Carlo Truth Production

In the full simulation generation, the total numbers N_{full} of Λ, Ξ or Ω hyperons were counted and saved. In a second run with similar statistics N_T, without GEANT, but saving the momenta of all particles in question, the so called Monte Carlo truth was produced. The ratio $\frac{N_{full}}{N_T}$ was used to scale the results from the Monte Carlo truth production to the full simulation. A short run including GEANT was also done to check the decay lengths of the

particle	$c\tau$ in MC truth [cm]	PDG value $c\tau$ [cm] [Hag02]
Λ	7.24 ± 0.09	7.89
Ξ	4.72 ± 0.11	4.91
Ω	2.47 ± 0.18	2.46

Table 5.1: The $c\tau$ values in Monte Carlo truth.

particles in the Monte Carlo, as presented in Figure 5.1 for the Λ hyperons. An exponential function was fitted to the ct_0-distributions. From these we get $c\tau$ by $c\tau = \frac{1}{s}$ where s is the slope from the fit and τ is the average lifetime. In Table 5.1 the results are listed and compared to the reference values from the Particle Data Group. From these values only the value for the Λ hyperons deviates significantly by about 10% from the Particle Data Group value.
In Table A.1 the numbers of produced particles in the Monte Carlo are listed. An overview of the Monte Carlo production with comparison to the handling of the real data can be seen in Figure 5.2

5.2 Acceptance Corrections

The acceptance is obtained by dividing the distributions of the Monte Carlo data that was processed applying the same selection criteria and cuts as the real data by the Monte Carlo truth scaled appropriately. The real data distribution divided by this number yields the acceptance corrected measured number. So to get *e.g.* the number of Λ hyperons in the carbon run, this number from the real data has to be divided by the acceptance for Λ hyperons in that run obtained by the Monte Carlo. The method is only reliable, if the distributions (like lifetime τ or transverse momentum p_t) of the Monte Carlo have a similar shape like those of the data. Therefore, the distribution from the Monte Carlo data will be compared with the real data in this section.

5.2.1 Comparison real Data – Monte Carlo Simulation

In Figures 5.3(a) to 5.10(a) and 5.11(a) to 5.11(d), the mass peaks in the Monte Carlo are seen. The widths of the Λ and Ξ peaks are all about a factor 0.7 smaller than in the real data (see Fig. 4.10 and 4.11 for comparison). In Figures 5.3 to 5.10 different variables are plotted for Λ and Ξ with comparison to the Monte Carlo simulation. For the Monte Carlo distributions in the comparison, in contrary to the mass peaks, only candidates that are a Λ, Ξ or Ω (known from the Monte Carlo truth ARTE tables) were accepted, and only those not originating from a particle decaying in GEANT, as listed in

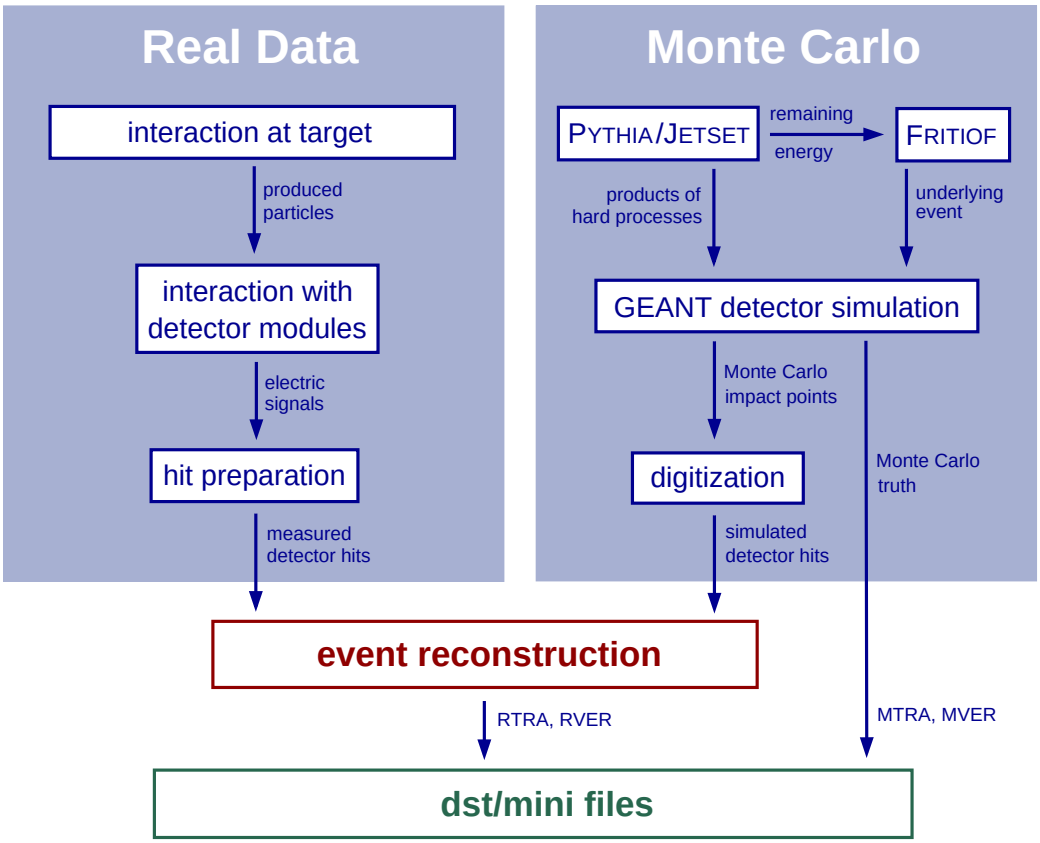

Figure 5.2: The Comparison of the Monte Carlo production to the handling of real data, taken from [Aga01]. Note that the Monte Carlo truth is saved *before* GEANT is called, except for the check on the decay length (see text).

Section 5.1.2. This ensures that the acceptances are consistent, since those decays are also not counted in the Monte Carlo truth generation. The signals were obtained with the selections and cuts discussed in Chapter 4, applied to the data as well as to the Monte Carlo. The data was also background corrected, which was not necessary for the Monte Carlo, which is background free at this stage. The background was taken in the range $[c-9\sigma, c-6\sigma]$ and $[c+6\sigma, c+9\sigma]$ to reduce the contribution from the signal that does not have a perfect Gaussian shape as is obvious for the Λ mass peaks.
Due to the poor statistics this was not feasible for the Ω hyperons for all variables. But in Figure 5.11 βct_0 is plotted together with the Monte Carlo distribution for the Ω and $\overline{\Omega}$ hyperons both for the carbon and the tungsten run. In all these plots the Monte Carlo histograms are normalized to the number of entries in the data histograms.
Data and Monte Carlo agree within errors for most distributions. Exceptions are the squared transverse momentum p_t^2 of the Λ and Ξ hyperons. For the Λ particles also the rapidity y in the center of mass system and the Feynman x_f in the Monte Carlo deviate from the data. Even the Monte Carlo distribution of the azimuthal angle ϕ of the Λ hyperons is not correct (see Fig. 5.3(f)) while it is correct for the $\overline{\Lambda}$ (see Fig. 5.5(e)). This must be due to an incorrect description of the detector efficiencies. All these disagreements between the Monte Carlo and the data give rise to systematic errors discussed later in Section 5.4.
The agreement of the Monte Carlo Ω βct_0 distribution with the data does not only show that the Monte Carlo is reliable, but also that the particles in the data are indeed Ω hyperons. The same argument holds for Λ and Ξ.
The corresponding calculated acceptances for Λ and Ξ hyperons are shown in Figures 5.12 to 5.15.

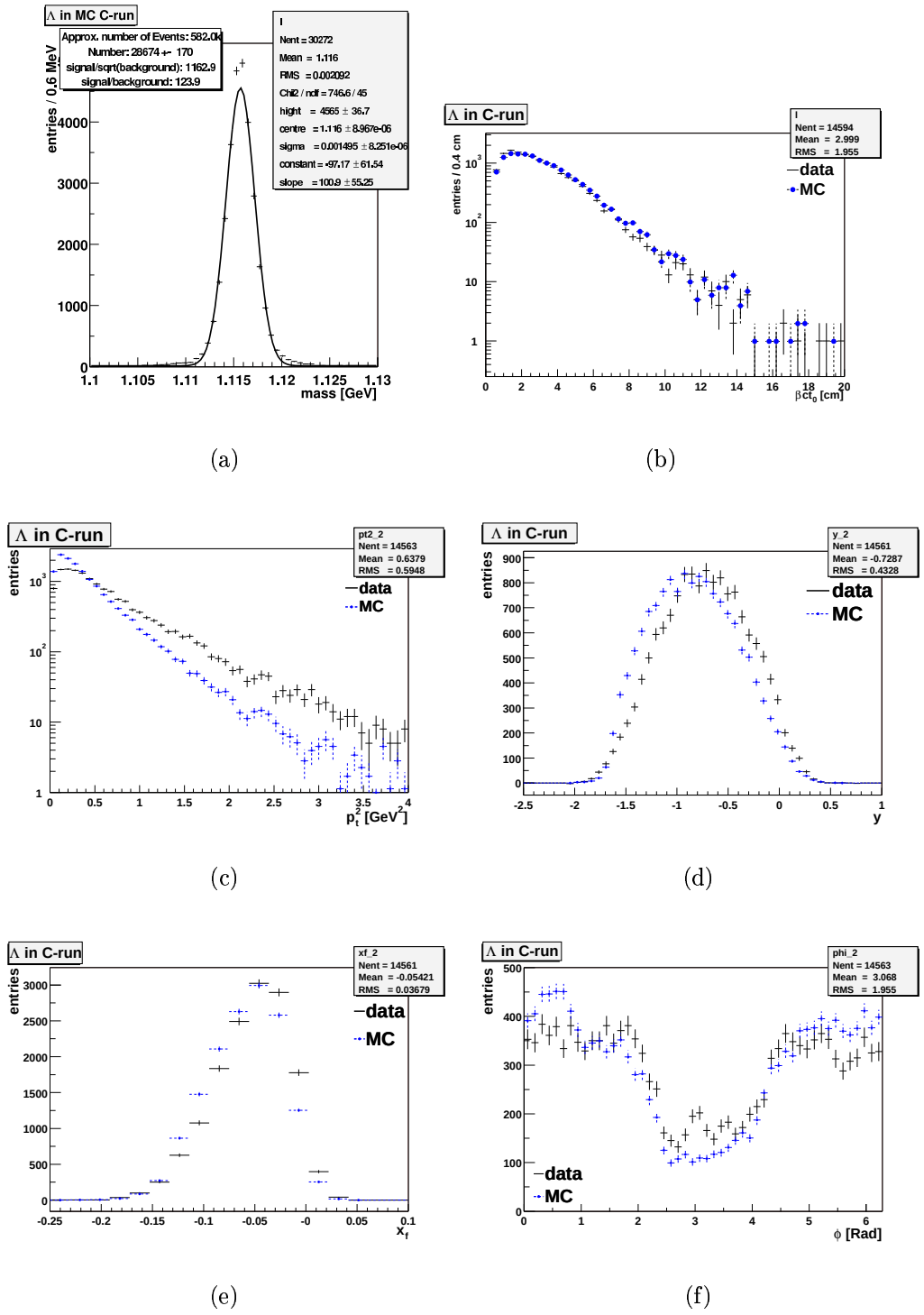

(a) (b)

(c) (d)

(e) (f)

Figure 5.3: The comparison of Monte Carlo and data and the mass peak in the Monte Carlo for the Λ hyperons in the carbon run. Plotted are mass peak (a), flight lengths boosted to the rest frame of the particle βct_0 (b), transverse momentum squared p_t^2 (c), rapidity y in the center of mass system (d), Feynman x_f (e) and azimuthal angle ϕ (f). The Monte Carlo distributions are normalized to the number of entries of the real data histogram.

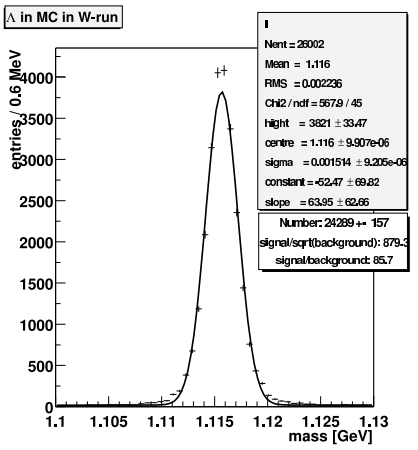

(a)

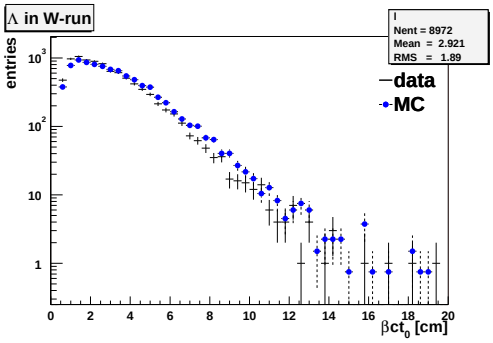

(b)

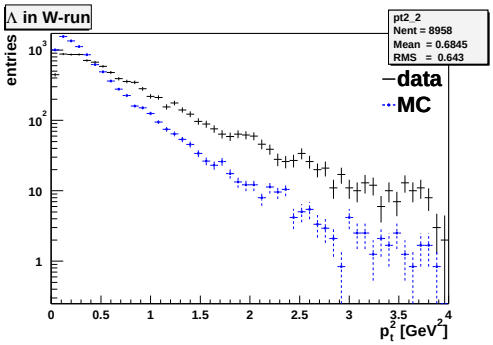

(c)

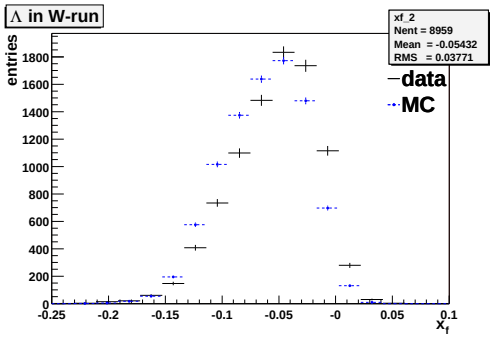

(d)

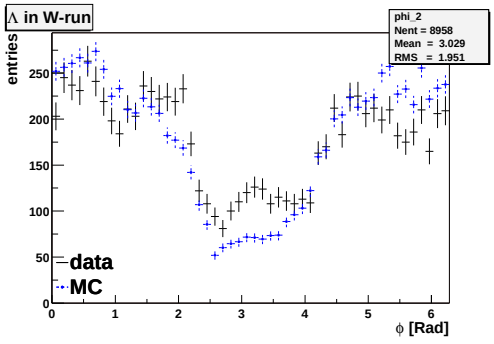

(e)

Figure 5.4: The comparison of Monte Carlo and data and the mass peak in the Monte Carlo for the Λ hyperons in the tungsten run. Plotted are mass peak (a), flight lengths boosted to the rest frame of the particle βct_0 (b), transverse momentum squared p_t^2 (c), Feynman x_f (d) and azimuthal angle ϕ (e). The Monte Carlo distributions are normalized to the number of entries of the real data histogram.

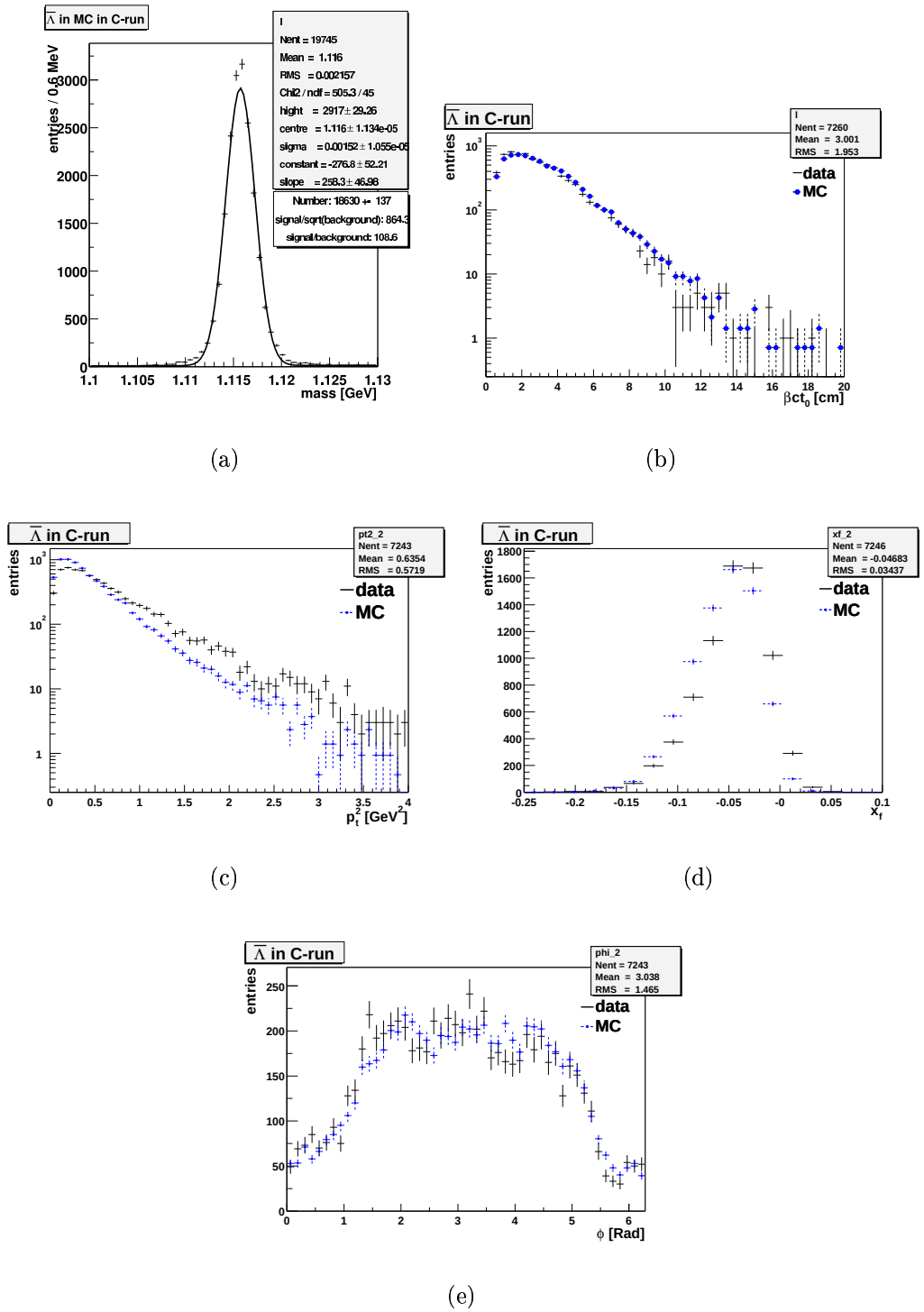

Figure 5.5: The comparison of Monte Carlo and data and the mass peak in the Monte Carlo for the $\overline{\Lambda}$ hyperons in the carbon run. Plotted are mass peak (a), flight lengths boosted to the rest frame of the particle βct_0 (b), transverse momentum squared p_t^2 (c), Feynman x_f (d) and azimuthal angle ϕ (e). The Monte Carlo distributions are normalized to the number of entries of the real data histogram.

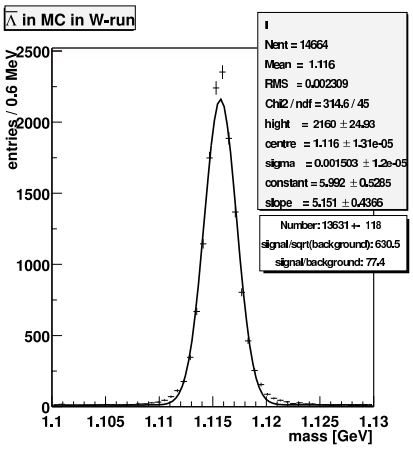

(a)

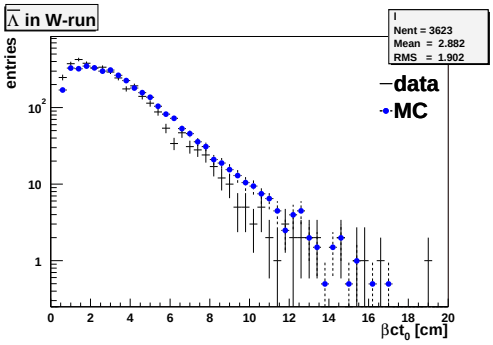

(b)

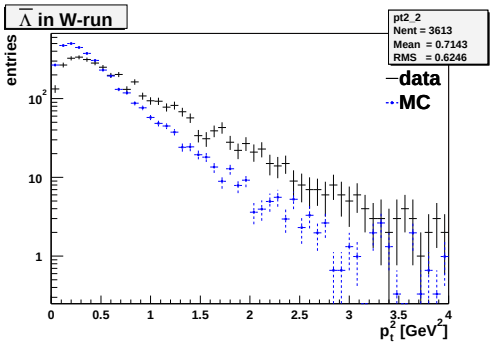

(c)

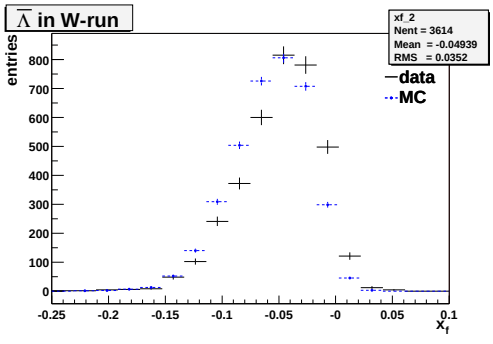

(d)

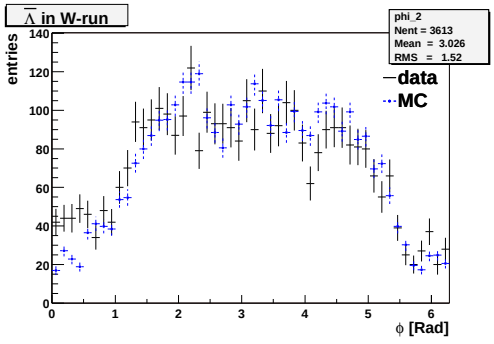

(e)

Figure 5.6: The comparison of Monte Carlo and data and the mass peak in the Monte Carlo for the $\overline{\Lambda}$ hyperons in the tungsten run. Plotted are mass peak (a), flight lengths boosted to the rest frame of the particle βct_0 (b), transverse momentum squared p_t^2 (c), Feynman x_f (d) and azimuthal angle ϕ (e). The Monte Carlo distributions are normalized to the number of entries of the real data histogram.

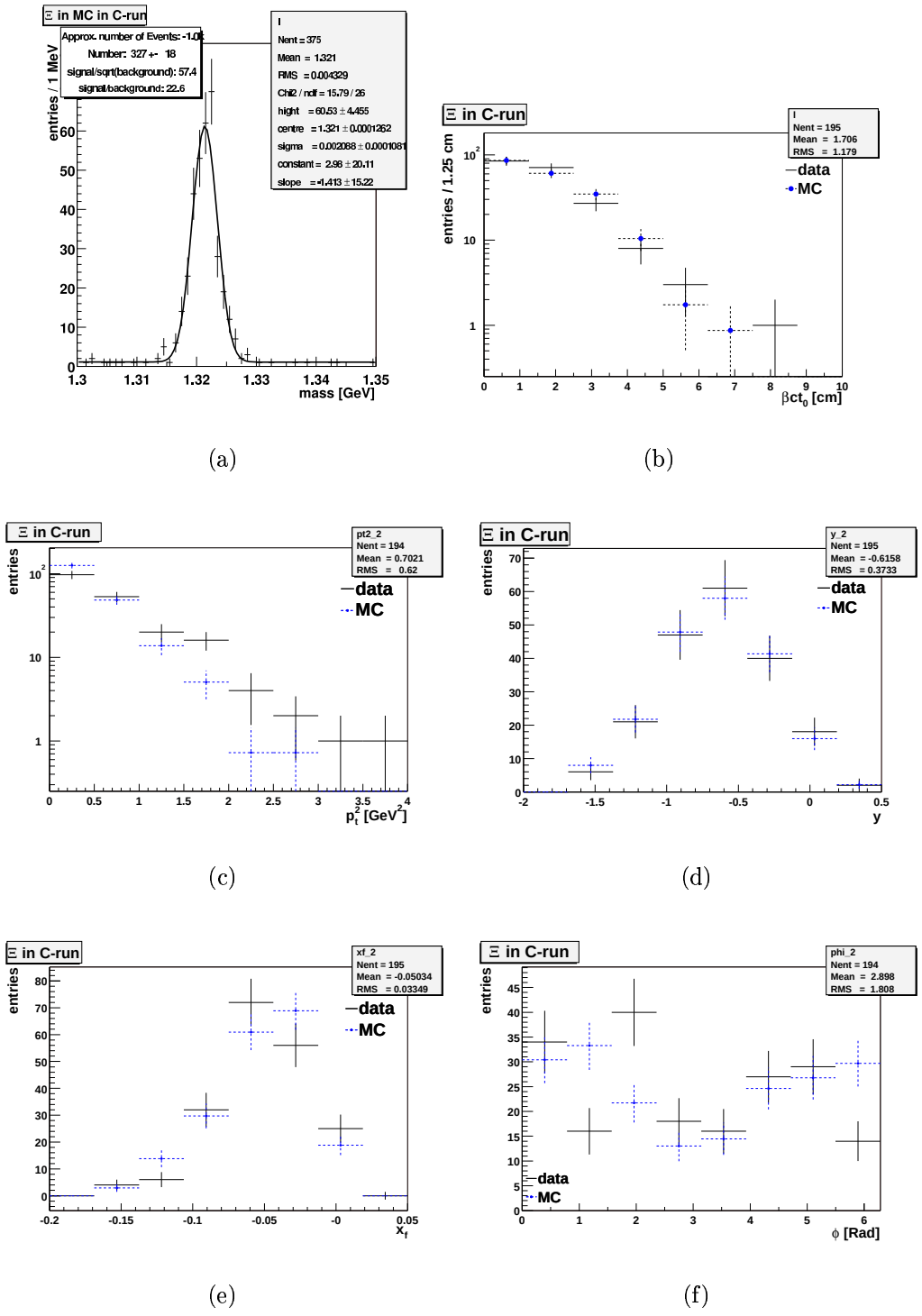

Figure 5.7: The comparison of Monte Carlo and data and the mass peak in the Monte Carlo for the Ξ hyperons in the carbon run. Plotted are mass peak (a), flight lengths boosted to the rest frame of the particle $\beta c t_0$ (b), transverse momentum squared p_t^2 (c), rapidity y in the center of mass system (d), Feynman x_f (e) and azimuthal angle ϕ (f). The Monte Carlo distributions are normalized to the number of entries of the real data histogram.

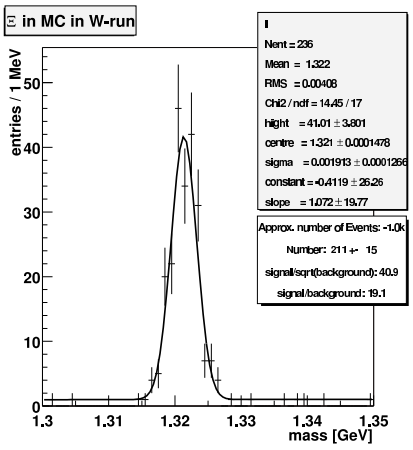

(a)

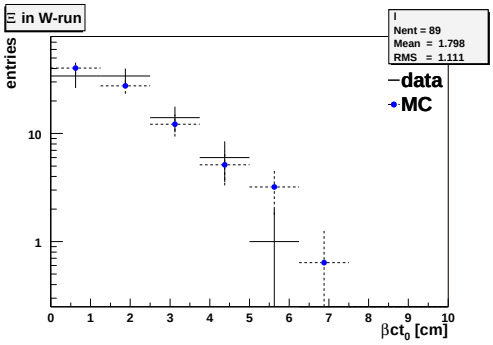

(b)

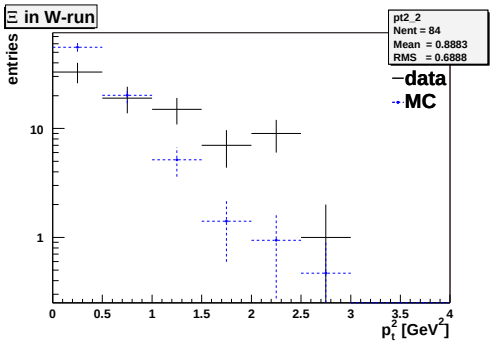

(c)

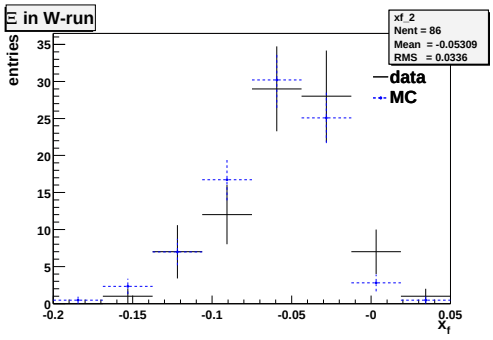

(d)

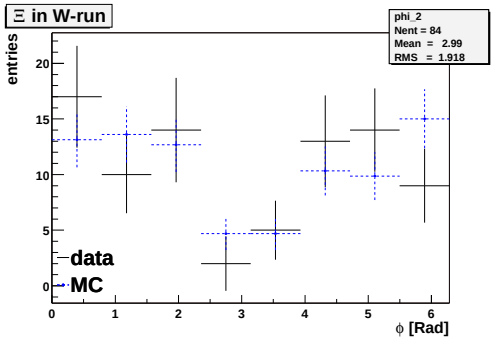

(e)

Figure 5.8: The comparison of Monte Carlo and data and the mass peak in the Monte Carlo for the Ξ hyperons in the tungsten run. Plotted are mass peak (a), flight lengths boosted to the rest frame of the particle βct_0 (b), transverse momentum squared p_t^2 (c), Feynman x_f (d) and azimuthal angle ϕ (e). The Monte Carlo distributions are normalized to the number of entries of the real data histogram.

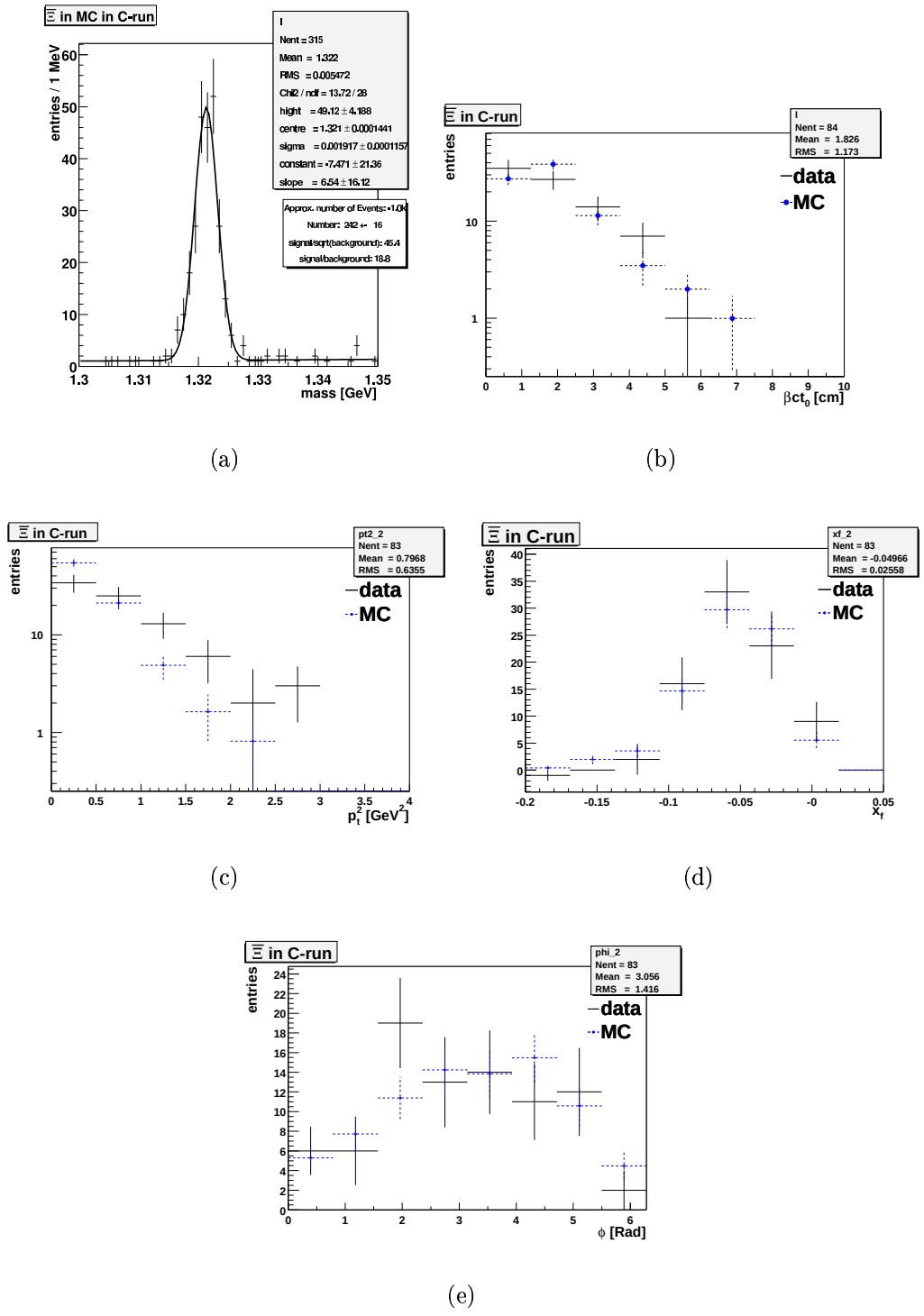

Figure 5.9: The comparison of Monte Carlo and data and the mass peak in the Monte Carlo for the $\overline{\Xi}$ hyperons in the carbon run. Plotted are mass peak (a), flight lengths boosted to the rest frame of the particle βct_0 (b), transverse momentum squared p_t^2 (c), Feynman x_f (d) and azimuthal angle ϕ (e). The Monte Carlo distributions are normalized to the number of entries of the real data histogram.

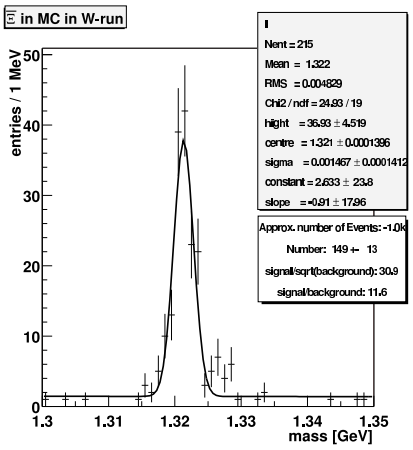

(a)

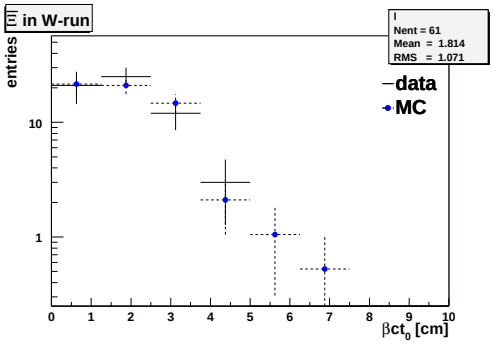

(b)

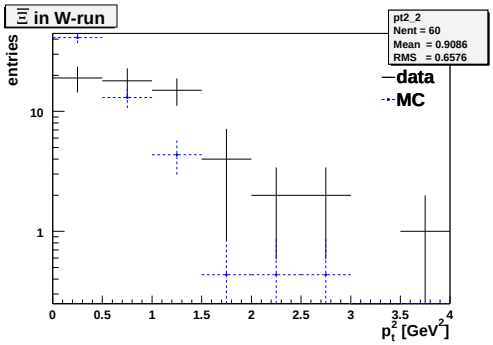

(c)

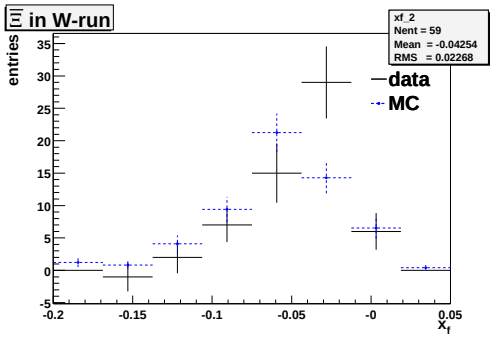

(d)

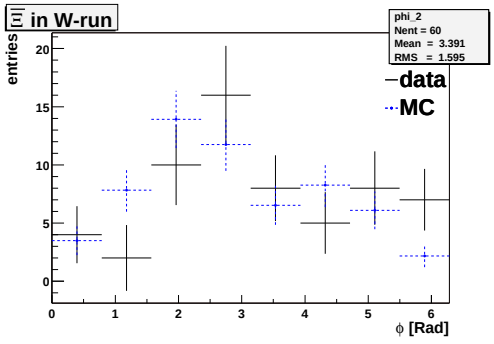

(e)

Figure 5.10: The comparison of Monte Carlo and data and the mass peak in the Monte Carlo for the $\overline{\Xi}$ hyperons in the tungsten run. Plotted are mass peak (a), flight lengths boosted to the rest frame of the particle βct_0 (b), transverse momentum squared p_t^2 (c), Feynman x_f (d) and azimuthal angle ϕ (e). The Monte Carlo distributions are normalized to the number of entries of the real data histogram.

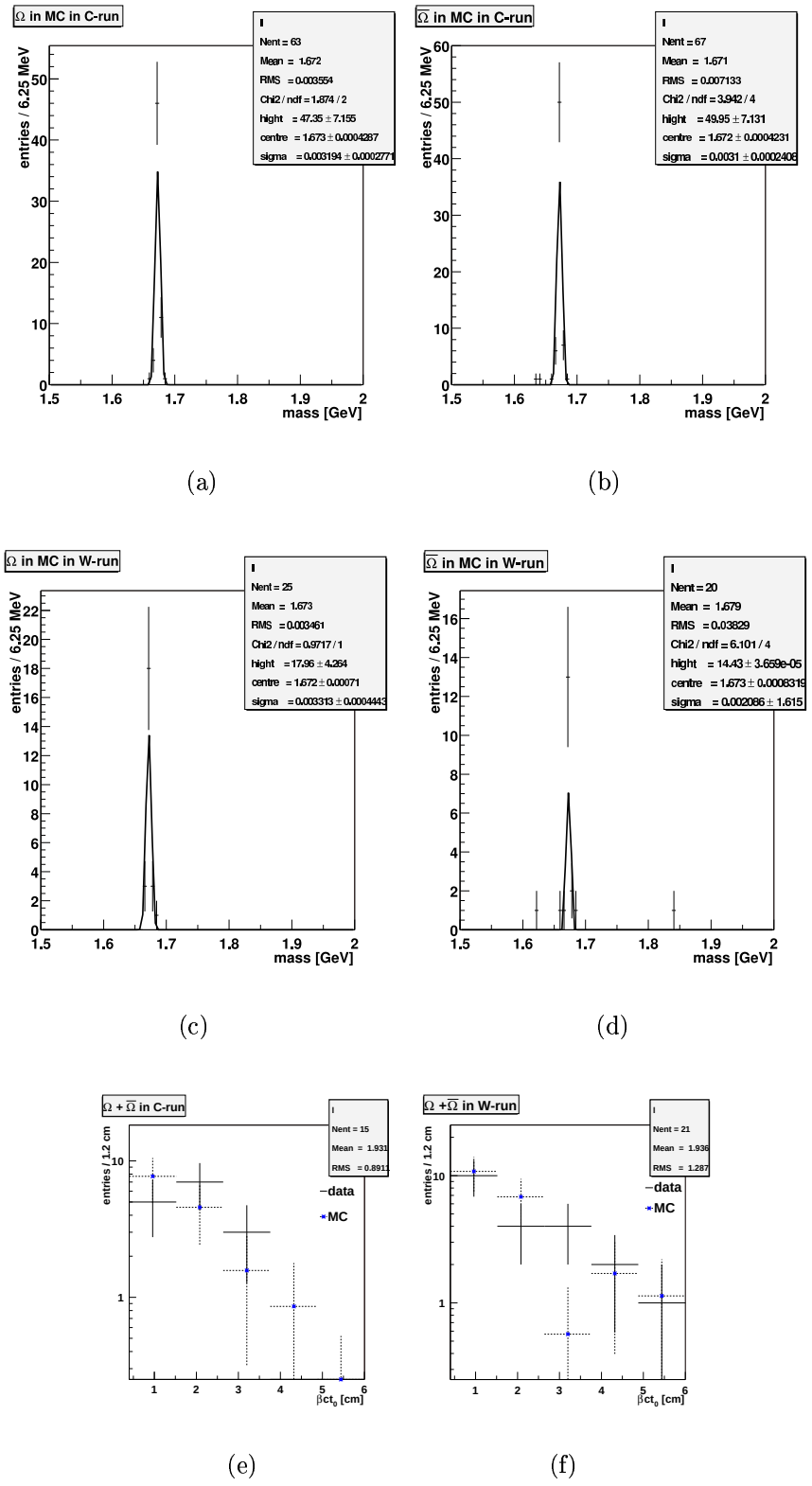

Figure 5.11: The mass peaks of the Ω and $\overline{\Omega}$ hyperons in the Monte Carlo, Ω in the C-run (a), $\overline{\Omega}$ in the C-run (b), Ω in the W-run (c), $\overline{\Omega}$ in the W-run (d). And comparison of Monte Carlo and data for the Ω hyperons in the carbon (e) and tungsten (f) run. Plotted are flight lengths boosted to the rest frame of the particle βct_0 for Ω *and* $\overline{\Omega}$. The Monte Carlo distributions are normalized to the number of entries of the real data histogram.

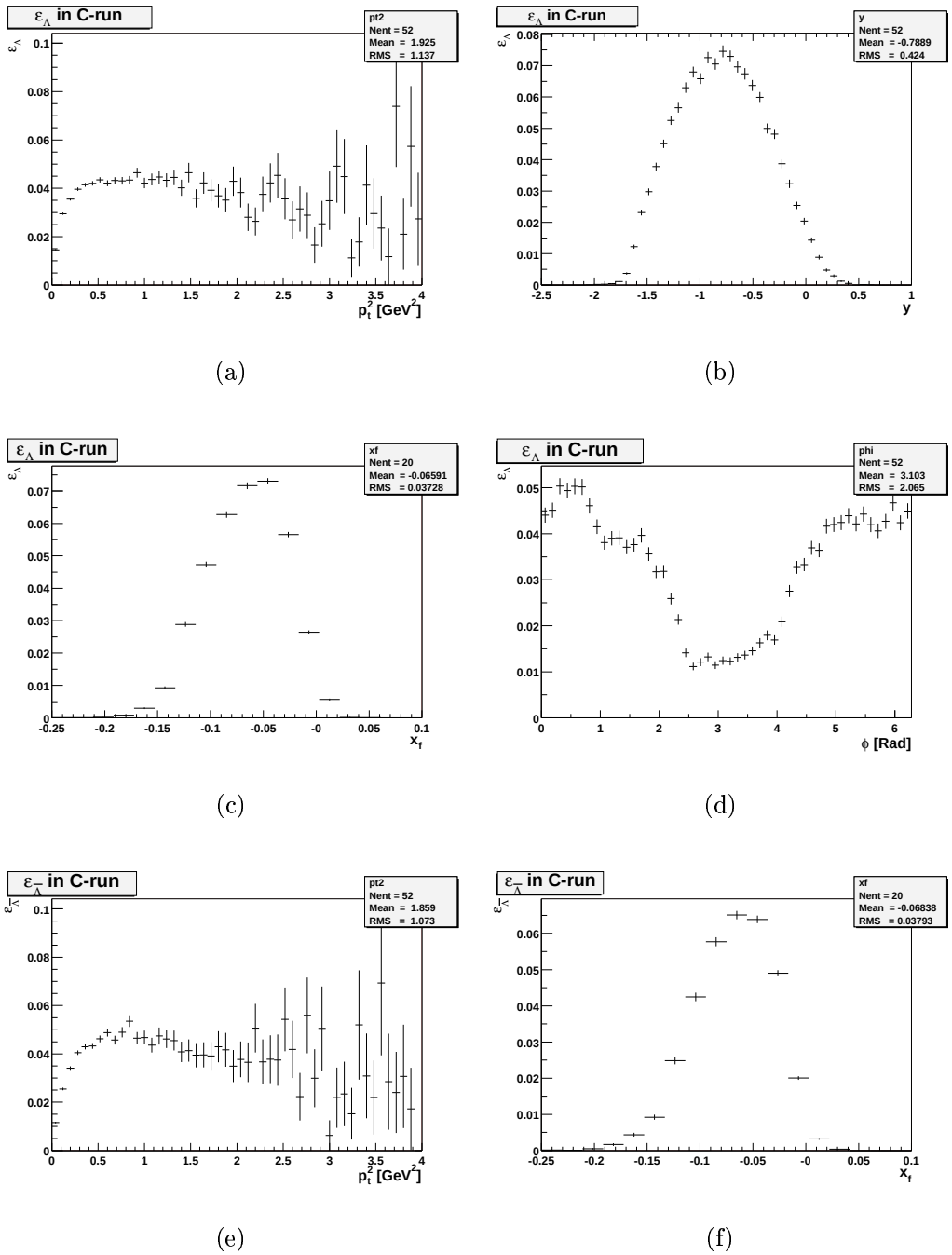

Figure 5.12: The acceptances for the Λ hyperons in the carbon run. Plotted are transverse momentum squared p_t^2 (a), rapidity y in the center of mass system (b), Feynman x_f (c) and azimuthal angle ϕ (d). And for the $\overline{\Lambda}$ hyperons transverse momentum squared p_t^2 (e), Feynman x_f (f).

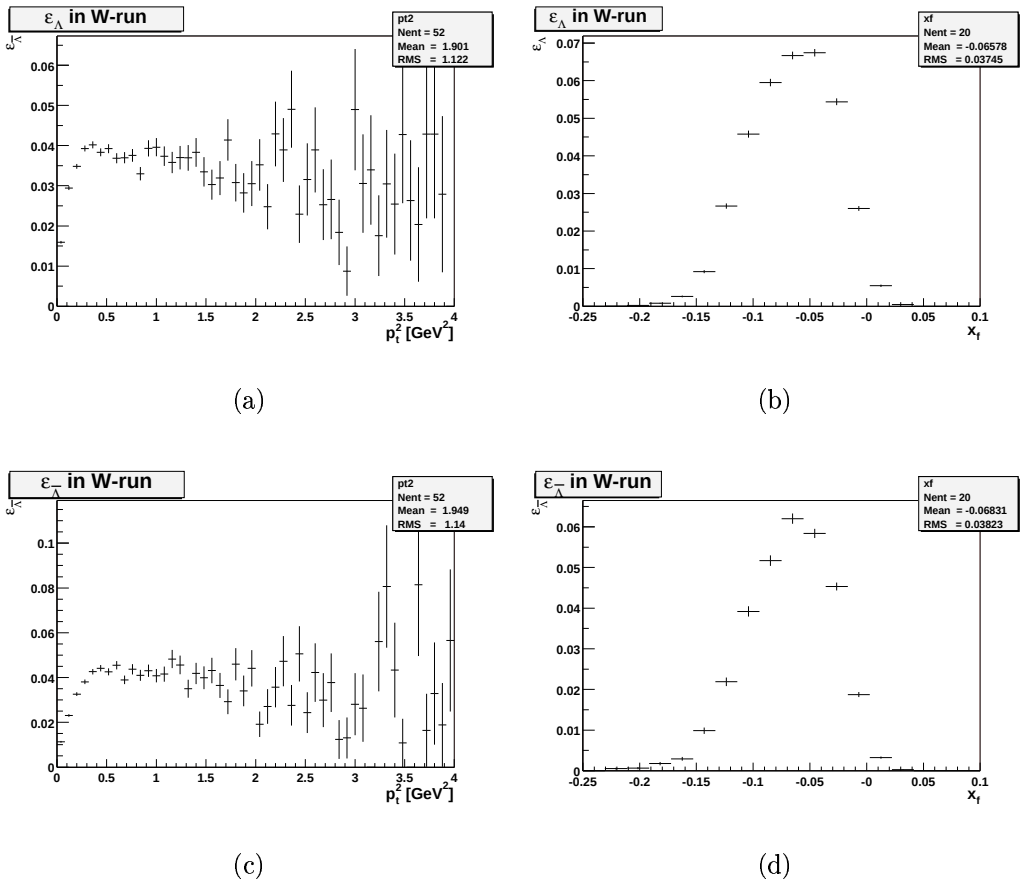

(a) (b)

(c) (d)

Figure 5.13: The acceptances for the Λ hyperons in the tungsten run. Plotted are transverse momentum squared p_t^2 (a), Feynman x_f (b), for $\overline{\Lambda}$ transverse momentum squared p_t^2 (c), Feynman x_f (d).

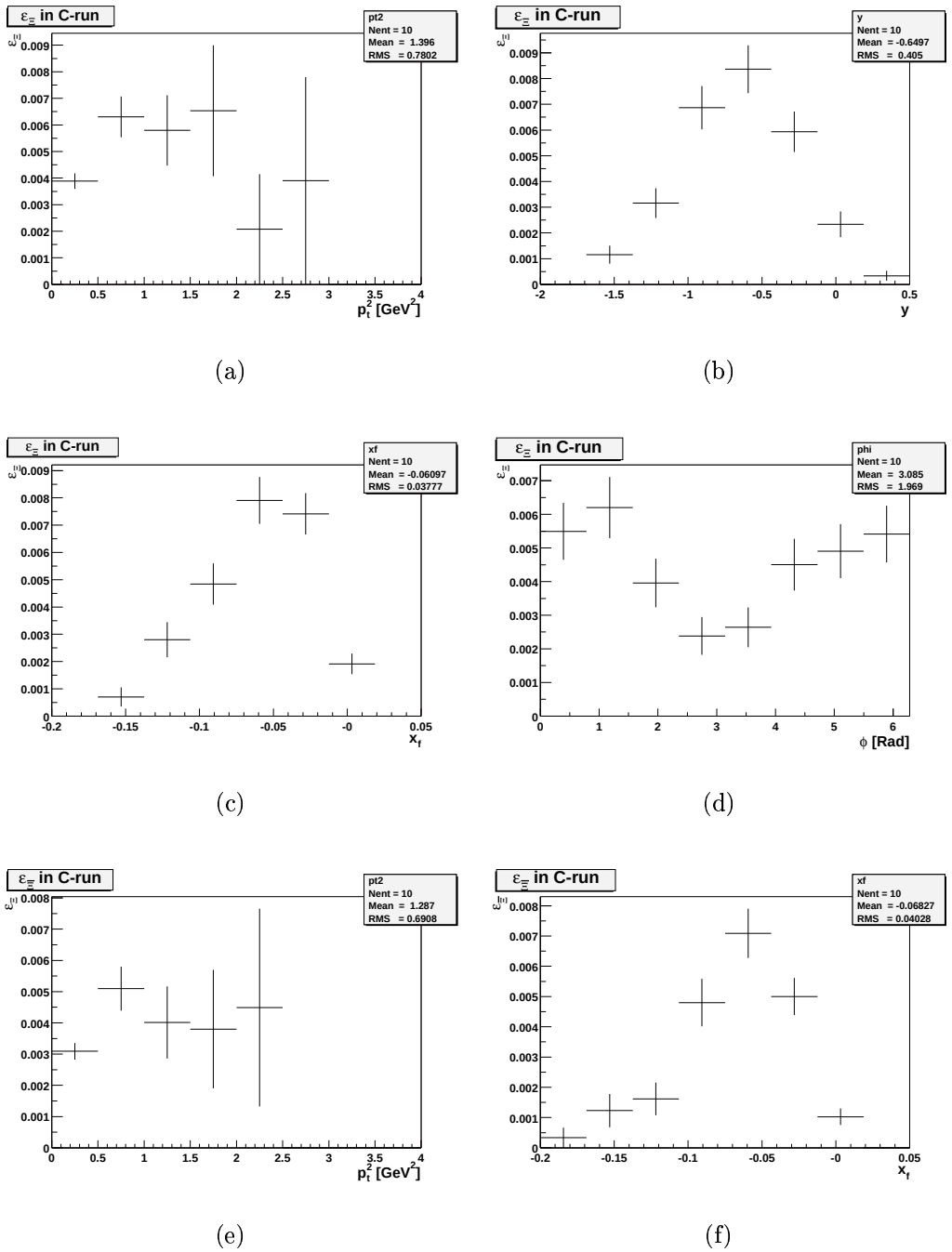

Figure 5.14: The acceptances for the Ξ hyperons in the carbon run. Plotted are transverse momentum squared p_t^2 (a), rapidity y in the center of mass system (b), Feynman x_f (c) and azimuthal angle ϕ (d). And for the $\overline{\Xi}$ hyperons transverse momentum squared p_t^2 (e), Feynman x_f (f).

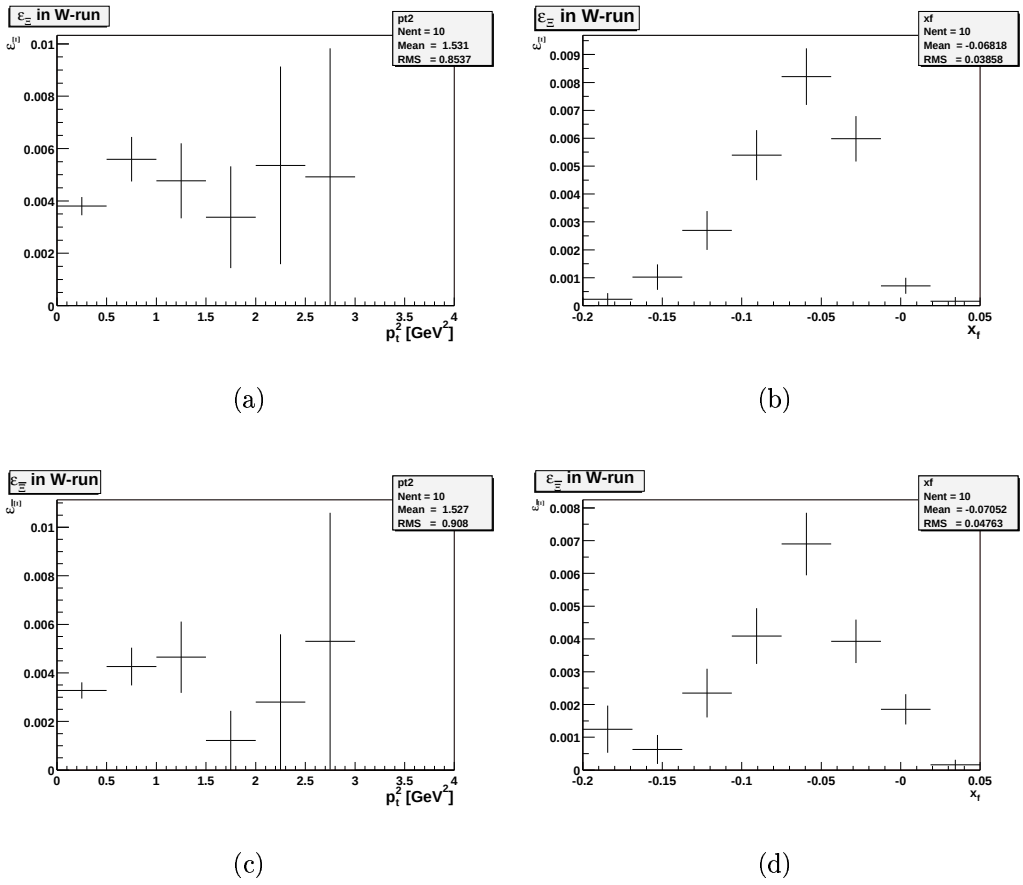

Figure 5.15: The acceptances for the Ξ hyperons in the tungsten run. Plotted are transverse momentum squared p_t^2 (a), Feynman x_f (b) and for the $\overline{\Xi}$ hyperons p_t^2 (c), Feynman x_f (d).

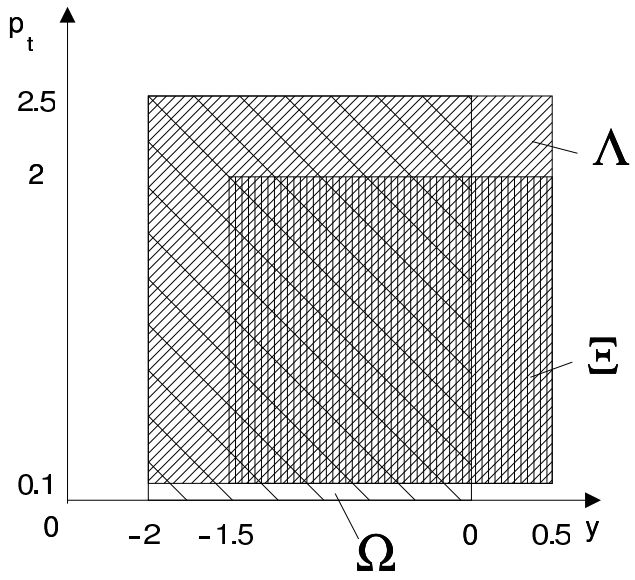

Figure 5.16: The accessible kinematic regions: Λ region with 0.1 GeV $< p_t <$ 2.5 GeV and $-2.0 < y < 0.5$, Ξ region with 0.1 GeV $< p_t <$ 2 GeV and $-1.5 < y < 0.5$ and Ω region with 0 GeV $< p_t <$ 2.5 GeV and $-2 < y < 0$

5.3 Hyperon Ratios and Asymmetries

In this section it is described how the results on the hyperon ratios, integrated and differential in p_t^2 and x_f, and the hyperon asymmetries were obtained.

5.3.1 The integrated Hyperon Ratios

The hyperon ratios were calculated for four different kinematic regions. First all particles were accepted, also in the Monte Carlo truth, leading to an extrapolation to the whole phase space, since the Monte Carlo Data was produced filling the whole phase space. This of course implies relying on the Monte Carlo to describe the distributions of the particles well in the region outside the detector acceptance. Looking at Section 5.2.1, the agreement between Monte Carlo and data is not very good, leaving doubts of the correctness of this extrapolation. Qualitatively however, the distributions in the Monte Carlo should be correct over the whole phase space. An alternative approach to extrapolate to the whole phase space is presented in Section 5.3.2.
The kinematic regions where the particles were detected are the following. The second region after the whole phase space is the region of Λ acceptance with 0.1 GeV $< p_t <$ 2.5 GeV and $-2.0 < y < 0.5$, also called Λ region later on. The third region is the so called Ξ region of 0.1 GeV $< p_t <$ 2 GeV and $-1.5 < y < 0.5$, where also the number of particles of Λ and Ω are calculated to get also ratios like $\frac{\Xi}{\Lambda}$ etc. The last region is the Ω region of 0

run	ratio	value	MC truth
C	$\frac{\overline{\Lambda}}{\Lambda}$	0.204 ± 0.004	0.259
	$\frac{\overline{\Xi}}{\Xi}$	0.39 ± 0.07	0.69
	$\frac{\Xi}{\Lambda}$	0.040 ± 0.004	0.052
	$\frac{\overline{\Xi}}{\Lambda}$	0.078 ± 0.011	0.139
	$\frac{\overline{\Omega}}{\Omega}$	1.2 ± 1.0	1.3
	$\frac{\Omega}{\Xi}$	0.029 ± 0.016	0.12
	$\frac{\overline{\Omega}}{\overline{\Xi}}$	0.09 ± 0.06	0.22
W	$\frac{\overline{\Lambda}}{\Lambda}$	0.198 ± 0.005	0.262
	$\frac{\overline{\Xi}}{\Xi}$	0.64 ± 0.15	0.69
	$\frac{\Xi}{\Lambda}$	0.034 ± 0.005	0.050
	$\frac{\overline{\Xi}}{\Lambda}$	0.11 ± 0.02	0.13
	$\frac{\overline{\Omega}}{\Omega}$	1.4 ± 0.7	1.3
	$\frac{\Omega}{\Xi}$	0.18 ± 0.07	0.10
	$\frac{\overline{\Omega}}{\overline{\Xi}}$	0.40 ± 0.18	0.18

Table 5.2: The hyperon ratios extrapolated to the whole phase space, obtained as stated in the text. The last column gives the Monte Carlo truth prediction.

GeV $< p_t <$ 2.5 GeV and $-2 < y < 0$. These regions are depicted in Figure 5.16.

Extrapolation to the whole Phase Space

For this part, the numbers of all three kinds of hyperons and their antiparticles were taken, as they were obtained in section 4.5. The same procedure was applied to the reconstructed Monte Carlo using only Λ, Ξ and Ω candidates that do not come from decays of particles listed in Section 5.1.2. This also means that the numbers used here differ from those in the mass peaks seen in the Figures 5.3 to 5.11. A few of these particles remained in the Monte Carlo, if the event in addition contained a directly produced Λ or a Λ coming from a resonance. This implies that Λ hyperons coming from Σ^0 decays are taken into account in these ratios. By only accepting candidates that are a Λ, Ξ or Ω the background vanishes and a simple Gaussian can be fitted to the signal. Thus the numbers were obtained by adding the 3σ region of that Gaussian and taking their square root as the error. For clarity, this calculation will be shown in an example, the ratio $\frac{\overline{\Lambda}}{\Lambda}$ in the carbon run.

We have defined the acceptance by dividing the number of particles in the Monte Carlo after reconstruction and cuts by the number of particles in the Monte Carlo truth after scaling, *i.e.* for the Λ candidates: $\varepsilon_\Lambda = \frac{24976 \pm 158}{2945388} = (8.48 \pm 0.05) \cdot 10^{-3}$. The same was applied on the $\overline{\Lambda}$, giving $\varepsilon_{\overline{\Lambda}} = (0.0206 \pm 0.0002)$. Using the numbers of particles in the data after the cuts from Figure 4.10, we get the real number of Λ hyperons in the carbon run by dividing this number by the just obtained acceptance: $\#\Lambda = \frac{14278 \pm 123}{(8.48 \pm 0.05)10^{-3}} = (1.684 \pm 0.018) \cdot 10^6$, where the error of the result is obtained by Gaussian error propagation. For ratios with other hyperons, we also include the branching ratio of 63.9 ± 0.5 % [Hag02] by dividing by it, giving $\#\Lambda_{\mathrm{BR}} = (2.64 \pm 0.04) \cdot 10^6$. But for the value $\frac{\overline{\Lambda}}{\Lambda}$, the value determined first was used, since the branching ratios are equal for particles and anti-particles. For the $\overline{\Lambda}$, we get $\#\overline{\Lambda} = (0.344 \pm 0.005) \cdot 10^6$ and $\#\overline{\Lambda}_{\mathrm{BR}} = (0.538 \pm 0.009) \cdot 10^6$. This gives $\frac{\overline{\Lambda}}{\Lambda} = 0.204 \pm 0.004$.
The other ratios listed in Table 5.2 were determined in the same way.

The Ratios in the different kinematic Regions

In the different regions mentioned above, the same method was applied as for the integrated ratios, but applying cuts on p_t and y selecting the corresponding region. The result is shown in Table 5.3. For the Ω candidates, the distribution in p_t–y is plotted in Figure 5.17. Due to the low background, a background correction was not necessary. In addition $\frac{\overline{\Lambda}}{\Lambda}$ was also calculated for smaller kinematical regions as seen in Table 5.4 for the carbon and Table 5.5 for the tungsten run.

5.3.2 The differential Hyperon Ratios and Extrapolation to $x_f = 0$

The Particle Distributions

In Figures 5.18 to 5.21 the background and acceptance corrected distributions of the Λ and Ξ hyperons are shown. These are obtained using the distributions as determined in Section 5.2.1 for the data, divided by the distributions for the acceptance. Also shown in the figures are the Monte Carlo truth predictions for these distributions normalized to the same integral. As for the uncorrected data, the Monte Carlo truth does not describe the Λ data well.
From the Monte Carlo, we can also get an estimate for the impact of Λ baryons from Σ^0 decays. In Figure 5.22 the y- and p_t^2-distribution of the Λ hyperons coming from Σ^0 decays that were kept in Monte Carlo events with a directly produced Λ or a Λ from a resonance decay is shown. Also shown are the distributions of the Λ hyperons not coming from Σ^0 decays, normalized to the same integral. The distributions look very similar. Thus

region & run	ratio	value	MC truth
Λ, C	$\frac{\overline{\Lambda}}{\Lambda}$	0.477 ± 0.009	0.604
Λ, W	$\frac{\overline{\Lambda}}{\Lambda}$	0.390 ± 0.009	0.519
Ξ, C	$\frac{\overline{\Lambda}}{\Lambda}$	0.576 ± 0.011	0.733
	$\frac{\overline{\Xi}}{\Xi}$	0.55 ± 0.09	0.97
	$\frac{\overline{\Xi}}{\Lambda}$	0.083 ± 0.008	0.109
	$\frac{\overline{\Xi}}{\Lambda}$	0.079 ± 0.011	0.144
	$\frac{\overline{\Omega}}{\Omega}$	1.0 ± 0.9	1.3
	$\frac{\Omega}{\Xi}$	0.043 ± 0.023	0.07
	$\frac{\overline{\Omega}}{\overline{\Xi}}$	0.08 ± 0.07	0.13
Ξ, W	$\frac{\overline{\Lambda}}{\Lambda}$	0.474 ± 0.011	0.638
	$\frac{\overline{\Xi}}{\Xi}$	0.79 ± 0.19	0.93
	$\frac{\Xi}{\Lambda}$	0.058 ± 0.009	0.091
	$\frac{\overline{\Xi}}{\Lambda}$	0.097 ± 0.017	0.132
	$\frac{\overline{\Omega}}{\Omega}$	1.4 ± 0.8	1.1
	$\frac{\Omega}{\Xi}$	0.26 ± 0.11	0.06
	$\frac{\overline{\Omega}}{\overline{\Xi}}$	0.44 ± 0.20	0.10
Ω, C	$\frac{\overline{\Omega}}{\Omega}$	1.3 ± 1.1	1.4
Ω, W	$\frac{\overline{\Omega}}{\Omega}$	1.3 ± 0.7	1.2

Table 5.3: The hyperon ratios for the different regions. The last column gives the Monte Carlo truth prediction. The regions are: Λ: 0.1 GeV $< p_t <$ 2.5 GeV and $-2.0 < y < 0.5$, Ξ: 0.1 GeV $< p_t <$ 2.0 GeV and $-1.5 < y < 0.5$, Ω: 0 GeV $< p_t <$ 2.5 GeV and $-2 < y < 0$.

p_t region	y region	$\frac{\overline{\Lambda}}{\Lambda}$
0.1 GeV $< p_t <$ 1.0 GeV	$-1.375 < y < -0.75$	0.46 ± 0.01
	$-0.75 < y < -0.125$	0.67 ± 0.02
	$-0.125 < y < 0.5$	0.94 ± 0.08
1.0 GeV $< p_t <$ 1.9 GeV	$-1.375 < y < -0.75$	0.43 ± 0.04
	$-0.75 < y < -0.125$	0.53 ± 0.04
	$-0.125 < y < 0.5$	0.66 ± 0.07

Table 5.4: The ratio $\frac{\overline{\Lambda}}{\Lambda}$ for different kinematic regions for the carbon run.

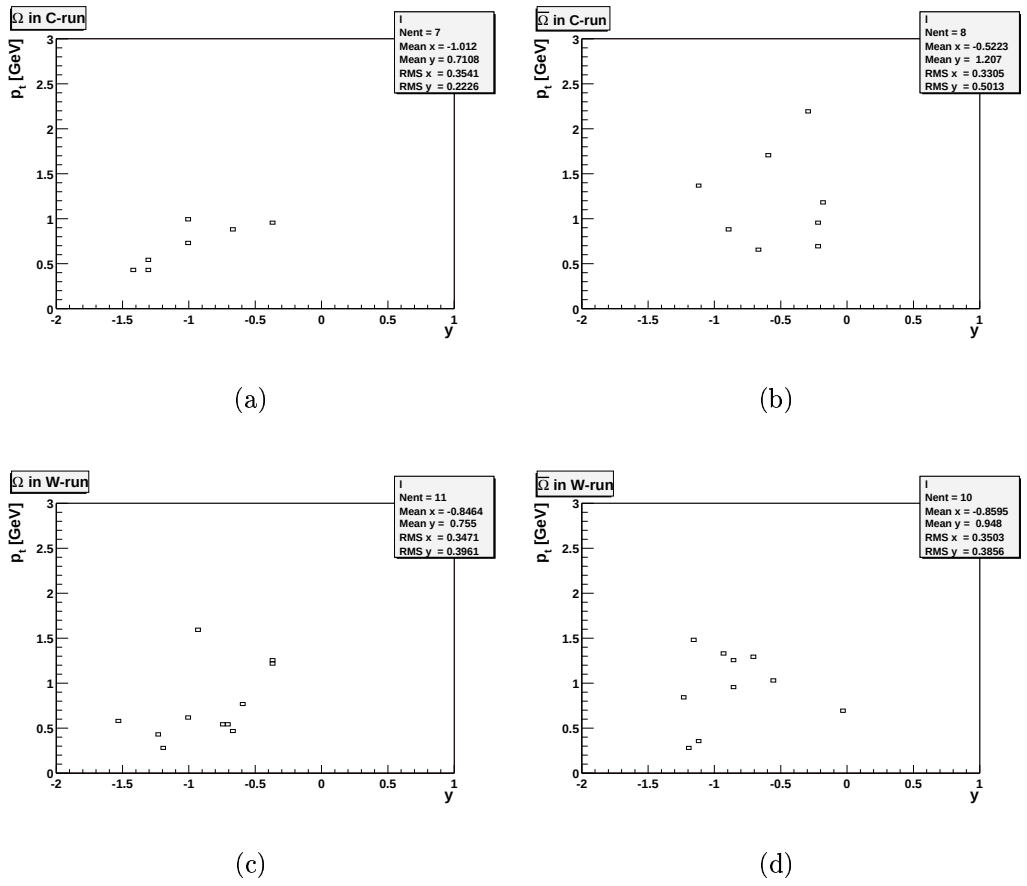

Figure 5.17: The p_t–y-distribution of the Ω candidates (a), $\overline{\Omega}$ candidates (b) in the carbon run, Ω candidates (c), $\overline{\Omega}$ candidates (d) in the tungsten run

p_t region	y region	$\frac{\overline{\Lambda}}{\Lambda}$
0.1 GeV $< p_t <$ 1.0 GeV	$-1.375 < y < -0.75$	0.41 ± 0.02
	$-0.75 < y < -0.125$	0.50 ± 0.02
	$-0.125 < y < 0.5$	0.76 ± 0.09
1.0 GeV $< p_t <$ 1.9 GeV	$-1.375 < y < -0.75$	0.33 ± 0.04
	$-0.75 < y < -0.125$	0.50 ± 0.04
	$-0.125 < y < 0.5$	0.47 ± 0.06

Table 5.5: The ratio $\frac{\overline{\Lambda}}{\Lambda}$ for different kinematic regions for the tungsten run.

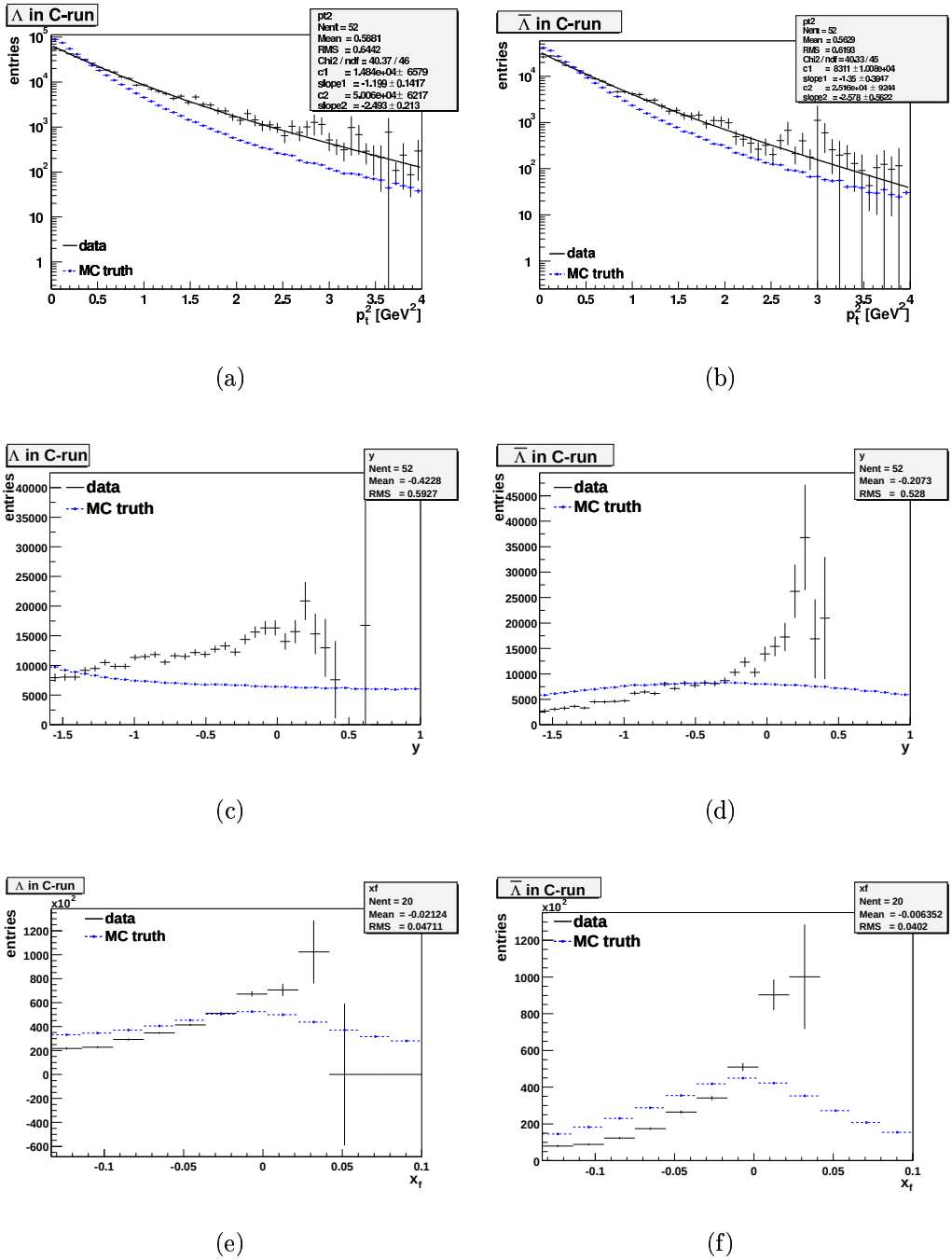

Figure 5.18: The acceptance and background corrected distributions for the carbon run. p_t^2 for Λ (a), $\overline{\Lambda}$ (b), y-distributions of Λ (c), $\overline{\Lambda}$ (d), and the x_f-distributions of Λ (e) and $\overline{\Lambda}$ (f) in the carbon run. Dashed is the Monte Carlo truth, normalized to the same integral. The fits are fits of the function $c1 \cdot \exp(slope1 \cdot p_t^2) + c2 \cdot \exp(slope2 \cdot p_t^2)$.

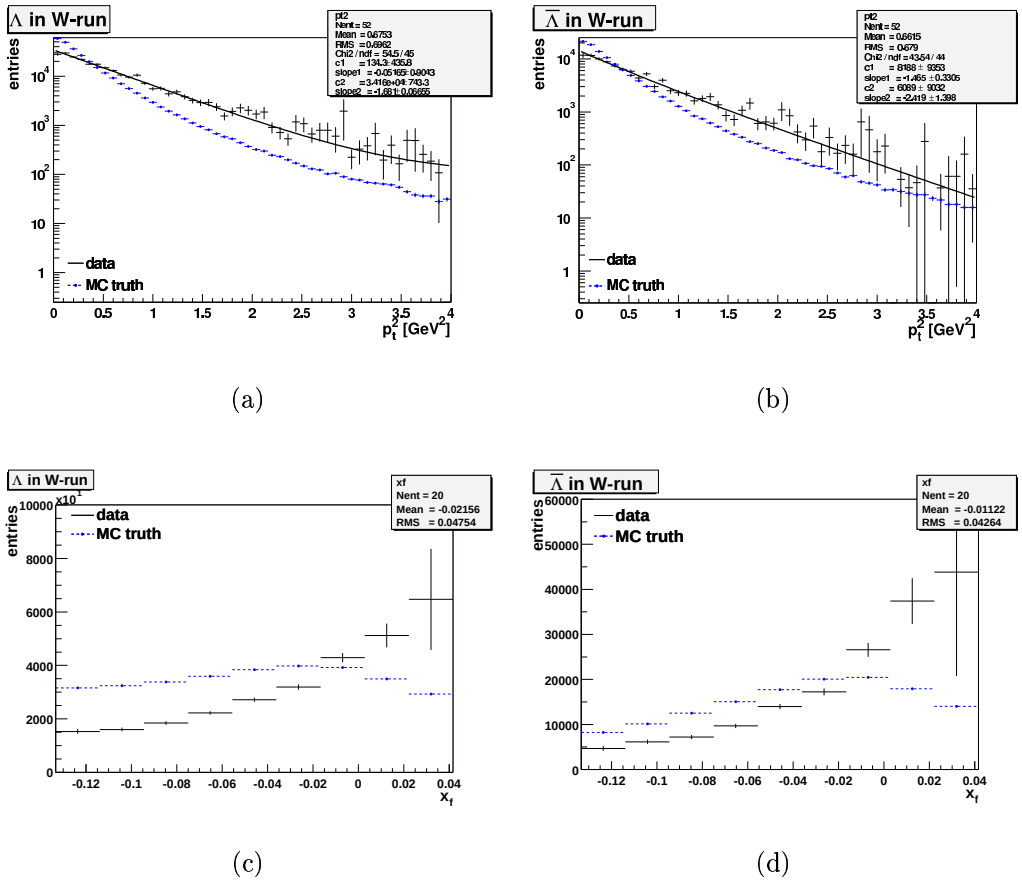

Figure 5.19: The acceptance and background corrected distributions for the tungsten run. p_t^2 for Λ (a), $\overline{\Lambda}$ (b) and the x_f-distributions of Λ (c) and $\overline{\Lambda}$ (d). Dashed is the Monte Carlo truth, normalized to the same integral. The fits are fits of the function $c1 \cdot \exp(slope1 \cdot p_t^2) + c2 \cdot \exp(slope2 \cdot p_t^2)$.

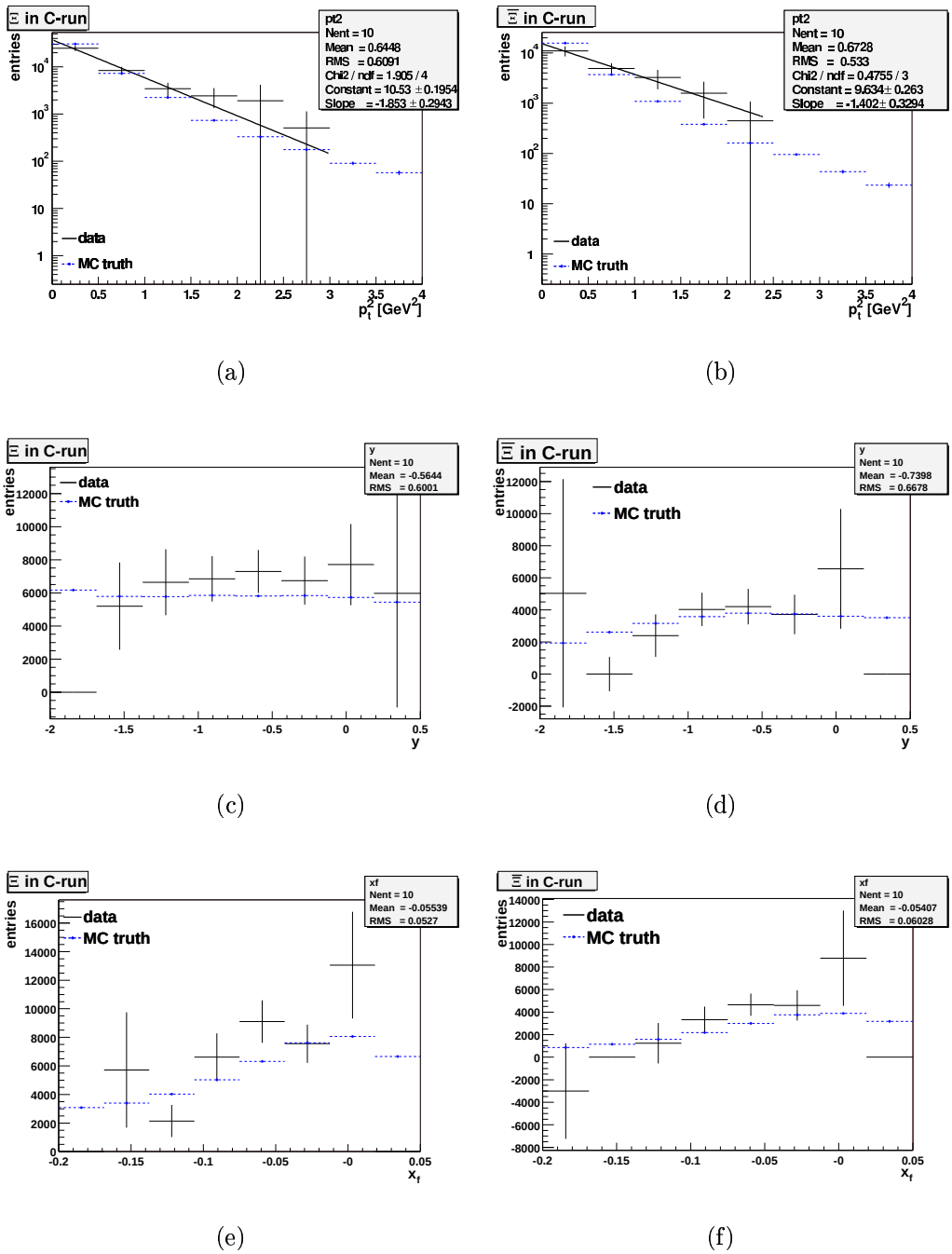

Figure 5.20: The acceptance and background corrected distributions for the carbon run. p_t^2 for Ξ (a), $\overline{\Xi}$ (b), y-distributions of Ξ (c), $\overline{\Xi}$ (d), and the x_f-distributions of Ξ (e) and $\overline{\Xi}$ (f). Dashed is the Monte Carlo truth, normalized to the same integral. The fits are fits of the function $Constant \cdot \exp(slope \cdot p_t^2)$.

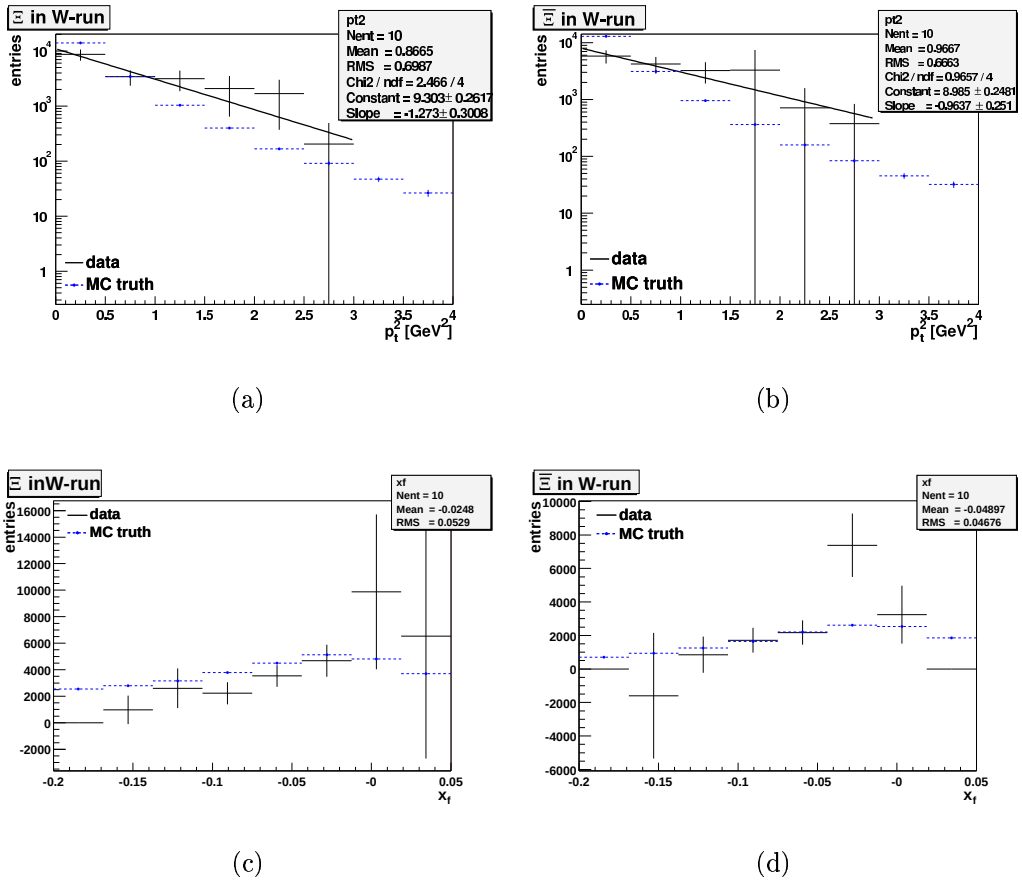

Figure 5.21: The acceptance and background corrected distributions for the tungsten run. p_t^2 for Ξ (a), $\overline{\Xi}$ (b) and the x_f-distributions of Ξ (c) and $\overline{\Xi}$ (d). Dashed is the Monte Carlo truth, normalized to the same integral. The fits are fits of the function $Constant \cdot \exp(slope \cdot p_t^2)$.

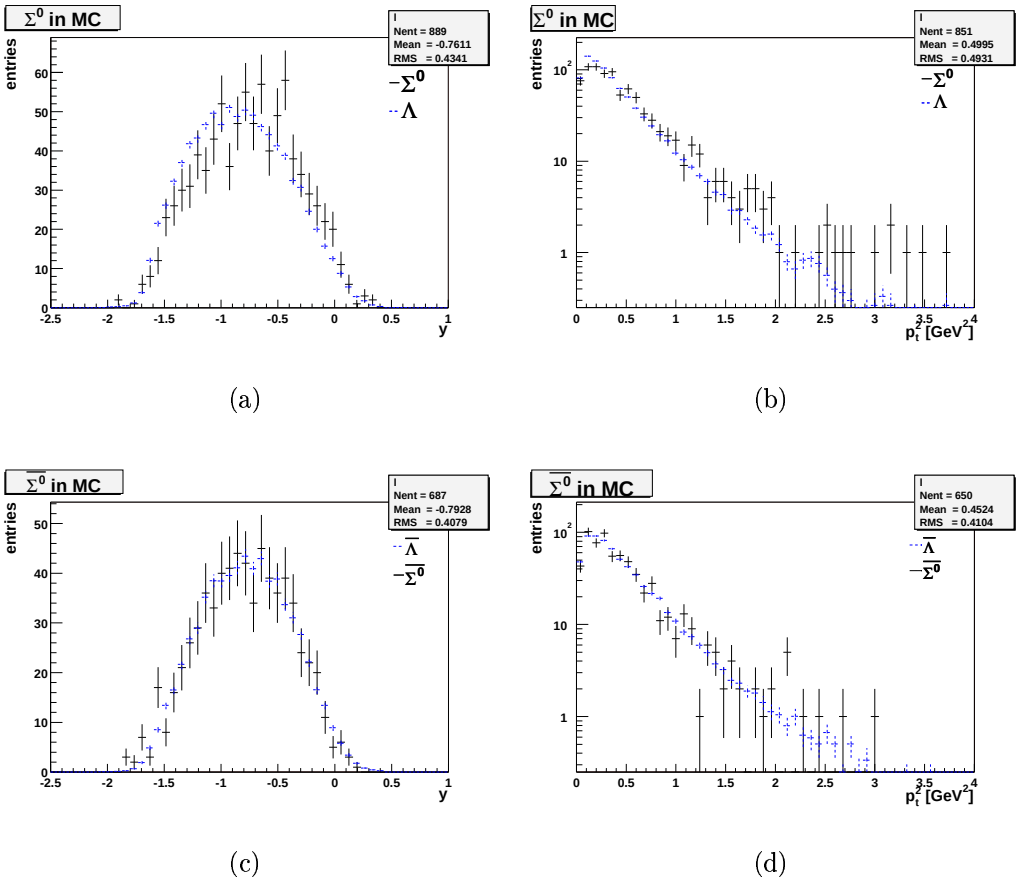

(a) (b)

(c) (d)

Figure 5.22: Comparison of Λ hyperons from Σ^0 decays and direct Λ hyperons or Λ hyperons from a resonance decay (dashed) for the carbon run. The latter are normalized to the same integral. (a) y-distribution for Λ hyperons, (b) p_t^2-distribution for Λ hyperons, (c) y-distribution for $\overline{\Lambda}$ hyperons and (d) p_t^2-distribution for $\overline{\Lambda}$ hyperons

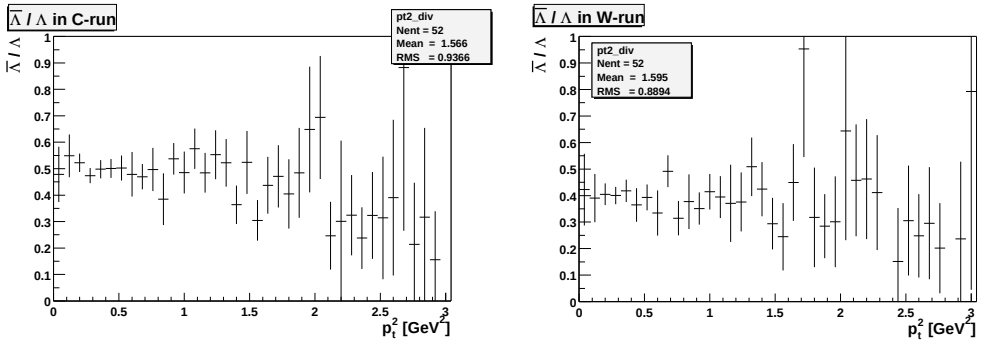

(a) (b)

Figure 5.23: The $\frac{\overline{\Lambda}}{\Lambda}$ p_t^2-distributions for the carbon (a) and the tungsten (b) run. The error bars include the statistical and the systematic errors (see text).

it can be concluded that the exclusion of the Σ^0 in the Monte Carlo should not affect the distributions and results.
By dividing the $\overline{\Lambda}$ p_t^2-distribution by that of the Λ, the p_t^2-distributions for $\frac{\overline{\Lambda}}{\Lambda}$ in Figure 5.23 for both runs are obtained. Only Λ hyperons in the Λ region were taken. The systematic error discussed in section 5.4.2 is included here already by adding it quadratically to the statistical error.

The Hyperon Ratio versus x_f and Extrapolation to $x_f = 0$

The distributions of $\frac{\overline{\Lambda}}{\Lambda}$ and $\frac{\overline{\Xi}}{\Xi}$ in x_f are obtained in the same way and shown in Figures 5.24 and 5.25 for both runs. Again the systematic error from Section 5.4.3 is included for $\frac{\overline{\Lambda}}{\Lambda}$. In [Kac97], already mentioned in Section 1.3.1, it is stated that these distributions should follow the functional form

$$\frac{\overline{\Lambda}}{\Lambda}(x_f) = \frac{k_{\overline{\Lambda}}(1-|x_f|)^{\beta_{\overline{\Lambda}}}}{k_\Lambda(1-|x_f|)^{\beta_\Lambda}} = k(1-|x_f|)^{\Delta\beta}, \tag{5.1}$$

since the thermal distribution in p_t^2 are assumed to be equal for particle and anti-particle below $p_t = 1$ GeV. This fit can be done either with fixed $\Delta\beta = \beta_{\overline{\Lambda}} - \beta_\Lambda$ given in [Kac97] (Fig. 5.25) or with $\Delta\beta$ as a free parameter (Fig. 5.24). The $\Delta\beta$ calculated from numbers in the paper are: $\Delta\beta_\Lambda = 7.27 \pm 0.14$ and $\Delta\beta_\Xi = 4.34 \pm 0.20$. The fitted values are $\Delta\beta = 7.3 \pm 1.5$ for the carbon run, the fit for the tungsten run gives $\Delta\beta = 5.4 \pm 1.2$. Within the large errors the two results are comparable and also consistent with the literature value. For the $\frac{\overline{\Xi}}{\Xi}$ distribution $\Delta\beta$ is fixed to the value $\Delta\beta_\Xi = 4.34$, since the statistics is so low that a free fit would make little sense.
The other fit parameter k is the value of the fit function at $x_f = 0$ and thus the desired extrapolation of the hyperon ratio to $x_f = 0$. In cases of low

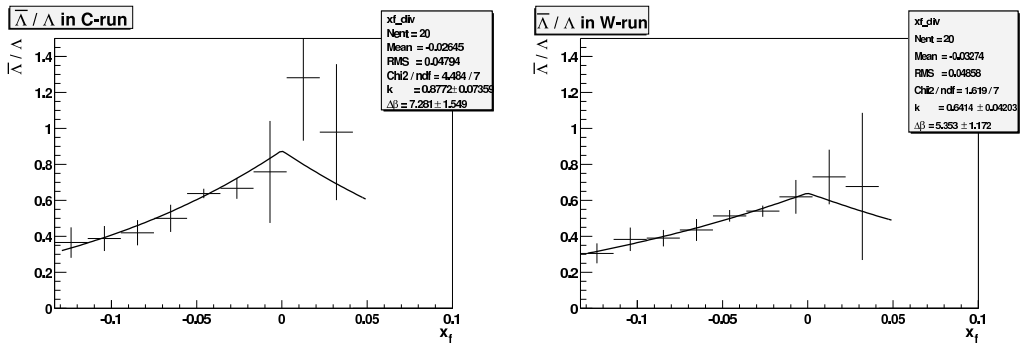

(a) (b)

Figure 5.24: The $\frac{\overline{\Lambda}}{\Lambda}$ x_f-distributions for the carbon (a) and the tungsten (b) run, formula 5.1 fitted to the distributions with free $\Delta\beta$.

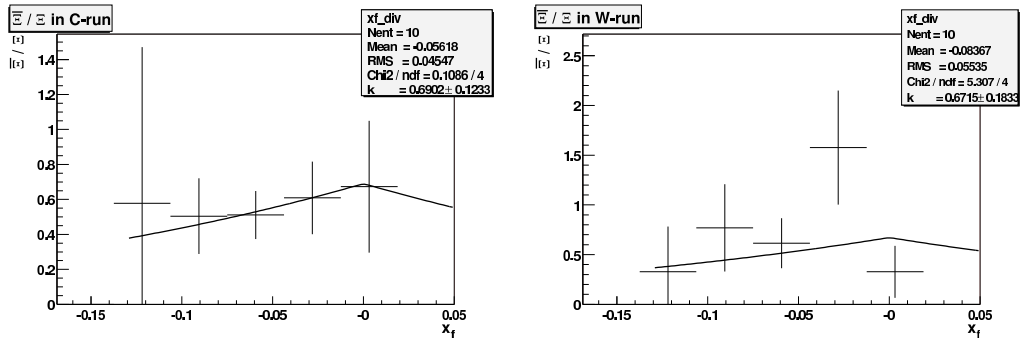

(a) (b)

Figure 5.25: The $\frac{\overline{\Xi}}{\Xi}$ x_f-distributions for the carbon (a) and the tungsten (b) run, formula 5.1 fitted to the distributions with $\Delta\beta$ set to 4.34 (value is taken from [Kac97]).

target mat.	ratio	value at $x_f = 0$	fit method
C	$\frac{\overline{\Lambda}}{\Lambda}$	0.88 ± 0.07	$\Delta\beta$ free
	$\frac{\overline{\Xi}}{\Xi}$	0.69 ± 0.12	$\Delta\beta$ fixed
	$\frac{\overline{\Omega}}{\Omega}$	1.7 ± 1.4	mean value
	$\frac{\Omega}{\Xi}$	0.05 ± 0.03	mean value
W	$\frac{\overline{\Lambda}}{\Lambda}$	0.64 ± 0.04	$\Delta\beta$ free
	$\frac{\overline{\Xi}}{\Xi}$	0.67 ± 0.18	$\Delta\beta$ fixed
	$\frac{\overline{\Omega}}{\Omega}$	1.7 ± 0.9	mean value
	$\frac{\Omega}{\Xi}$	0.29 ± 0.12	mean value

Table 5.6: Results of the extrapolation to $x_f = 0$. More information is given in the text.

ratio	$\Delta\beta$	$\langle x_f \rangle$	$\langle p_t \rangle$
$\frac{\overline{\Lambda}}{\Lambda}$	7.27 ± 0.14	-0.05	0.75
$\frac{\overline{\Xi}}{\Xi}$	4.34 ± 0.20	-0.05	0.85
$\frac{\overline{\Omega}}{\Omega}$	2.97 ± 0.21	-0.09	0.9
$\frac{\Omega}{\Xi}$	1.37 ± 0.21	-0.07	0.8
$\frac{\overline{\Omega}}{\overline{\Xi}}$	0.0 ± 0.2	-0.06	0.9

Table 5.7: The parameters used for the extrapolation to $x_f = 0$. $\Delta\beta$ is calculated from numbers given in [Kac97]. $\langle x_f \rangle$ and $\langle p_t \rangle$ are the averages of the means of the different distributions in the data.

statistics like $\frac{\overline{\Omega}}{\Omega}$ or $\frac{\Omega}{\Xi}$, the extrapolation can be done by estimating the mean value $\langle x_f \rangle$ of the distributions and by using the fit function 5.1 with the $\Delta\beta$ values given in [Kac97]. The extrapolation factor is then given by $\frac{1}{(1-|\langle x_f \rangle|)^{\Delta\beta}}$. The results are listed in table 5.6 together with the results from the fits. The errors are dominated by the statistical errors, the error on the extrapolation is negligible. The used parameters are listed in Table 5.7. The value of $\frac{\overline{\Omega}}{\Omega}$ does not have to be extrapolated in x_f, since for anti-particle to anti-particle ratio $\Delta\beta = 0$ holds [Kac97]. But for ratios of (anti-)hyperons with different strangeness content, also the p_t would have to be extrapolated to $p_t = 0$. Its estimated mean is therefore also stated in Table 5.7.

A different Way to extrapolate to the whole Phase Space

To be more independent of the Monte Carlo, a different method of extrapolation to the whole phase space is performed here. From [WA8903] we can take β values for neutron on carbon and copper. Interestingly enough, they are different, namely for carbon: $\beta_\Lambda = 1.80 \pm 0.02$, $\beta_{\overline{\Lambda}} = 8.46 \pm 0.09$ and for copper: $\beta_\Lambda = 2.23 \pm 0.02$, $\beta_{\overline{\Lambda}} = 8.18 \pm 0.09$. Using these values, we obtain for carbon $\Delta\beta = 6.66 \pm 0.09$ and for copper $\Delta\beta = 5.95 \pm 0.09$. Both values agree within errors with the fit results in Table 5.6 from figure 5.24 when comparing the tungsten with the copper target.
From the integral of $k(1-|x_f|)^\beta$ over x_f from -1 to 1, a value for the complete number of Λ hyperons and $\overline{\Lambda}$ hyperons can be obtained and thus a value for $\frac{\overline{\Lambda}}{\Lambda}$ integrated over the whole phase space.
The above mentioned integral is easy to calculate, it is

$$\int_{-1}^{1} k(1-|x|)^\beta dx = 2 \cdot \int_0^1 k(1-x)^\beta dx = \frac{2k}{\beta+1}. \tag{5.2}$$

This gives for the whole phase space:

$$\frac{\overline{\Lambda}}{\Lambda} = \frac{\frac{2k_{\overline{\Lambda}}}{\beta_{\overline{\Lambda}}+1}}{\frac{2k_\Lambda}{\beta_\Lambda+1}} = \frac{k_{\overline{\Lambda}}}{k_\Lambda}\frac{\beta_\Lambda+1}{\beta_{\overline{\Lambda}}+1} = k\frac{\beta_\Lambda+1}{\beta_{\overline{\Lambda}}+1} \tag{5.3}$$

where k is the fit parameter in from figure 5.24. Using this fit parameter for the carbon run and the above mentioned β values from the paper for carbon, we now calculate for the whole phase space in the carbon run: $\frac{\overline{\Lambda}}{\Lambda} = 0.26 \pm 0.02$ where the errors are obtained by Gaussian error propagation.
For tungsten, no β values could be found in the literature. By comparing the β values from [WA8903] with the values in [Kac97]: $\beta_\Lambda = 0.581 \pm 0.003$ and $\beta_{\overline{\Lambda}} = 7.85 \pm 0.14$, we see that the $\beta_{\overline{\Lambda}}$ does not seem to change much with the target material. Thus setting $\beta_\Lambda = \beta_{\overline{\Lambda}} - \Delta\beta$, and using $\Delta\beta$ from the fit and for $\beta_{\overline{\Lambda}}$ the value for copper, we obtain for the whole phase space in the tungsten run $\frac{\overline{\Lambda}}{\Lambda} = 0.27 \pm 0.09$.

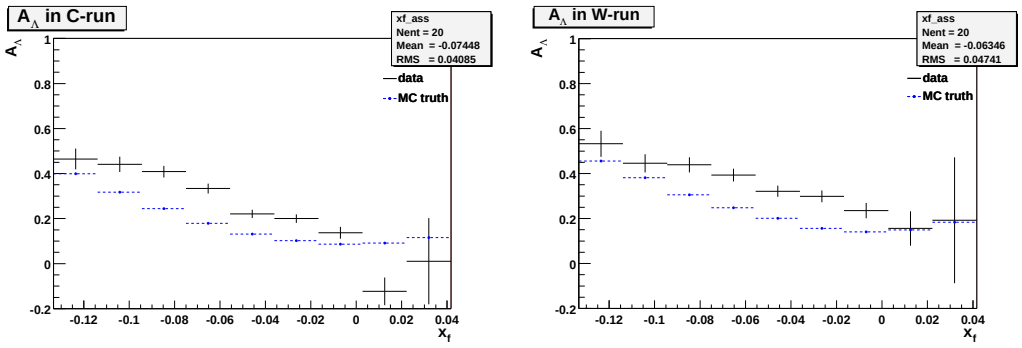

(a) (b)

Figure 5.26: The Λ particle–anti-particle asymmetry $A_\Lambda(x_f)$ for the carbon (a) and tungsten (b) run. Dashed, the Monte Carlo truth prediction is plotted.

5.3.3 Particle–anti-Particle Asymmetries

The particle–anti-particle asymmetry in x_f as defined in Equation 1.13 have been plotted in Figure 5.26 for Λ hyperons for both runs, including the Monte Carlo truth prediction. This was done straight forward using the acceptance corrected x_f-distributions.

5.4 Systematic Errors

As the statistical uncertainties for the Ξ hyperons and Ω hyperons are large, the discussion of the systematic errors will be restricted to $\frac{\overline{\Lambda}}{\Lambda}$. An examination of the systematic error on the Λ asymmetry is missing, but could be done by the same method used later for the p_t^2- and x_f-distributions of $\frac{\overline{\Lambda}}{\Lambda}$. As mentioned above, the two effects that distort measurements are detector inefficiencies and finite resolution of the measured values as position or momenta. While the first effect is present in every measurement, the second one affects only distributions. Thus this section will describe first a way to determine the overall systematic uncertainty, including also other possible effects than the acceptance corrections, then the systematic uncertainties in the p_t^2- and x_f-distributions will be discussed for $\frac{\overline{\Lambda}}{\Lambda}$.

5.4.1 Integral Errors

The Error from the Acceptance Corrections

As seen in Section 5.2.1, the azimuthal distributions of the Λ hyperons in the Monte Carlo deviate from that of the real data, while the $\overline{\Lambda}$ ϕ-distributions

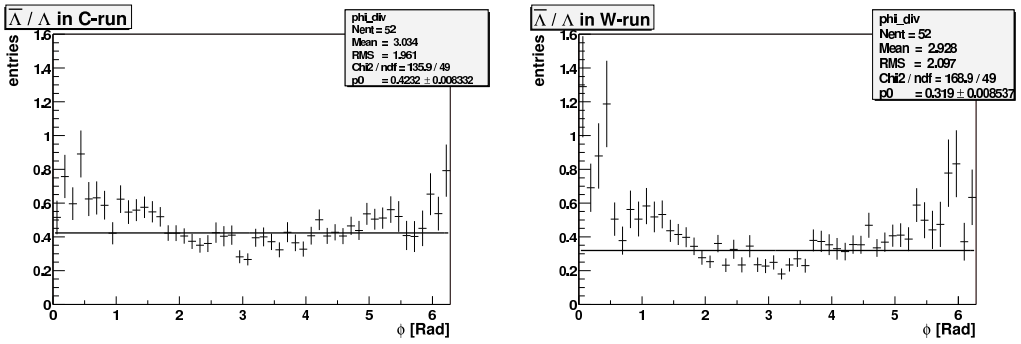

(a) (b)

Figure 5.27: The acceptance corrected ϕ-distribution for $\frac{\overline{\Lambda}}{\Lambda}$ for the carbon (a) and the tungsten (b) run in the region 0.1 GeV $< p_t <$ 2.5 GeV and $-2 < y < 0.5$. A constant was fitted to the distributions.

do not. This of course leads to a non flat distribution of $\frac{\overline{\Lambda}}{\Lambda}$ in ϕ after the acceptance correction as seen in Figure 5.27 for both runs. Since this is by no means understandable from the physics point of view, it must be an artefact of the acceptance correction. By using this deviation, the systematic error can be estimated using the following method.
The fits of a constant in Figure 5.27 are done by the χ^2 method which is described *e.g.* in [Cow98]. The way the χ^2 method works is that the so called χ^2 function, which is just a measure for the quality of the fit, is minimized. For uncorrelated measurements, which we have in this case, the χ^2 function has the following form:

$$\chi^2 = \sum_i \frac{(x_i - \bar{x}_i)^2}{\sigma_i^2} \tag{5.4}$$

where the x_i stand for the measured values, $\bar{x}_i$ for the values of the fit function at that point and σ_i for the uncertainty of the data point. Obviously, the value of the χ^2 function at the calculated minimum is a measure for the quality of the fit, or more precise, it should be

$$\langle \chi^2_{min} \rangle = n_{dof} \quad \Rightarrow \quad \frac{\chi^2_{min}}{n_{dof}} \approx 1. \tag{5.5}$$

for a good fit. Here n_{dof} is the number of degrees of freedom, which is the number of fitted data points minus the number of parameters in the fit. In our case, we have 50 data points in the histogram and one parameter in the fit, namely the constant "p0", so we get $n_{dof} = 50 - 1 = 49$. From the histograms, we read $\frac{\chi^2_{min}}{n_{dof}} = 135.9/49$ for the carbon run and $\frac{\chi^2_{min}}{n_{dof}} = 168.9/49$ for the tungsten run, both numbers are larger than one, indicating that the data cannot be described by a constant as they should.

The question is now how much larger the errors must be, for the χ^2 to satisfy Equation 5.5. We introduce a factor a and each single error of each data point is multiplied by that factor, giving

$$\chi^2_{new} = \sum_i \frac{(x_i - \bar{x}_i)^2}{a^2\sigma_i^2} = \frac{1}{a^2}\sum_i \frac{(x_i - \bar{x}_i)^2}{\sigma_i^2}$$

and thus, to satisfy Equation 5.5, $a = \sqrt{\frac{\chi^2_{min}}{n_{dof}}}$ from the fit. Therefore we have $a = \sqrt{135.9/49} = 1.6$ for the carbon run and $a = \sqrt{168.9/49} = 1.9$ for the tungsten run, meaning that the statistical errors of $\frac{\overline{\Lambda}}{\Lambda}$ in the Λ region in the carbon (tungsten) run have to be multiplied by the factor 1.6 (1.9) to get the overall error, including statistical and systematic error. Since these errors are both 0.009 as seen in table 5.3, the corresponding systematic error in the carbon run is

$$\sigma_{syst} = \sqrt{(1.6^2 - 1)\sigma^2_{stat}} = 1.2\sigma_{stat} = 0.011. \tag{5.6}$$

For the tungsten run this gives $\sigma_{syst} = 0.015$. These numbers correspond to relative errors of $\sigma_{syst,C} = 2.3\%$ for carbon and $\sigma_{syst,W} = 3.6\%$ for the tungsten run. If we assume that this relative systematic error is of the same order of magnitude for all kinds of hyperon ratios, it is justified to neglect this error except for $\frac{\overline{\Lambda}}{\Lambda}$ if we compare it to the statistical errors in the Tables 5.2 and 5.3.
The method described above assumes uncorrelated systematic errors for the individual bins. Therefore the bin size should roughly match the angular coverage of individual detector elements. Looking at the fluctuations around a common mean, Figure 5.27 suggests that the chosen binning is in fact too narrow in certain regions. Nevertheless, since part of the effect is expected to average out when integrating over the azimuth, the systematic errors are considered to be realistic estimates for the uncertainties of the global detector acceptance.

The Error from the Trigger

As mentioned in Section 3.3.4, the trigger used in the runs analyzed in this work was an interaction trigger, requiring a certain hit multiplicity in the RICH. In case Λ events would have a different multiplicity than $\overline{\Lambda}$ events, the interaction trigger would introduce a bias. To examine the dependence of the value $\frac{\overline{\Lambda}}{\Lambda}$ on the multiplicity, different cuts on the number of tracks coming from the primary vertex are applied and the acceptance corrected value $\frac{\overline{\Lambda}}{\Lambda}$ for the tungsten run has been calculated exactly the same way as in Section 5.3.1. The result is shown in Table 5.8. No dependence on the multiplicity is observed.

cut on # tracks	$\frac{\overline{\Lambda}}{\Lambda}$
> 1	0.198 ± 0.005
> 3	0.197
> 5	0.195
> 7	0.196
> 9	0.197

Table 5.8: For the carbon run, the acceptance corrected value $\frac{\overline{\Lambda}}{\Lambda}$ with a cut on the multiplicity.

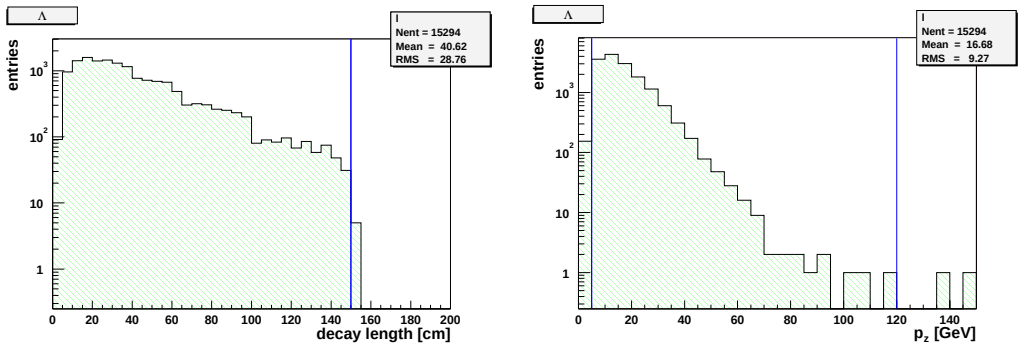

(a) (b)

Figure 5.28: The decay length (a) and p_z-distribution (b) for Λ candidates after all cuts in the peak region for the carbon run. The lines indicate the cuts applied on the Monte Carlo level.

Error from the Monte Carlo Cut on $p_z > 5$ GeV

As stated in Section 5.1.2, to save disk space, at the Monte Carlo generation level only Λ hyperons with 5 GeV $< p_z <$ 120 GeV and decay length $<$ 150 cm were injected into the detector simulation. The distributions in p_z and decay length of the Λ candidates for the real data carbon run are shown in Figure 5.28. As seen in Figure 5.28(b), the cut on $p_z <$ 5GeV is not completely uncritical, since about 1% of the content of the histogram is below 5 GeV. To be sure that this does not affect the results on $\frac{\overline{\Lambda}}{\Lambda}$, the momentum spectrum was plotted with background correction for Λ and $\overline{\Lambda}$ for both the carbon and the tungsten run. The results, *i.e.* the number of entries in the first bin, corresponding to $p_z = 0$ to 5 GeV, are listed in Table 5.9. From these numbers, we obtain a deviation on $\frac{\overline{\Lambda}}{\Lambda}$ of about 0.5%. Since the minimal error on $\frac{\overline{\Lambda}}{\Lambda}$, obtained for the carbon run with no restriction on p_t and y (see section 5.3.1), is about 1.8% statistical and 2.3% systematic,

particle	run	entries	1^{st} bin	ratio
Λ	C	14726	142	0.010
$\overline{\Lambda}$	C	7323	37	0.005
Λ	W	9031	91	0.010
$\overline{\Lambda}$	W	3646	19	0.005

Table 5.9: The contents of the histograms where p_z is plotted for $\Lambda/\overline{\Lambda}$ candidates after all cuts after background correction. The bin size is 5 GeV, thus the first bin contains all entries at $0-5$ GeV. The last column gives the number of entries in the first bin divided by the number of all entries.

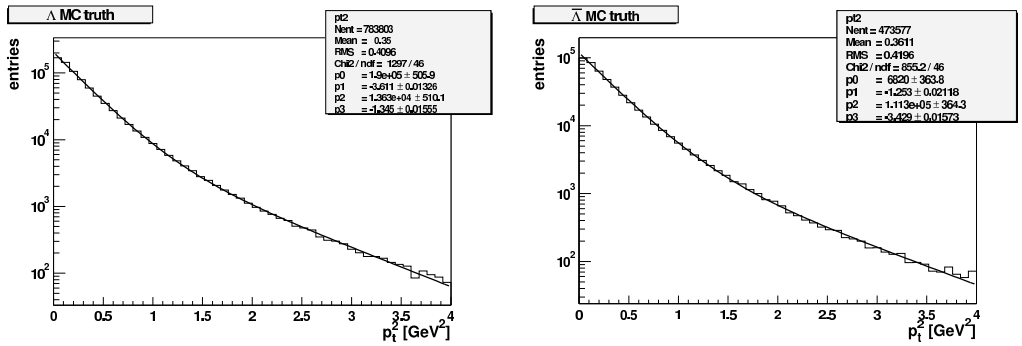

(a) (b)

Figure 5.29: The Monte Carlo truth p_t^2-distribution for Λ (a) and $\overline{\Lambda}$ (b) in the carbon run, fitted to the sum of two exponential functions: $p0 \cdot \exp(p1 \cdot x) + p2 \cdot \exp(p3 \cdot x)$.

this contribution to the overall error can be neglected.
On the other hand for the distributions in x_f and y, since $p_z < 5$ GeV corresponds to $x_f < -0.125$ and $y < -1.58$, acceptance corrected values in this range are not reliable, and therefore not shown.

5.4.2 The Error in the p_t^2-Distribution

To estimate the systematic uncertainties in the p_t^2-, as well as in the x_f-distribution of $\frac{\overline{\Lambda}}{\Lambda}$, a toy Monte Carlo method was used. The way this toy Monte Carlo program works is that it generates numbers for the p_t^2 of a particle such that the distribution follows a sum of two exponential functions with parameters obtained by the fit to the ("real", not toy) Monte Carlo truth distribution shown in Figure 5.29. The method used for the production of these distributions was the acceptance–rejection method, a short description can be found *e.g.* in [Cow98]. This distribution is our toy Monte Carlo truth.

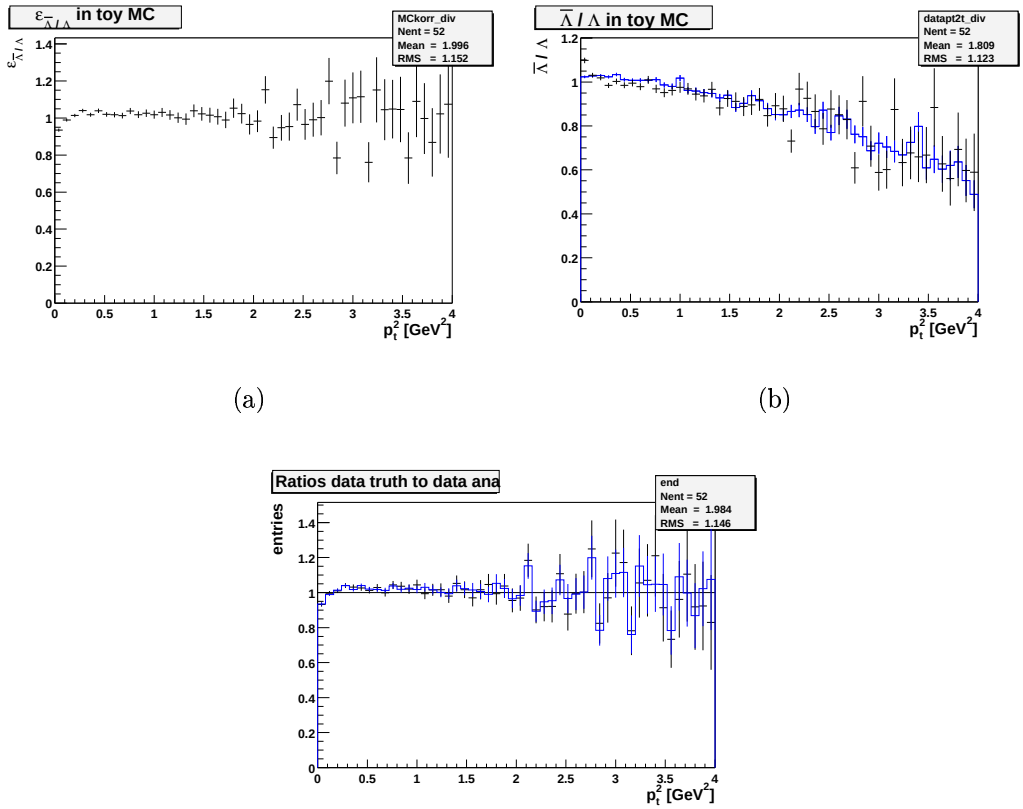

(a) (b)

(c)

Figure 5.30: Results of the toy Monte Carlo for p_t^2. (a) acceptance for the $\frac{\overline{\Lambda}}{\Lambda}$ ratio, (b) the toy data $\frac{\overline{\Lambda}}{\Lambda}$-distribution as it was generated (histogram) in comparison to the corrected toy data (crosses) and (c) the Monte Carlo "toy data" $\frac{\overline{\Lambda}}{\Lambda}$-distribution as it was generated divided by the corrected toy data, *i.e.* the deviation of the corrected toy data from the originally produced toy data (crosses). Also shown in (c) is the acceptance for $\frac{\overline{\Lambda}}{\Lambda}$ (histogram)

	parameter	Λ	$\overline{\Lambda}$
MC truth	c_1	1	16
	s_1	-3.6	-3.4
	c_2	15	1
	s_2	-1.3	-1.3
data	c_1	5	3
	s_1	-2.5	-2.5
	c_2	1.5	1
	s_2	-1.2	-1.35

Table 5.10: Listed are the parameters of the function $c_1 \cdot \exp(s_1 \cdot p_t^2) + c_2 \cdot \exp(s_2 \cdot p_t^2)$ with which the distributions of the toy Monte Carlo truth and the original toy data were produced.

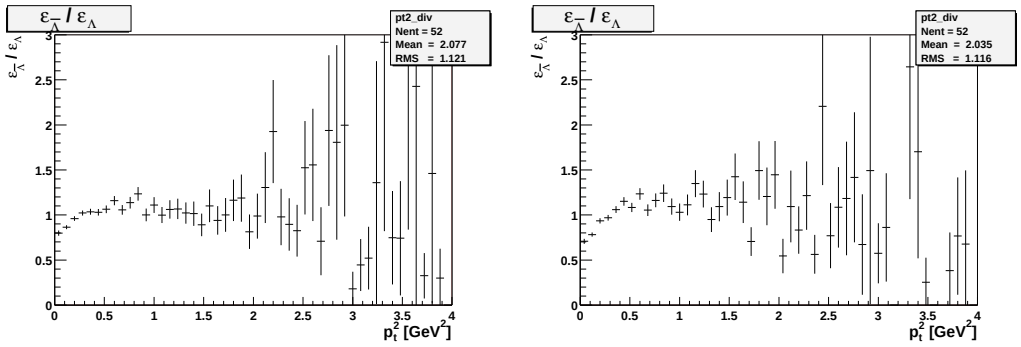

(a) (b)

Figure 5.31: The acceptances of $\frac{\overline{\Lambda}}{\Lambda}$ in the carbon (a) and the tungsten (b) run in the range 0.1 GeV $< p_t <$ 2.5 GeV and $-2 < y < 0.5$.

It is folded with a Gaussian distribution to give the toy Monte Carlo after the digitization and reconstruction. The ratio of the two gives the acceptance correction for the toy Monte Carlo.
Then a second p_t^2 distribution is generated following the same functional form, but this time using the parameters from the real acceptance corrected data shown in Figures 5.18 to 5.21 for the carbon run. This defines the toy Monte Carlo "real data", also called toy data from now on. These numbers again are smeared with a Gaussian distribution and then give the toy data after reconstruction. The latter is then corrected using the acceptance correction from the toy Monte Carlo described above. If everything is perfect, the corrected distribution should be the same as the original function with which the toy data were produced. Every deviation from that is a measure for the systematic error.
A resolution of $\sigma_{p_t^2} = 0.08$ GeV^2 was used for the toy Monte Carlo. For the toy data a 40% larger smearing was used, which is the factor that the mass peaks are wider in the real data than in the Monte Carlo. The parameters of these distributions are listed in Table 5.10, they are chosen to be close to the values of the fits in Figures 5.29 and 5.18 mentioned above. The results are shown in Figure 5.30: the acceptance for the $\frac{\overline{\Lambda}}{\Lambda}$, the toy data $\frac{\overline{\Lambda}}{\Lambda}$-distribution as it was generated in comparison to the corrected toy data. Also shown in Figure 5.30(c) is the toy data $\frac{\overline{\Lambda}}{\Lambda}$-distribution as it was generated divided by the corrected toy data, in comparison to the acceptance for $\frac{\overline{\Lambda}}{\Lambda}$. The first two distributions in the figure match qualitatively the real data in Figure 5.31 and 5.23, supporting that the parameters and the method are reasonable. As can be seen in Figure 5.30(c), the correction factors and the deviation of the corrected distribution from the input almost coincide. Even when the parameters were changed strongly the distributions matched at least roughly. The point is that the parameters for the Λ and $\overline{\Lambda}$ distributions in the real data do not differ so much, yielding in a correct result *even without an acceptance correction*. It looks like the acceptance correction, calculated from pretty different parameters for the distributions, worsen the result, leading to a systematic error being as large as the acceptance correction.
Thus the acceptance on $\frac{\overline{\Lambda}}{\Lambda}$ itself is a measure for the systematic error, or more precisely its deviation from unity in each p_t^2 bin. The acceptance correction for $\frac{\overline{\Lambda}}{\Lambda}$ is nothing but the ratio of the acceptance corrections of $\overline{\Lambda}$ and Λ $\frac{\varepsilon_{\overline{\Lambda}}}{\varepsilon_{\Lambda}}$. Therefore we obtain for the relative error $\frac{\sigma_{p_t^2,syst}}{\frac{\overline{\Lambda}}{\Lambda}(p_t^2)} = |1 - \frac{\varepsilon_{\overline{\Lambda}}}{\varepsilon_{\Lambda}}|$ for each bin in p_t^2.

5.4.3 The Error in the x_f-Distribution

The method to estimate the systematic error on the x_f-distribution of $\frac{\overline{\Lambda}}{\Lambda}$ is the same as for the p_t^2 distribution, but there are some problems to solve.

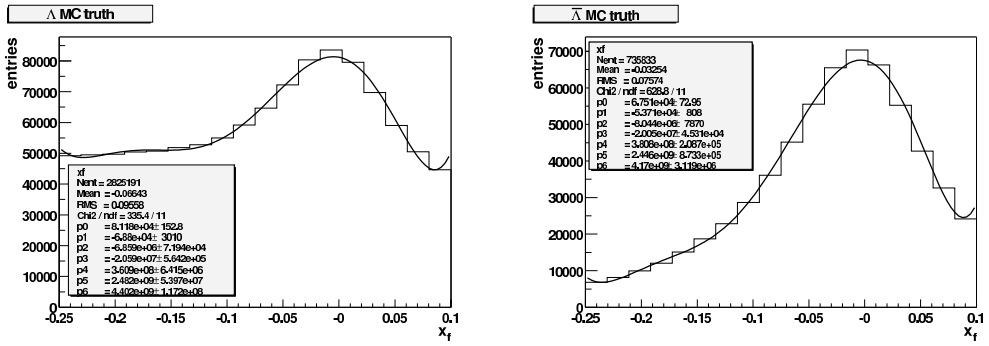

(a) (b)

Figure 5.32: Sixth order polynomials fitted to the Monte Carlo truth in x_f in the carbon run, done for Λ (a) and $\overline{\Lambda}$ (b).

First, the function which was fitted to the data in Figure 5.24 cannot be fitted to the Monte Carlo truth data. Therefore a polynomial of sixth order was used as seen in Figure 5.32. The toy Monte Carlo truth is generated following these functions. The toy data on the other hand is produced according to the function $(1-|x_f|)^\beta$. Now the same procedure starts as for the p_t^2-distribution, but this time the parameters β in the data distributions were chosen in a way that the distributions of the corrected $\frac{\overline{\Lambda}}{\Lambda}$ (see Fig. 5.33(b) and 5.33(c) for both toy Monte Carlo runs) yield about the same fit parameter $\Delta\beta$ as the real data in Figure 5.24. This was for the carbon run at $\beta_\Lambda = 3$, $\beta_{\overline{\Lambda}} = 14$ and for the tungsten run at $\beta_\Lambda = 6$, $\beta_{\overline{\Lambda}} = 13$. The smearing was chosen in a way that the acceptances $\frac{\varepsilon_{\overline{\Lambda}}}{\varepsilon_\Lambda}$ (the histogram in Fig. 5.33(d)) look roughly as the ones in the "real" Monte Carlo in Figure 5.34. The corresponding value is $\sigma_{x_f} = 0.04$ for the toy Monte Carlo and 1.4 times that value for the toy data, as above.

The resulting deviations of the corrected values of $\frac{\overline{\Lambda}}{\Lambda}$ from the originally produced distribution are shown as the crosses in Figures 5.33(d) and 5.33(e). From the acceptance, shown as the histogram in Figure 5.33(d), it is obvious that the case is very different from the p_t^2 distributions where these distributions coincide. In this case the acceptance correction really corrects the distribution. The distributions do not change drastically, if the parameters are changed slightly and thus are assumed to be a rough estimate for the real systematic error, although the match between the real data and Monte Carlo is not very good. These histograms were used to calculate the systematic errors as the deviations from unity in these histograms for each x_f bin, *i.e.* the relative error is $\frac{\sigma_{x_f,syst}}{\frac{\overline{\Lambda}}{\Lambda}(x_f)} = |1 - \text{bin content}|$.

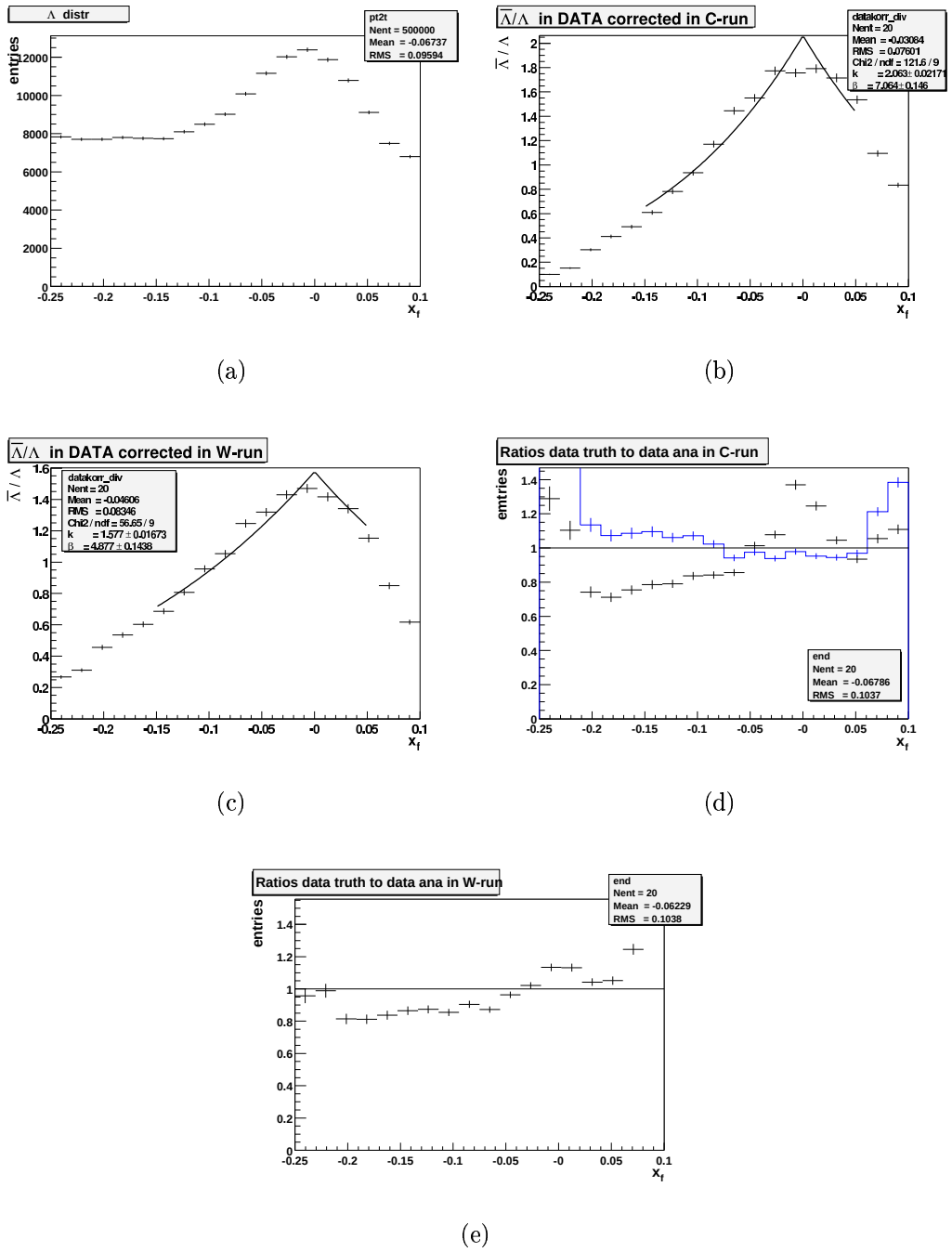

Figure 5.33: Toy Monte Carlo results for x_f. (a) Monte Carlo truth for Λ in the carbon run. (b) Ratio $\frac{\overline{\Lambda}}{\Lambda}$ corrected toy data in the carbon and (c) the tungsten run. (d) Acceptance for $\frac{\overline{\Lambda}}{\Lambda}$ (histogram) and toy data as generated divided by toy data after correction for the carbon (crosses) and (e) the tungsten run.

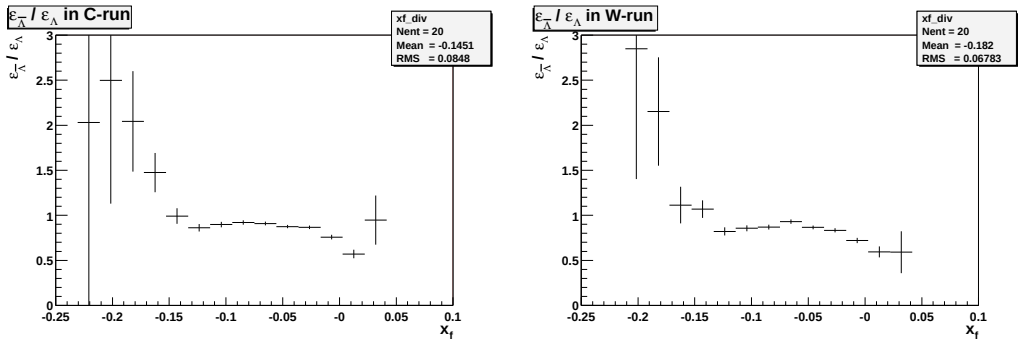

(a) (b)

Figure 5.34: The x_f-distribution in the Monte Carlo data of the $\frac{\overline{\Lambda}}{\Lambda}$ acceptance for the carbon (a) and tungsten run (b).

Chapter 6

Results, Discussion and Outlook

In this chapter, the results will be summarized, compared to those of other experiments and discussed. It will close with the conclusion after a short outlook.

6.1 Results and their Discussion

6.1.1 Results on Hyperon Ratios

The integrated Hyperon Ratios

The results on hyperon ratios in different kinematic regions are listed in the Tables 5.3, 5.4 and 5.5. The numbers from the last two tables are graphically presented in Figure 6.1. If we include the systematic error from Section 5.4.1, we determine for the different regions for $\frac{\overline{\Lambda}}{\Lambda}$ the values and errors listed in Table 6.1. From these tables, we see that the Monte Carlo cannot predict these values quantitatively, but it can do so qualitatively, even for the differences between the two targets.
The most interesting thing is that the values for $\frac{\overline{\Lambda}}{\Lambda}$ for the two runs in the Λ as well as in the Ξ region deviate with more than three standard deviations from each other.
The hyperon ratios, which are extrapolated to the whole phase space, are listed in Table 5.2 and, including the systematic errors, in table 6.1. The two extrapolation methods — the one using the Monte Carlo as in Section 5.3.1 and the other using the Formula 5.3 as done in Section 5.3.2 — agree within errors on the value for $\frac{\overline{\Lambda}}{\Lambda}$ in the carbon run, but the agreement is not very good. Especially they both give the same numbers for the two target materials, although the number for the x_f extrapolation of the tungsten run has a large error. This is due to the fact that the β parameters for tungsten were not known. None the less this indicates that indeed it is well possible

region	run	value	MC truth
Λ	C	$0.477 \pm 0.009 \pm 0.011$	0.604
Λ	W	$0.390 \pm 0.009 \pm 0.014$	0.519
Ξ	C	$0.576 \pm 0.011 \pm 0.013$	0.733
Ξ	W	$0.474 \pm 0.011 \pm 0.017$	0.638
whole by MC	C	$0.204 \pm 0.004 \pm 0.005$	0.259
whole by MC	W	$0.198 \pm 0.005 \pm 0.007$	0.262
whole by x_f	C	$0.26 \pm 0.02 \pm 0.01$	0.259
whole by x_f	W	$0.27 \pm 0.09 \pm 0.01$	0.262

Table 6.1: Final results on $\frac{\overline{\Lambda}}{\Lambda}$ in the different regions and extrapolated to the whole phase space. Where "whole by MC" means extrapolated to the whole phase space using the Monte Carlo (see Section 5.3.1) and "whole by x_f" means using the x_f extrapolation (see Section 5.3.2). The last column gives the Monte Carlo truth prediction. The regions are: Λ: 0.1 GeV $< p_t <$ 2.5 GeV and $-2.0 < y < 0.5$, Ξ: 0.1 GeV $< p_t <$ 2.0 GeV and $-1.5 < y < 0.5$. The first error is the statistical error, the second one is the systematic uncertainty.

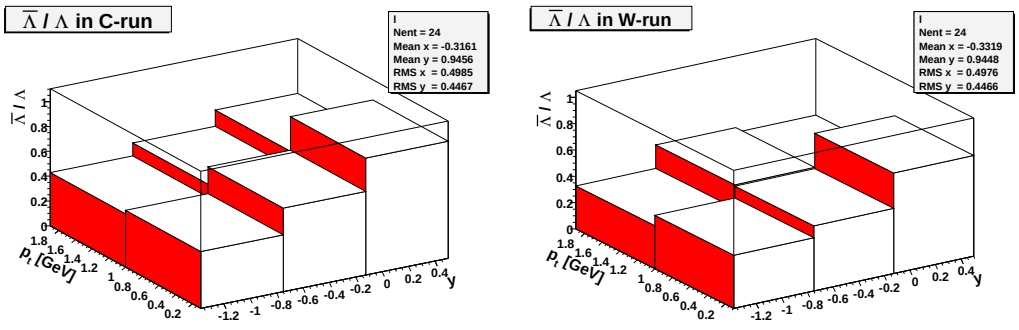

(a) (b)

Figure 6.1: Distribution of $\frac{\overline{\Lambda}}{\Lambda}$ in p_t versus y for the carbon (a) and the tungsten (b) run. The numbers used for these plots are taken from Tables 5.4 and 5.5.

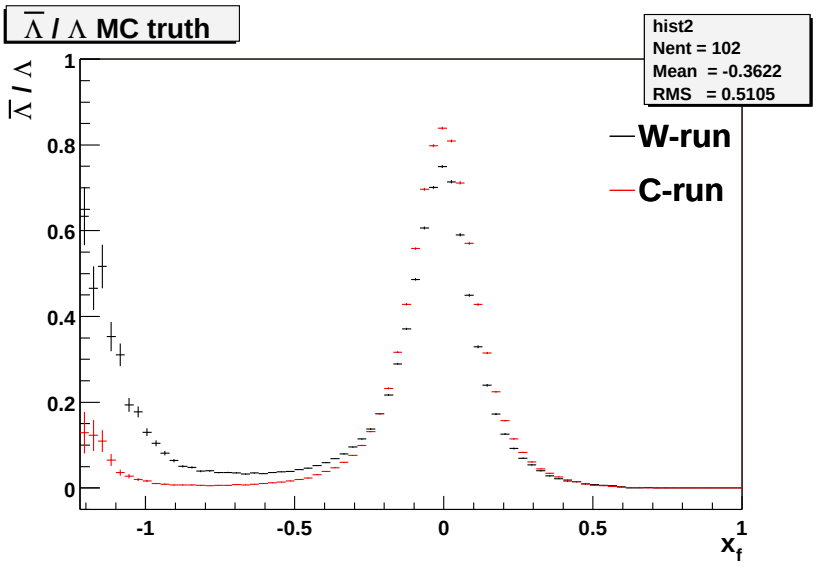

(a)

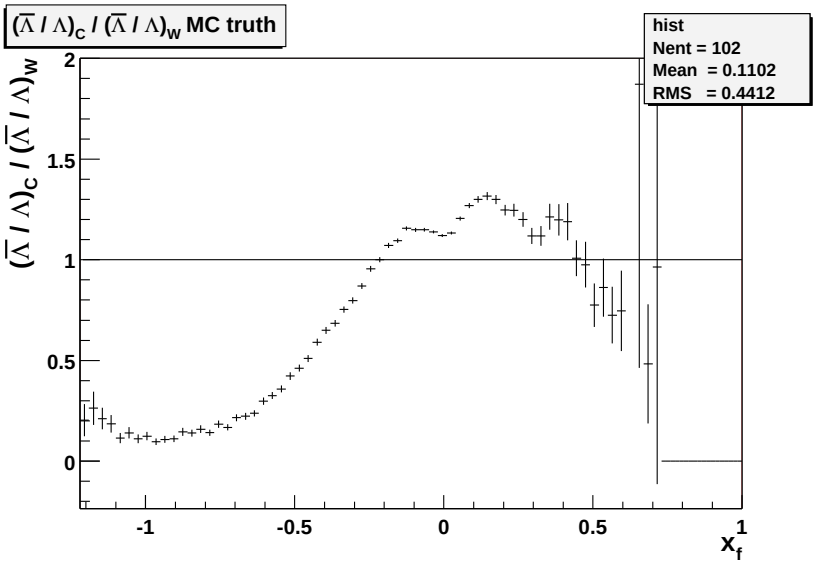

(b)

Figure 6.2: Monte Carlo truth: Distribution of $\frac{\overline{\Lambda}}{\Lambda}$ in x_f for the carbon (a, black) and the tungsten (a, red or grey) run. In (b) the ratio of these $(\frac{\overline{\Lambda}}{\Lambda})_C/(\frac{\overline{\Lambda}}{\Lambda})_W$ is plotted.

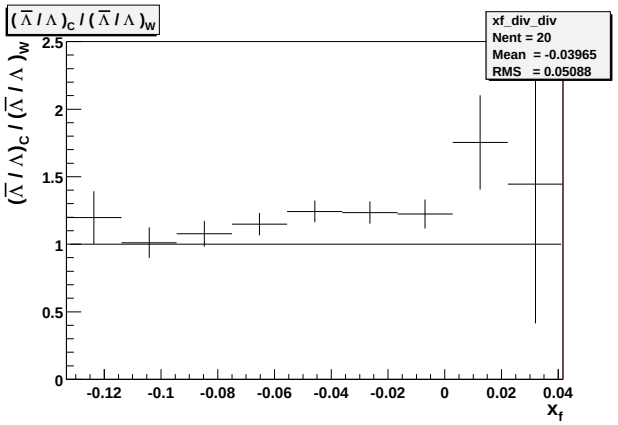

Figure 6.3: The ratio $\frac{\overline{\Lambda}}{\Lambda}$ in the carbon run divided by $\frac{\overline{\Lambda}}{\Lambda}$ for the tungsten run in the data.

that the numbers are the same for both materials.
If one believes the arguments that $\frac{\overline{\Lambda}}{\Lambda}$ ratios for the whole phase space do not depend on the target material, obviously, the β parameters have to be material dependent. This is for β_Λ already seen by comparing the number for carbon and copper from [WA8903] and the numbers from [Kac97] as stated in Section 5.3.2. In Figure 6.2, the Monte Carlo truth values for $\frac{\overline{\Lambda}}{\Lambda}$ in the carbon and the tungsten run plotted against x_f are shown together with the ratio of the two. In Figure 6.3 the same ratio is plotted for the acceptance and background corrected data. The ratio is about the same around $x_f = 0$ for the data and the Monte Carlo truth, and it is one in about the same range of x_f. Thus it is safe to say that the Monte Carlo describes this ratio qualitatively correct making it more plausible that its prediction, that the ratio $\frac{\overline{\Lambda}}{\Lambda}$ for the whole phase space is equal for both materials, is correct.
But what can be the reason for such a behavior? The first thing that strikes the eye when looking at Figure 6.2 is that the distributions spread into the kinematically forbidden range of $x_f < -1$. Since this range is only kinematically forbidden, if a single nucleon–nucleon interaction is assumed, this must be a nuclear effect. This effect is known from hadron nucleus interactions at a few GeV and is sometimes called the cumulative effect [Bal75]. It was first discovered for mesons, and is now also known for baryons, *e.g.* the Λ [Tom94]. There are different explanations, one is that the beam particle does not interact with a single nucleon, but simultaneously with a group of nucleons [Bal75]. This cannot be the case for the Monte Carlo, since FRITIOF, as described earlier in Section 5.1.1, considers incoherent multiple scatterings with single nucleons only [Pi92]. A different kind of explanation is that given in [Gor77]. Here the beam particle is subject to multiple scattering and looses velocity (and possibly gains mass) in the first interaction. Therefore the produced particles of the second interaction can appear more backwards than is allowed by a single interaction.

run	a	b	ratio	value	exp.
C	0.451	0.555	$\frac{\overline{\Lambda}}{\Lambda}$	0.18	0.204
			$\frac{\overline{\Xi}}{\Xi}$	0.63	0.39
			$\frac{\overline{\Omega}}{\Omega}$	1.5	1.2
			$\frac{\Xi}{\Lambda}$	0.086	0.040
			$\frac{\overline{\Xi}}{\Lambda}$	0.30	0.078
			$\frac{\Omega}{\Xi}$	0.34	0.029
			$\frac{\overline{\Omega}}{\overline{\Xi}}$	0.81	0.10
W	0.471	0.561	$\frac{\overline{\Lambda}}{\Lambda}$	0.19	0.198
			$\frac{\overline{\Xi}}{\Xi}$	0.65	0.64
			$\frac{\overline{\Omega}}{\Omega}$	1.6	1.4
			$\frac{\Xi}{\Lambda}$	0.085	0.034
			$\frac{\overline{\Xi}}{\Lambda}$	0.35	0.11
			$\frac{\Omega}{\Xi}$	0.37	0.18
			$\frac{\overline{\Omega}}{\overline{\Xi}}$	0.83	0.40

Table 6.2: The results of the simple model trying to find optimal parameters a and b for the data in the carbon and tungsten run. The last column gives the values for the corresponding run, as listed in Table 5.2. The four first rows for each run corresponds to the four ratios used for optimization, the other ratios do not depend so much on a and b.

In the context of this explanation, it is possible to understand, why the x_f-distributions of the hyperon ratios should be different for different target materials. Due to the changed Lorentz transformation in multiple scatterings, any distribution in x_f should smear out with rising nuclear mass number of the target, since the multiple scattering becomes more probable. This can explain qualitatively the Monte Carlo distributions in Figure 6.2 as well as the broadening of the x_f-distribution of $\frac{\overline{\Lambda}}{\Lambda}$ for the tungsten run compared to that of the carbon run (see Fig. 5.24 and 6.3).

The predictions of the simple Model

The model presented in Chapter 2 yielded qualitatively good results for the hyperon ratios $\frac{\overline{\Lambda}}{\Lambda}$, $\frac{\overline{\Xi}}{\Xi}$, $\frac{\Xi}{\Lambda}$ and $\frac{\overline{\Xi}}{\Lambda}$ for the WA85 results. Now the parameters a and b can be optimized *e.g.* for the results on $\frac{\overline{\Lambda}}{\Lambda}$, $\frac{\overline{\Xi}}{\Xi}$, $\frac{\Xi}{\Lambda}$ and $\frac{\overline{\Omega}}{\Omega}$ for the whole phase space in the carbon and tungsten run of this thesis. A global minimum was again found for both runs and it looked similar to the minimum for the WA85 data. The best solutions found are given in Table 6.2 with the

target	particle	slope1	slope2	slope2 in [WA8903]
C	Λ	-1.2 ± 0.1	-2.5 ± 0.2	-2.38 ± 0.01
C	$\overline{\Lambda}$	-1.4 ± 0.4	-2.6 ± 0.6	-3.22 ± 0.03
W	Λ	-0.1 ± 0.9	-1.68 ± 0.07	—
W	$\overline{\Lambda}$	-1.5 ± 0.3	-2.4 ± 1.4	—

Table 6.3: Λ fit results for p_t^2 compared to results from neutron–carbon collisions at about 260 GeV beam energy.

corresponding values from the experiment taken from Table 5.2. It seems that the model predicts the tungsten values much better and has especially problems to get the ratios of hyperons with different strangeness right. The parameters a and b are similar for all three cases (in the WA85 case it was $a = 0.447$ and $b = 0.536$) and so are the hyperon ratios. Again a and b are close to 0.5, indicating almost equal probabilities to build a hadron from sea and constituent quarks and the production of baryons to mesons.
The ratios anti-hyperon to hyperon and $\frac{\Xi}{\Lambda}$ are qualitatively right. This is astonishing, since the model neglects almost all kinematics and two important processes, namely the leading twist and the leading particle effect including hadronization. We have to conclude that combinatorics is the main part to explain the hyperon ratios.

The Differential Hyperon Ratios and extrapolation to $x_f = 0$

The Λ and $\overline{\Lambda}$ distributions in p_t^2 were shown in Figures 5.18 to 5.21 for both runs. The sum of two exponential functions $c1 \cdot \exp(slope1 \cdot p_t^2) + c2 \cdot \exp(slope2 \cdot p_t^2)$ were fitted to them. The fit results are listed in Table 6.3 together with corresponding values from neutron beam on carbon interactions at around 260 GeV [WA8903]. Except for the Λ fit results for tungsten, the slope parameters from HERA-B all agree with each other within errors. The slope2 parameters in the carbon run agree within errors with the corresponding values from [WA8903]. In the WA89 experiment, a flattening of the Λ and $\overline{\Lambda}$ p_t^2 spectrum above ~ 1.1 GeV is seen also.
The p_t^2 distribution of $\frac{\overline{\Lambda}}{\Lambda}$ is shown in Figure 5.23 and is flat between 0 GeV^2 and 1 GeV^2 as expected, since equal thermal distributions for particle and anti-particle were assumed for the extrapolation Formula 5.1.
When fitting the x_f-distribution of $\frac{\overline{\Lambda}}{\Lambda}$, the results are obtained as listed in Table 5.6. It agrees within errors for the carbon run ($\Delta\beta = 7.28 \pm 1.5$) with the value from [Kac97]($\Delta\beta = 7.27 \pm 0.14$, for all target materials) and with the value for carbon from [WA8903] $\Delta\beta = 6.66 \pm 0.09$. The value for the tungsten run $\Delta\beta = 5.4 \pm 1.2$ also agrees within the large errors, but with a 1.5σ deviation. So there might be a dependence of the β_Λ parameter on the

run	ratio	value	other p–A experiments	E_{beam} [GeV]
C	$\frac{\overline{\Lambda}}{\Lambda}$	0.88 ± 0.07	0.67 ± 0.14	$\sqrt{s} = 31 - 53$
W	$\frac{\overline{\Lambda}}{\Lambda}$	0.64 ± 0.07		
C	$\frac{\overline{\Xi}}{\Xi}$	0.69 ± 0.12	0.62 ± 0.05	800
W	$\frac{\overline{\Xi}}{\Xi}$	0.67 ± 0.18		
C	$\frac{\overline{\Omega}}{\Omega}$	1.7 ± 1.4	0.55 ± 0.15	800
W	$\frac{\overline{\Omega}}{\Omega}$	1.7 ± 0.9		
C	$\frac{\Omega}{\Xi}$	0.05 ± 0.03	0.055 ± 0.010	800
W	$\frac{\Omega}{\Xi}$	0.29 ± 0.12		
C	$\frac{\overline{\Omega}}{\overline{\Xi}}$	0.08 ± 0.07	0.088 ± 0.010	800
W	$\frac{\overline{\Omega}}{\overline{\Xi}}$	0.44 ± 0.20		

Table 6.4: Final results of the extrapolation to $x_f = 0$, where the error on $\frac{\overline{\Lambda}}{\Lambda}$ includes the systematic error. In the last two columns, results from other experiments are given, taken from [Kac97]. The result on $\frac{\overline{\Lambda}}{\Lambda}$ was obtained by proton–proton collisions, the other values are from proton–beryllium interactions. The results on $\frac{\Omega}{\Xi}$ and $\frac{\overline{\Omega}}{\overline{\Xi}}$ are given at $p_t = 0.75$ and $p_t = 0.9$, for the numbers from other experiments at $p_t \neq 0$ are read from the corresponding figure in [Kac97] .

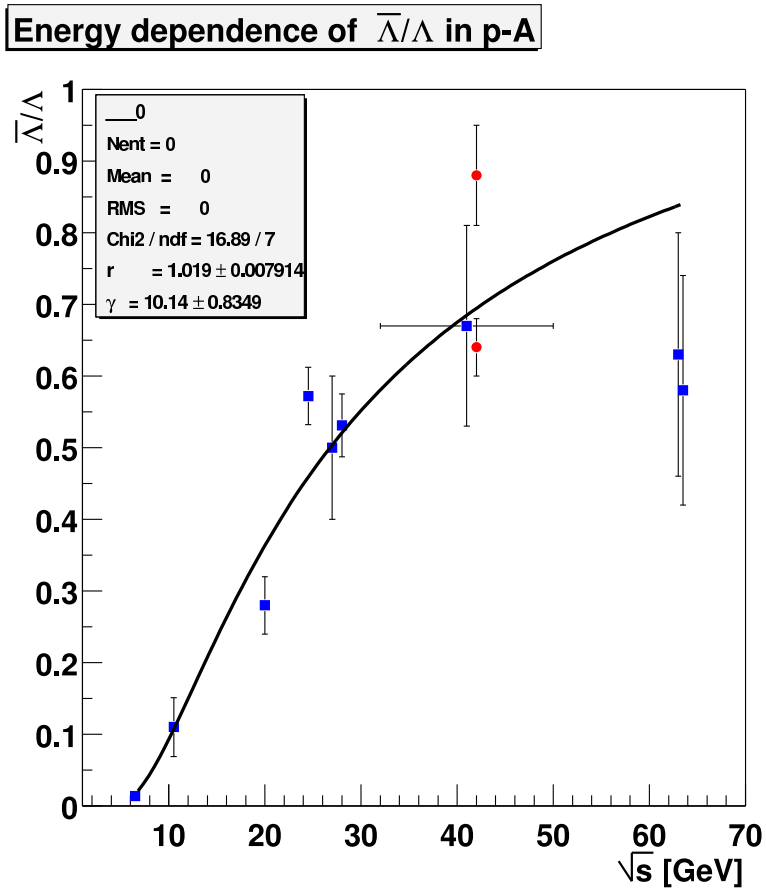

Figure 6.4: The circles are $\frac{\overline{\Lambda}}{\Lambda}$ extrapolated to $x_f = 0$. The squares are data from other p–A experiments also listed in Table 1.5. The squares only are fitted to the function $r \cdot (1 - \frac{2M}{\sqrt{s}})^{\gamma}$, where M is the Λ mass, as in [Kac97].

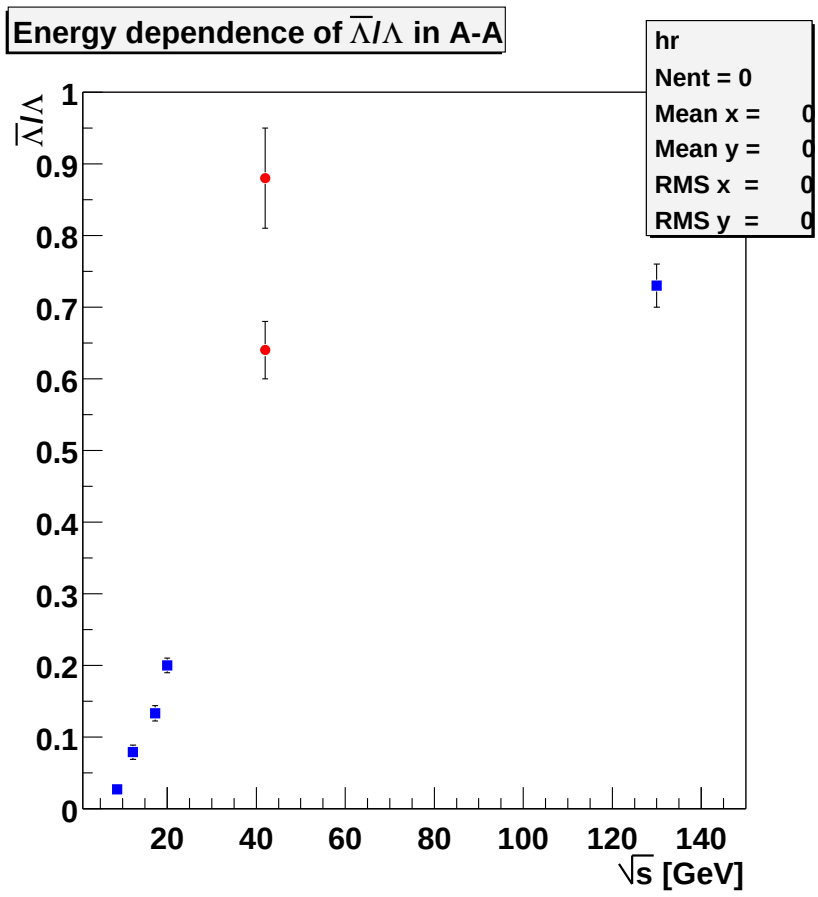

Figure 6.5: The circles are the HERA-B results on $\frac{\overline{\Lambda}}{\Lambda}$ extrapolated to $x_f = 0$. The squares are A–A data from experiments NA49 [Mis02], WA97 [Cal99], WA85 [Aba97a] and STAR [Zim01] (preliminary), most numbers are listed in Section 1.3.

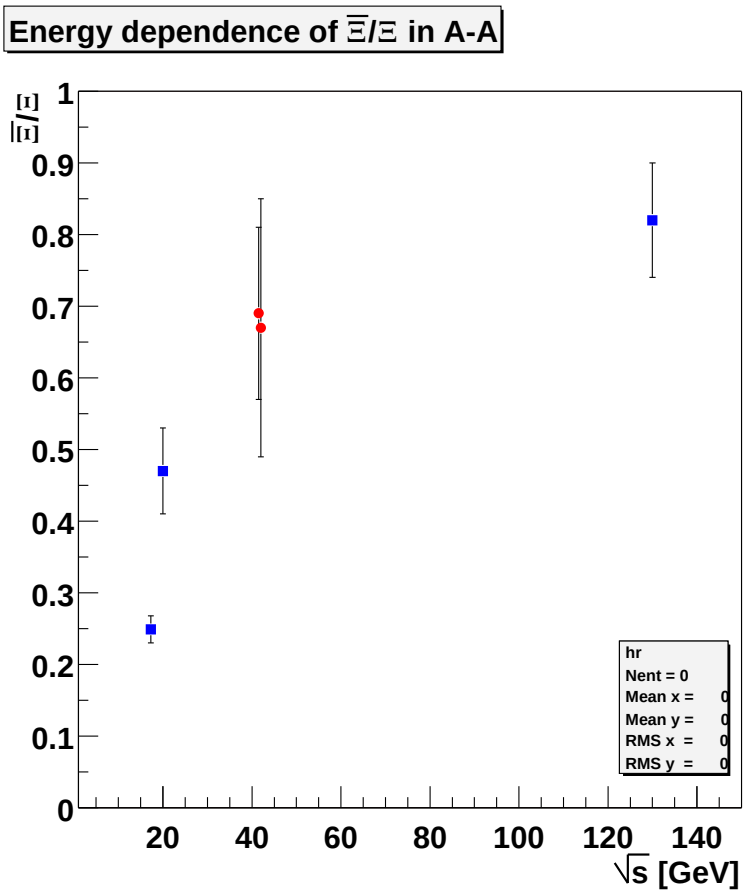

Figure 6.6: The circles are $\frac{\overline{\Xi}}{\Xi}$ extrapolated to $x_f = 0$ and the squares A–A data from experiments WA97 [Cal99], WA85 [Aba97a] and STAR [Zim01] (preliminary), numbers are listed in Section 1.3.

target material. If this would turn out to be true, the extrapolation Formula 5.1 would not be good for all materials, using the same parameter $\Delta\beta$.
The extrapolated values for hyperon ratios are again listed in table 6.4 together with results from different proton–nucleus experiments and also extrapolated to $x_f = 0$. The results given for $\frac{\Omega}{\Xi}$ and $\frac{\overline{\Omega}}{\overline{\Xi}}$ are at $p_t = 0.75$ and $p_t = 0.9$. These numbers were already presented in Section 1.3.1 extrapolated to $p_t = 0$. The HERA-B values agree within errors with the other data for all ratios. For $\frac{\Omega}{\Xi}$ and $\frac{\overline{\Omega}}{\overline{\Xi}}$ in the tungsten run the deviation is 2.2σ and 1.8σ. Since the values in the carbon run do agree within 1σ, and the other data was taken with beryllium as target material, this could be an indication for a nuclear mass dependence. On the other hand, the errors are large and the difference not really significant.
In Figure 6.4, the extrapolated $\frac{\overline{\Lambda}}{\Lambda}$ values are plotted as circles together with other proton–nucleus data. In Figure 6.5 it is plotted with nucleus–nucleus data. In both Figures, the HERA-B data fits well into the overall picture, apart from the carbon values being a bit high. In the context of QGP produced in nucleus–nucleus interaction, one would expect the HERA-B data to be significantly lower than the nucleus–nucleus data, which is not the case. It could be argued that the extrapolation is wrong, but the values in the Ξ region $-1.5 < y < 0.5$ are already high and would fit equally well into the plot. In Figure 6.6 then the extrapolated $\frac{\overline{\Xi}}{\Xi}$ is plotted with nucleus–nucleus data. Again the HERA-B values fit well into the other data and is not significantly lower, although the errors are of course large.

6.1.2 Results on Hyperon Asymmetries

In Figure 6.7, the Λ asymmetry distribution in x_f $A_\Lambda(x_f)$ is plotted together with results from the experiment E791 [Ait00]. In the E791 experiment, a π^- beam with four diamond and one platinum foils as targets were used. For the carbon run, the agreement of the HERA-B and E791 data is good. This supports the correctness of the ansatz in Section 1.2.2. For the tungsten target, the HERA-B data is systematically higher than in the results from E791. This could also be a nuclear mass dependence, but the errors are statistical errors only, so there can still be significant systematic errors. Another hint that nuclear effects do play a role, is that the HERA-B Monte Carlo including FRITIOF for nuclear effects can reproduce the Λ asymmetry (see Fig. 5.26) qualitatively better than the pure nucleon–nucleon simulation PYTHIA/JETSET Monte Carlo used in [Ait00]. The outcome of this Monte Carlo is shown in Figure 6.8. The FRITIOF results include the effect that the asymmetry is larger in the tungsten run. The large asymmetry at $x_f = 0$ that puzzled the authors of [Ait00] may be explained by nuclear effects. If this indications of nuclear effects in the x_f-asymmetry distribution are taken seriously, the model in [Gut02] presented in Section 1.2.2 would have to be changed since it only accounts for single hadron–nucleon interactions.

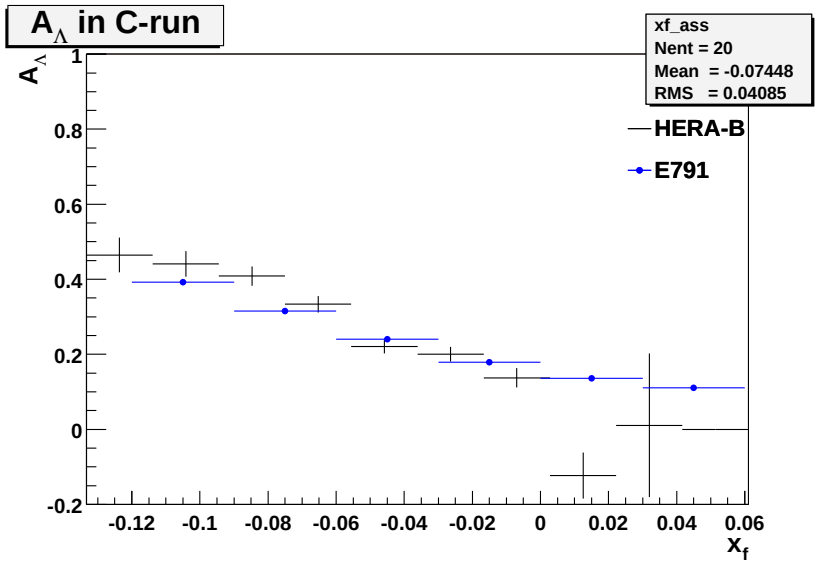

(a)

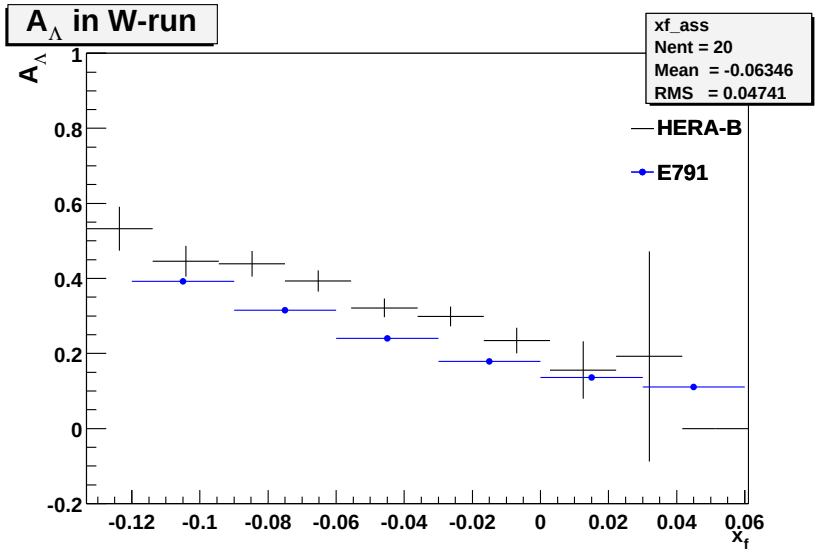

(b)

Figure 6.7: The Λ asymmetry x_f-distribution in comparison to results from E791 [Ait00] for carbon (a) and tungsten (b). HERA-B data, statistical errors only, the E791 results are marked by the circles, its errors are too small to be seen in this plot.

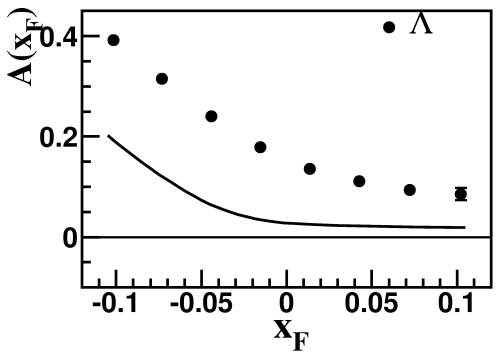

Figure 6.8: PYTHIA/JETSET results for Λ asymmetry compared to E791 results, taken from [Ait00]. When comparing this to the result of the HERA-B Monte Carlo also using FRITIOF to simulate nuclear effects (see Fig. 5.26), the HERA-B Monte Carlo reproduces the data qualitatively better, indicating that nuclear effects may be important in understanding hyperon asymmetry distributions.

6.2 Outlook

Meanwhile a much larger amount of interaction trigger data was recorded at HERA-B. After a rough run selection, one finds about 70 million events with the carbon, 70 million events with the tungsten and 25 million events with a titanium wire. This is ten times the statistics for the carbon and almost 30 times the statistics for the tungsten target used in this analysis. This means that the values for all hyperon ratios including Ξ, Ω or their anti-particle can be measured with a three times smaller statistical error for carbon and a fifth of the error for tungsten compared to this analysis. This also implies that the statistical error on $\frac{\overline{\Omega}}{\Omega}$ in the tungsten run decreases from over 50% to about 10%, the statistical error on $\frac{\overline{\Xi}}{\Xi}$ in the carbon run from about 16% to about 5%. In addition a measurement of the Ξ asymmetry with appropriate uncertainties will become feasible. Maybe a possible nuclear mass dependence of $\frac{\Omega}{\Xi}$ and $\frac{\overline{\Omega}}{\overline{\Xi}}$ can be measured then.
To achieve a smaller uncertainty for the Λ hyperons is more difficult, since the systematic error in this analysis is already about as large as the statistical error. Therefore it is crucial to have a better Monte Carlo description of the detector efficiencies. A more realistic description of the particle distributions in the Monte Carlo would also help much, and could be achieved also by reweighting Monte Carlo samples.
By also measuring the ratio $\frac{\overline{p}}{p}$, the coalescence model as presented in Section 1.2.1 could be tested the first time for proton–nucleus reactions at 920 GeV beam energy.

6.3 Conclusion

There are two main outcomes of this analysis. First, the HERA-B proton–nucleus data on $\frac{\overline{\Lambda}}{\Lambda}$ and $\frac{\overline{\Xi}}{\Xi}$ at 920 GeV beam energy fits qualitatively into the nucleus–nucleus data that were taken at different energies below and above 920 A GeV. This can have at least two reasons, one is that no QGP was produced in the nucleus–nucleus interaction in spite of some indications to the contrary. The second explanation, already mentioned in Section 1.3.3, is that the increase of the ratios $\frac{\overline{Y}_n}{Y_n}$ are not good signatures for QGP. Since there is already this indication from the coalescence model, the second seems to be the right explanation.
Another outcome of this analysis is the target material dependence of the ratio $\frac{\overline{\Lambda}}{\Lambda}$ in the region $-2.0 < y < 0.5$. This can either mean, that the ratio is different over the whole phase space, or that only the distributions in x_f are different. By employing the Monte Carlo as well as by using an extrapolation method in x_f, the second seems to be correct. As a possible reason, the smearing out in x_f due to Lorentz boosts in a second interaction of the beam proton in the target nucleus, can be given. On the other hand, the systematic error might be larger, and the difference thus not significant. The Λ particle–anti-particle x_f-distribution for the carbon run agrees with data taken in pion–nucleus interactions at 500 GeV pion beam energy from the experiment E791.

Appendix A

The Monte Carlo Simulation

In this appendix more details about the production and reconstruction of the Monte Carlo data are given. In Table A.1 the statistics with which the Monte Carlo data were generated is given.
The two problems of the production of Monte Carlo data are time and disk space, thus cuts had to be applied. In order to save disk space, the particles to be produced (Λ, Ξ or Ω hyperons) were forced to decay by the selected decay channel only (see Section 4.3). Then some cuts are applied to reduce the size of the files. For the Λs:

- $\theta > 0.015$ and $\theta_x < 0.250$ and $\theta_y < 0.160$ for the Λ
- the same for its decay products
- decay length < 150 cm
- $p_z < 120$ and $p_z > 5$ — in the data only few candidates lie outside of this region

where θ is the polar angle and θ_x (θ_y) means the polar angle projected to the $xz(yz)$-plane. For the Ξ and Ω simulation the following cuts were used:

- $\theta > 0.015$ and $\theta_x < 0.250$ and $\theta_y < 0.160$ for the particle itself
- the same for its decay products
- decay length < 200 cm

The cuts on θ correspond to the geometrical acceptance of the outer tracker as described in Section 3.3.2. The cut on the decay length of the Ξ/Ω particles can be understood by the fact that the particle has to decay in the VDS for the momentum to be calculated. The additional cuts for the Λ simulation are discussed in Section 5.4.1.
The steering file for the Monte Carlo digitation and reconstruction is listed here for the carbon run:

run	particle	generated	in MC truth
C	Λ	2945388	2938463
	$\overline{\Lambda}$	762841	762059
	Ξ	153457	149767
	$\overline{\Xi}$	106005	102766
	Ω	18518	272
	$\overline{\Omega}$	23764	358
W	Λ	2053787	2090050
	$\overline{\Lambda}$	538329	548233
	Ξ	103181	84495
	$\overline{\Xi}$	70646	57594
	Ω	10124	187
	$\overline{\Omega}$	12692	200

Table A.1: The statistics of the Monte Carlo generated data. The third column gives the number of particles generated, the last column how many particles are contained in the Monte Carlo truth distributions.

```
 wiremask = 00010000
 masking = yes

 DBOPEN GEODB -RO
 DBREAD GEODB NGHD 02 0103 EQ
 DBCLOSE GEODB
* ------------------------------------------------------------
* INPUT (file)
* ------------------------------------------------------------

 IOFILE EV_IN /nfs/d24/herab/users/markward/mcgen/lam1/fi_p10
000.a0401r2-11.g2.0903.0041.dst -IG

KEYBOOK 26 /key_table keytable
/CNA/RUN2CNAKEY 19170

* ------------------------------------------------------------
* VDS
* ------------------------------------------------------------
SETENV VDS_MASKING DBS

* ------------------------------------------------------------
```

```
* ITR
* ------------------------------------------------------------
* /ITR/ITRHITR    : set hit resolution
* /ITR/ITRHCUT 20 : max hit/chamber/event
* ------------------------------------------------------------
 /ITR/ITRHITR  0.02
 /ITR/ITRHCUT 50
* ------------------------------------------------------------
* OTR
* ------------------------------------------------------------
* OtrHitPreparation 0   : constants via OTRI
* OtrEventSwitch    3 : kill noisy hits
* ------------------------------------------------------------
SETENV OtrHitPreparation 0
* kill noisy and dead channels in MC (BP)
if [masking]=no then
  SETENV OtrEventSwitch    0
else
  SETENV OtrEventSwitch    259
endif
* ------------------------------------------------------------
* RICH
* ------------------------------------------------------------
 SETENV RICH_INSTALLDB /RICH_GEO
 SETENV RICH_RECODB    /RICH_RECO
* ------------------------------------------------------------
* ECAL
* ------------------------------------------------------------
 SETENV HBECALDB /ECAL_CALIB
* ------------------------------------------------------------
* RECO
* ------------------------------------------------------------
 /RECON/SUBD VDS  ON CATS
 /RECON/SUBD ITR  OFF
 /RECON/SUBD OTR  ON
 /RECON/SUBD RICH ON
 /RECON/SUBD ECAL ON
 /RECON/SUBD MUON ON
*
 /RECON/RTRA ON VDSOTR
 /RECON/RTRA2001 1
*
 /RECON/REFIT ON
* ------------------------------------------------------------
```

```
* RANGER
* http:../software/arte/ranger/ranger-steering/ranger-steerin
* g.html
* ------------------------------------------------------------
* rlevel=-1       : off
* rlevel=0        : ideal
* rlevel=1        : x projection in PC
* rlevel=2        : PC
* rlevel=3        : PC+MC
* rlevel=4        : PC+MC+TC
* rlevel=5        : PC+TC
*
* segstor=Y       : (default)
* fit=0           : (default)
* qpmxtrip=1.0    : momentum cut 1/p (default)
*
* sltmode=0       : skip            (default)
* sltmode=1       : electrons       SLT tracks is used as see
* sltmode=2       : muons           SLT tracks is used as see
* sltmode=3       : electrons+muons SLT tracks is used as see
* sltmagn=Y       : SLT trough magnet
* sltclone=Y      : store clones in RSEG
* fitmagn=N       : refit with rejection of hits in magnet
* ------------------------------------------------------------
 /RANGER/FPAR rlevel=5 sltmode=6 sltmagn=Y fitmagn=N

 /RANGER/FPAR cats=Y

* ------------------------------------------------------------
* MARPLE
* ------------------------------------------------------------
* MARPLE VDS PC     : should be first!
* ------------------------------------------------------------
 /RECON/MATCH MARPLE VDS PC
 /RECON/MATCH MARPLE VDS ECAL
 /RECON/MATCH MARPLE OTR RICH
 /RECON/MATCH MARPLE RTRA RICH

MASVDECALNORTRA 1 1

* ------------------------------------------------------------
* PID
* ------------------------------------------------------------
* MUON : seeded (MURECB)
```

```
* ------------------------------------------------------------
 /RECON/PID RICH ON  RITER RISE
 /RECON/PID ECAL ON
 /RECON/PID MUON ON
* ------------------------------------------------------------
* RISE
* ------------------------------------------------------------
* SEARCH  : occup=3000 (s/a) soccup=20000 (seeded) (defaults
* from DB)
* SEARCH  : cell=0.20 require a minimal seperation distance
* of photons
* ------------------------------------------------------------
 /RISE/SEARCH  rlevel=0 fit=0
 /RISE/SEARCH  occup=300 soccup=0
 rise/ring drad=0.007

* ------------------------------------------------------------
* RITER
* ------------------------------------------------------------
* DWIN 1000 : monitor some crucial parameters
* ------------------------------------------------------------
 /RITER/DWIN 1000
/RITER/NITER 0
/RITER/ETA 1.
* ------------------------------------------------------------
* Grover
* ------------------------------------------------------------
* WIREFOLLOWING  1 : wire following mechanism on
* TSELECTION     1 : track selection method to default
* WRITE_RTAR     1 : RTAR writing
* FIND_PRIMARIES 1 : primary finding
* ------------------------------------------------------------
 /GROVER/STEERING/WIREFOLLOWING  1
 /GROVER/STEERING/TSELECTION     1
 /GROVER/STEERING/WRITE_RTAR     1
 /GROVER/STEERING/FIND_PRIMARIES 1
* ------------------------------------------------------------
* CLASSIFICATION [Andreas]
* ------------------------------------------------------------
* (setting of bits, NO event selection!)
* www:  http://www-hera-b.desy.de/subgroup/farm/ECLASS.html
* ALL ON             : evaluation of all classes
* CAL1HT ON 4.0      : cluster Et > 4.0 GeV
* RECYPS ON 6.0      : l+l- candidate m > 6.0 GeV
```

```
* RECDV  ON 0.5 3.0  : detached vertex (default: dd<0.5cm OR
* dd>3.0cm)
* -------------------------------------------------------
 /RECON/CLASS ALL ON
*
 /RECON/CLASS JPSIEE ON
 /RECON/CLASS JPSIMM ON
 /RECON/CLASS CAL1HT ON 4.0
 /RECON/CLASS FCNC   ON
 /RECON/CLASS VZERO  ON
 /RECON/CLASS VZERO2 ON
 /RECON/CLASS DVTX   ON
 /RECON/CLASS SLTYPS ON
 /RECON/CLASS SLTCUT ON
 /RECON/CLASS SLTEEB ON
 /RECON/CLASS SLTEE  ON
 /RECON/CLASS SLTMM  ON
 /RECON/CLASS SLTDV  ON
* /RECON/CLASS TLT    ON
 /RECON/CLASS FLTTRG ON
 /RECON/CLASS RNDTRG ON
 /RECON/CLASS RECYPS ON 6.0
 /RECON/CLASS RECDV  ON 0.5 5.0
 /RECON/CLASS DIMUON ON
 /RECON/CLASS ALIGN  ON
* -------------------------------------------------------
* SLT
* -------------------------------------------------------
* FILL ON : filling of tables RSLA/RSLI replacing DSLT
* (default: OFF)
* -------------------------------------------------------
 /SLT/FILL ON
* -------------------------------------------------------
* OUTPUT
* -------------------------------------------------------
 IOTAB OUTPUT HITL
 IOTAB OUTPUT DDST
* -------------------------------------------------------
* DST
* -------------------------------------------------------
* DDST : Steering table (empty)
* DIHD : Raw data header table
* DEVT : Full raw data event (includes)
* DTLT : TLT information filled during DQ (not in raw data)
```

```
* D4LT : 4LT information presently not filled
*  (not in raw data)
* DTA1 : Target data from GTAR
* HITL : Hit table for luminosity determination in MB
* ------------------------------------------------------------
 IOTAB  DST EVHD
 IOTAB  DST EVRC
 IOTAB  DST EVFN
 IOTAB  DST EVHI
*
 IOTAB  DST RTRA
 IOTAB  DST RCCL
 IOTAB  DST RVER
 IOTAB  DST RREL
 IOTAB  DST RTRI
 IOTAB  DST RTAR
 IOTAB  DST RSLA
 IOTAB  DST RSLI
 IOTAB  DST RSEG
*
 IOTAB /DST HITL
*
 IOTAB  DST DDST
 IOTAB  DST DIHD
 IOTAB  DST DEVT
 IOTAB /DST DDAQ
 IOTAB /DST DSVD
 IOTAB /DST DITR
 IOTAB /DST DPTC
 IOTAB /DST DOTR
 IOTAB /DST DRIC
 IOTAB /DST DTRD
 IOTAB /DST DCAL
 IOTAB /DST DMUP
 IOTAB /DST DMUT
 IOTAB /DST DMUX
 IOTAB /DST DFLT
 IOTAB /DST DSLT
 IOTAB  DST DTLT
 IOTAB  DST D4LT
 IOTAB /DST DTAR
 IOTAB /DST DFCS
 IOTAB /DST DTST
 IOTAB /DST DKEY
```

```
 IOTAB  DST DTA1
*
 IOTAB  DST TAHD
 IOTAB  DST TAHB
 IOTAB  DST TATR

 IOTAB /DST MTCP

* ------------------------------------------------------------
* Digitisation parameters
* ------------------------------------------------------------
 HBDIGI/DGSEL *
 HBDIGI/DGLEV OTR 3
 HBDIGI/DGLEV ECAL 2
 HBDIGI/DGLEV ITR 1
 HBDIGI/OTRGAUSSMEARING 0.04
 HBDIGI/OTRNOMINALEFFICIENCY 0.90
* ------------------------------------------------------------
* Muon digitisation parameters
* ------------------------------------------------------------
 SETENV MUON_CONFIG $HBROOT/MUON/db/Mu.config
 if [masking]=no then
   SETENV MUON_BADFILE $HBROOT/MUON/db/Mu.mask_blank
 else
   SETENV MUON_BADFILE $HBROOT/MUON/db/Mu.mask_strict
 endif
* ------------------------------------------------------------
* VDS digitisation parameters
* ------------------------------------------------------------
 if [masking]=no then
   SETENV VDS_MASKING OFF
 else
   SETENV VDS_MASKING ON
 endif

* ------------------------------------------------------------
* Wiremask - used in patch to remove GTAR entries
* BP: the patch for this is missing!!!
* ------------------------------------------------------------
* PAIN - kuip removes leading zeroes...
 if [wiremask]=1000 then
   setenv WIREMASK 00001000
 elseif [wiremask]=10000 then
   setenv WIREMASK 00010000
```

```
 elseif [wiremask]=11000 then
   setenv WIREMASK 00011000
 endif

nmax = 3000
do i=1,20
  if ([i] .gt. 1) then
    close dst_out
  endif
  iofile dst_out fi_p10000.a0401r2-11.g2.0903.0011.[i].a.mini -go
  run [nmax]
enddo

quit
*-------------------------------------------------------------
 ENDKUMAC
* -------------------------------------------------------------
```

Bibliography

[Aba97a] S. Abatzis et al., *Hyperon production in proton-tungsten interactions at 200 GeV/c*, Phys. Let. **B 393** (1997) 210

[Aba97b] S. Abatzis et al., *Hyperon production in proton-sulphur collisions at 200 GeV/c*, Phys. Let. **B 400** (1997) 239

[Abt03] I. Abt et al., *GROVER: A vertexing package for the HERA-B experiment*, to be submitted to Nucl. Instr. Meth. (2003)

[Aga01] M. Agari, *Search for the decay of charmed mesons with the HERA-B detector in proton-nucleon collisions at* $\sqrt{s} = 42$ *GeV*, Diploma Thesis, Universität Heidelberg, October 2001

[Ait00] E. M. Aitala et al., *Asymmetries in the production of* Λ^0*,* Ξ^-*, and* Ω^- *hyperons in 500 GeV/c* π^-*-nucleon interactions*, Phys. Let. **B 496** (2000) 9

[Ari00] I. Ariño et al., *The HERA-B RICH*, Nucl. Instr. Meth. **A453** (2000) 289

[ART03] The HERA-B software group, `http://www-hera-b.desy.de/subgroup/software/` (status: March 2003)

[Aub02] B. Aubert et. al. [BaBar Collaboration], *Measuring of the CP-Violating Asymmetry Amplitude* $\sin 2\beta$, hep-ex/0207042 (2002) a preprint of Phys. Rev. Lett. **89** (2002) 201802

[Bal75] A.M. Baldin et al., *Experimental investigations of cumulative meson production*, Sov. J. Nucl. Phys., **20** (1975) 629

[Bal00] V. Balagura et al., *High-*P_T *trigger for HERA-B experiment*, Nucl. Instr. Meth. **A453** (2000) 412

[Bau03] C. Bauer et al., *Performance of the HERA-B Vertex Detector System*, Nucl. Instr. Meth. **A 501** (2003) 39

[Bia98] A. Bialas, *Quark model and strange baryon production in heavy ion collisions*, arXiv:hep-ph/9808434v1 being a preprint of Phys. Lett. **B 442** (1998) 449

[Bor97] C. Bormann for the NA49 Collaboration, *Kaon-,* Λ- *and* $\overline{\Lambda}$- *production in Pb+Pb collisions at 158 GeV per nucleon*, J. Phys. **G 23** (1997) 1817

[Brä01] M. Bräuer, *Die Alignierung des HERA-B Vertexdetektors*, Dissertation, Universität Heidelberg, October 2001

[Cal99] R. Caliandro for the WA97 Collaboration, Λ, Ξ *and* Ω *production at mid-rapidity in Pb+Pb and p-Pb collisions at 158 A GeV/c*, J. Phys. **G 25** (1999) 171

[Cow98] G. Cowan, *Statistical Data Analysis*, Oxford University Press (1998)

[CER03] CERN, The ROOT System Home Page, `http://root.cern.ch/` (status: March 2003)

[DES01] Deutsches Elektronen Synchrotron Hamburg, URL: `http://www.desy.de` (status: August 2002)

[Dim01] S. Dimopoulos, G. Landsberg, *Black Holes at LHC*, Phys. Rev. Lett. 87 (2001) 161602

[Dov95] C. B. Dover, *Aspects of Strangeness*, Nucl. Phys. **A 590** (1995) 333c

[Eis99] F. Eisele *The MSGC An introduction by F.Eisele*, HERA-B Inner Tracker group Heidelberg homepage, URL: `http://www1.physi.uni-heidelberg.de/~eisele/MSGC_Introduction.html` (status: September 2002)

[Eme01a] D. Emeliyanov et al., *Grover*, `http://www-hera-b.mppmu.mpg.de/analysis/grover.html` (status: March 2003)

[Eme01b] D. Emeliyanov et al., *OTR/ITR CATS: Tracking Based on Cellular Automaton and Kalman Filter*, HERA-B internal note01-137 (2001)

[Fra87] H. Frauenfelder/E. M. Henley, *Teilchen und Kerne*, 2nd edition, Oldenburg (1987)

[Frü00] R. Frühwirth, M. Regler, R.K. Bock, H. Grote, D. Notz, *Data Analysis Techniques for High-Energy Physics*, 2nd edition, Cambridge University Press (2000)

[Fun99] M. Funcke, *Alignement der HERA-B Targetmechanik*, Diploma Thesis, Universität Dortmund, March 1999

[GEA93] *GEANT 3.21 Detector Description and Simulation Tool*, CERN Program Library Long Writeup W5013, CERN, Genève (1993) to find under:
`http://wwwinfo.cern.ch/asdoc/geant_html3/geantall.html`

[Gle00] T. Glebe, *Vt++ Version 1.0*, HERA-B Internal Note 00-175 (2000)

[Gle01a] T. Glebe, *BEE – Interfaces and Design Issues*, HERA-B Internal Note 01-136 (2001)

[Gle01b] T. Glebe, *Clue – The BEE event model library*, HERA-B Internal Note 01-138 (2001)

[Gle01c] T. Glebe, *SMatrix - A high performance library for Vector/Matrix calculation and Vertexing*, HERA-B Internal Note 01-134 (2001)

[Gle02] T. Glebe, private comunication September 2002,`/afs/desy.de/group/hera-b/ARTE/ARTE-04-01-r2/cluearte/SlTableFill.C`

[Gor77] M.I. Gorenstein and G.M. Zinovjev, *Cluster Model of cumulative Particle Production in Hadron-Nucleus Collisions*, Phys. Lett. **B 67** (1977) 100

[Gra01] W.Grandl, *The Inner Tracker of HERA-B*, Nucl. Instr. Meth. **A461** (2001) 80

[Gri87] D. Griffiths, *Introduction to Elementary Particles*, John Wiley & Sons (1987)

[Gut02] T. Gutierrez, R.Vogt, *Asymmetries Between Strange and Antistrange Particle Production in Pion-Proton Interactions*, Lawrence Berkeley National Laboratory LBNL-47715, a preprint of Nucl. Phys. **A705** (2002) 396

[Hag02] K. Hagiwara et al., *Review of Particle Physics* Phys. Rev. **D 66**, 010001 (2002)

[HB94] T. Lohse et al., *HERA-B – An experiment to study CP violation in the B system using an internal target at the HERA proton ring*, Proposal, DESY-PRC 94/02 (May 1994)

[HB95] H. Albrecht et al., *HERA-B – An experiment to study CP violation in the B system using an internal target at the HERA proton ring*, Technical Design Report, DESY-PRC 95/01 (January 1995)

[HB00] The HERA-B collaboration, *Report on status and prospects*, DESY-PRC 00/04 (October 2000)

[Igo98] O. Igonkina, *MARPLE -Version 1.03-*, HERA-B Internal Note 98-129 (1998); for a more recent online reference see: `http://www-hera-b.desy.de/subgroup/software/arte/MARPLE` (status: March 2003)

[Iva99] J. Ivarsson et al., *PYTHIA and FRITIOF: Event Generators for HERA-B*, HERA-B Internal Note 99-067 (1999)

[Kac97] Th. Kachelhoffer, W. M. Geist, *Estimates of relative yields of strange baryons and antibarions from pp and pA interactions* Phys. Let. **B 394**, (1997) 225

[Kan97] M. Kaneta for the NA44 Collaboration, *Particle ratios from central Pb+Pb collisions at the CERN SPS*, J. Phys. **G 23** (1997) 1865

[Kis99] I.Kisel, S. Masciocchi, *CATS – A Cellular Automaton for Tracking in Silicon for the HERA-B Vertex Detector*, HERA-B Internal Note 99-242 (1999)

[Koc86] P. Koch et al., *Strangeness in Relativistic Heavy Ion Collisions* Phys. Rep. **142**, No. 4 (1986) 167

[Kre01] P. Kreuzer, *Experience with HERA-B triggering*, Nucl. Instr. Meth. **A462** (2001) 212

[LHC02] LHCb homepage, URL: `http://lhcb.web.cern.ch/lhcb/` (status: November 2002)

[Man97] R. Mankel, *A concurrent track evoluttion for pattern recognition in the HERA-B main tracking system*, Nuc. Instr. Meth. **A 395** (1997) 169

[Mis02] A. Mischke for the NA49 Collaboration, *Energy Dependence of* Λ *and* $\bar{\Lambda}$ *Production at CERN-SPS Energies*, arXiv:nucl-ex/0209002

[Nac91] O. Nachtmann, *Phänomene und Konzepte der Elementarteilchenphysik*, Vieweg Braunschweig (1991)

[Per82] D. H. Perkins, *Introduction to High Energy Physics*, 2nd edition, Addison-Wensley (1982)

[Pet02] B. A. Petersen, *Beauty Production at HERA-B*, Dissertation, University of Copenhagen, May 2002

[Ple01] M.-A. Pleier, *Cloneremove V1.0*, HERA-B Internal Note 01-062 (2001)

[Ple02] M.-A. Pleier, *Measurement of inclusive $\Lambda/\bar{\Lambda}$ hyperon polarisation in proton nucleus collisions at 920 GeV proton beam energy*, Dissertation, Universität Heidelberg, July 2002

[Pov95] B. Povh, K. Rith, C. Scholz, F. Zetsche, *Teilchen und Kerne*, 3nd edition, Springer (1995)

[Now94] S. Nowak, *A Description of HERA-B GEANT*, HERA-B Internal Note 94-123 (1994)

[Pi92] H. Pi, *An event generator for interactions between hadrons and nuclei - FRITIOF version 7.0*, Comp. Phys. Comm. **71** (1992) 173

[Pyr02] J.Pyrlik, Schematic draw of the HERA-B detector, URL: `http://www-hera-b.desy.de/subgroup/pictures/detector_schematic.eps` (status: October 2002)

[San02] F. Sanchez, private comunication May 2002, `/afs/desy.de/group/hera-b/ARTE/ARTE-04-01-r2/reco/rcSelect_K0S_Lambda.C` (2001)

[Sch02a] B. Schwingenheuer, private comunication November 2002

[Sch02b] M. Schmelling, private comunication September 2002, `/afs/desy.de/group/hera-b/ARTE/ARTE-04-01-r2/analysis/anl_eventselect.C`

[Sjö94] T. Sjöstrand, *PYTHIA 5.7 and JETSET 7.4, Physics and Manual*, Comp. Phys. Comm. **82** (1994) 74, hep-ph/9508391

[Ste02] F. W. Stecker, *The Matter-Antimatter Asymmetry of the Universe*, hep-ph/0207323 (2002)

[Tit00] M. Titov et al., *The MUON system in the HERA-B experiment*, Nucl. Instr. Meth. **A446** (2000) 355

[Tom94] K. Tomizawa et al., Λ *hyperon production at backward angles in the reaction* $\pi^- {}^6Li \rightarrow \Lambda X$ *at 4 GeV / c*, Phys. Lett. **B 328** (1994) 264

[WA8903] The WA89 Collaboration, V^0, $\overline{\Xi}^+$ *and* Ω^- *inclusive production cross sections*, Eur. Phys. J. **C 26** (2003) 357

[Wol83] L. Wolfenstein, *Parametrization of the Kobayashi-Maskawa Matrix*, Phys. Rev. Lett. **51** (1983) 1945

[Won94] C.-Y. Wong, *Introduction to High-Energy Heavy-Ion Collisions*, World Scientific (1994)

[Zim99] R. Zimmermann, *Zeitmesstechnik für den HERA-B Detektor*, Ph. D. Thesis, Universität Rostock, Juli 1999

[Zim00] J. Zimányi et al., *Quark liberation and coalescence at CERN SPS*, Phys. Lett. **B 472** (2000) 243

[Zim01] J. Zimányi et al., *Hyperon Ratios at RHIC and the Coalescence Predictions at Mid-Rapidity*, arXiv:hep-ph/0103156v1 (2001) submitted to World Scientific.

[Zoc00] A. Zoccoli et al., *The electromagnetic calorimeter of the HERA-B experiment*, Nucl. Instr. Meth. **A446** (2000) 246

Danksagung

Zuerst möchte ich Herrn Prof. Werner Hofmann und Herrn Prof. Karl-Tasso Knöpfle für die Übernahme der Gutachten danken. Außerdem natürlich Herrn Priv. Doz. Michael Schmelling für die gute Betreuung, er hat immer Zeit gehabt und vor allem auch immer gute Ideen.

Mein Dank gilt auch den Angestellten am MPI für die freundliche Unterstützung, darunter besonders Frau Jacqueline Suppanz-Pirsch.

Außerdem möchte ich meinen Zimmerkollegen Marc-André, Michaela, Mikhail und Torsten danken, zum einen für das sehr gute Arbeitsklima, bei der oft etwas trockenen Arbeit war der nötige Humor immer vorhanden. Zum anderen dafür, daß sie sich immer viel Zeit für mich und meine Fragen genommen haben.
Aber auch allen Mitgliedern der HERA-B Collaboration, die mich unterstützt haben und die mir bei Fragen geholfen haben, gilt mein Dank.
Zusätzlicher Dank gilt den Leuten, die für mich diese Arbeit korrektur gelesen haben: Johan, Marc-André, Michaela und Michael.

Besonders möchte ich mich bei den "Physiker Kochern" bedanken, gerade in der Zeit der Diplomarbeit bot das wöchentliche kochen mit Euch einen super Ausgleich. Speziell bedanken möchte ich mich bei Jan, Nicole, Ronny und Stephen für ihre Freundschaft und Unterstützung vieler Art, die das gesamte Studium zu einer sehr schönen Zeit gemacht haben.

Und "last but not least" möchte ich mich bei meinen Eltern bedanken, dafür, daß sie mir das Studium ermöglicht und mich dabei unterstützt haben und vor allem, daß sie mich zu einem Auslandsaufenthalt ermutigt und mich dabei (nicht nur) finanziell unterstützt haben.

Erklärung

Ich versichere, daß ich diese Arbeit selbständig verfasst und keine anderen als die angegebenen Quellen und Hilfsmittel benutzt habe.

Heidelberg, den 6.5.2003 Markward Britsch